12-15-2018

Petrogenesis of Enriched and Intermediate Poikilitic Shergottites: From Magmatic Source to Emplacement

Rachel Rahib
rachel.rahib93@gmail.com

PETROGENESIS OF ENRICHED AND INTERMEDIATE POIKILITIC SHERGOTTITES:

FROM MAGMATIC SOURCE TO EMPLACEMENT

By

Rachel R. Rahib

Bachelor of Science – Geoscience
University of Nevada, Las Vegas
2015

A thesis submitted in partial fulfillment
of the requirements for the

Master of Science – Geoscience

Department of Geoscience
College of Sciences
The Graduate College

University of Nevada, Las Vegas
December 2018

Thesis Approval

The Graduate College
The University of Nevada, Las Vegas

December 7, 2018

This thesis prepared by

Rachel Rahib

entitled

Petrogenesis of Enriched and Intermediate Poikilitic Shergottites: from Magmatic Source to Emplacement

is approved in partial fulfillment of the requirements for the degree of

Master of Science
Geoscience

Arya Udry, Ph.D.   Kathryn Hausbeck Korgan, Ph.D.
Examination Committee Chair   *Graduate College Interim Dean*

Simon Jowitt, Ph.D.
Examination Committee Member

Shichun Huang, Ph.D.
Examination Committee Member

Rebecca Martin, Ph.D.
Graduate College Faculty Representative

Abstract

Poikilitic shergottites, making up >20% of martian meteorites, likely represent a significant composition of the martian crust, as intrusive gabbroic rocks. To further constrain petrogenetic relationships amongst enriched and intermediate poikilitic shergottites, we utilize bulk rock trace element compositions, mineral major element compositions, phosphorus maps of olivine grains, oxygen fugacity (fO$_2$) values, subsolidus equilibration temperatures, and quantitative textural analyses, of the most comprehensive suite of poikilitic shergottites yet (11 samples), including three newly recovered samples (Northwest Africa [NWA] 11065, NWA 11043, NWA 10961). Although petrographically light rare earth element (LREE) enriched and intermediate poikilitic shergottites are similar, distinct LREE abundances suggest derivation from at least two unique magmatic sources. The characteristic bimodal textures (poikilitic and non-poikilitic textures) of poikilitic shergottites record evolving magmatic conditions at different stages of crystallization. Hotter, more reducing conditions, during early-stage crystallization, are recorded in the poikilitic textures and, cooler, more oxidizing conditions, at late-stage crystallization, are recorded in the non-poikilitic textures. Oxygen fugacity estimates for early-stage olivine-pyroxene-spinel assemblages of enriched and intermediate poikilitic shergottites suggest decoupling of fO$_2$ and degree of LREE-enrichment (i.e., [La/Yb]$_{CI}$), and increases in fO$_2$ exceeding 1 log unit from poikilitic to non-poikilitic textures implies auto-oxidation and degassing. Phosphorus maps of poikilitic and non-poikilitic olivine grains within NWA 10618, NWA 7755, and ALHA 77005 demonstrate transition from equilibrium growth in a magma staging chamber, followed by disequilibrium growth in transit to the surface, whereas phosphorus maps within LEW 88516 and NWA 11065 show disequilibrium growth during poikilitic olivine crystallization. Quantitative textural analyses of both enriched and intermediate poikilitic shergottites supports emplacement

as various cumulate piles or shallow intrusive bodies, as well as a potentially widespread

emplacement mechanism responsible for a major lithology of the martian crust.

Acknowledgements

First and foremost, I owe thanks to my advisor, Dr. Arya Udry, who has been a role model of mine since my senior year of undergrad. She is the perfect example of how hard work and perseverance allow you to achieve your goals. If it were not for her enthusiasm, encouragement, and support, I likely would not have pursued this degree. So much of my growth as a scientist is due to her, and I am so grateful for everything she has done (e.g., exposing me to funding opportunities that ended up in me having a NASA fellowship, funding and organizing my travels to conferences, arranging our visit to the Smithsonian Museum in D.C., encouraging and facilitating my internship with NASA JSC, and just being genuinely invested in my success) that allowed me to have so many amazing opportunities and experiences throughout my masters. I also wish thanks to my committee members Dr. Shichun Huang, Dr. Simon Jowitt, and Dr. Rebecca Martin for their edits, and more importantly, their time, given throughout this project, Dr. Minghua Ren for his help and advice during all of my EMP analyses at UNLV, and my collaborators, Dr. Julianne Gross, Dr. Geoffrey Howarth, Dr. James Day, and Dr. Marine Paquet, who assisted with data retrieval and interpretations. I am sincerely grateful for all of the close friends (especially Zoe) I made in grad school that always insisted I take breaks, so we could hang out. Last, but not least, I could not have successfully completed this project without my amazing family and best friends (Jessie, Jessica, Vanessa, and Carrie), whose constant emotional support (and endless favors) played a vital role in keeping my spirits high throughout grad school.

To my amazing fiancé, Edward, and our four children, whose continuous patience, love, and understanding allow me to thrive both professionally and personally.

Table of Contents

List of Tables

List of Figures

1. Introduction

Martian meteorites, the only available samples from Mars, mostly consist of different types of basalts and gabbros, with the shergottites, being the most abundant group (~90% of martian meteorites; Bridges and Warren, 2006). Shergottites are petrologically classified into four petrographic subgroups: Basaltic, olivine-phyric, poikilitic, and gabbroic (e.g., McSween and Treiman, 1998; Goodrich, 2002; Bridges and Warren, 2006; Walton et al., 2012; Filiberto et al., 2018; Udry et al., 2017). Basaltic and olivine-phyric shergottites are thought to represent extrusive rocks, whereas poikilitic and gabbroic shergottites are thought to be plutonic in origin (e.g., McSween, 1994; Goodrich et al., 2002; Bridges and Warren, 2006; Gross et al., 2011; Filiberto et al., 2014; Howarth et al., 2014; Udry et al., 2017; Combs et al., 2018). As Mars is predominantly a basaltic planet, systematic study of shergottites can lend insight into the martian interior, including martian crustal formation processes.

A geochemical classification scheme has been defined for the shergottites on the basis of their relative enrichments of the light rare earth elements (LREE), comprising three classes: Enriched, intermediate, and depleted. The geochemical signatures of the shergottites pertain to the distinct magma sources from which these igneous rocks crystallized. At least two distinct magma sources are thought to be responsible for the generation of the three shergottite subgroups: 1) A reduced, unradiogenic (i.e., low initial $^{87}Sr/^{86}Sr$, high $\varepsilon^{143}Nd$, and high $\varepsilon^{176}Hf$), incompatible-element depleted source, and 2) A more oxidized, radiogenic (i.e., high initial $^{87}Sr/^{86}Sr$, low $\varepsilon^{143}Nd$, and low $\varepsilon^{176}Hf$, incompatible-element enriched source (e.g., Herd et al., 2002; Jones., 2003, Borg and Draper 2003; Symes et al., 2008; Brennecka et al., 2014; McSween, 2015). The depleted source is thought to have been derived from the mantle, whereas the location of the enriched source is still highly debated and could be located within the martian mantle, crust, or both (e.g., Herd,

2003; Bridges and Warren, 2006; Symes et al., 2008; Brandon et al., 2012; Basu Sarbadhikari et al., 2011; Shearer et al., 2013; McSween, 2015; Peters et al., 2015). To date, poikilitic shergottites have only been classified as enriched [$(La/Yb)_{CI}$ = >0.8] and intermediate [$(La/Yb)_{CI}$ = ~0.3–0.8] (e.g., Harvey et al., 1993; Treiman et al., 1994; Mikouchi et al., 2005; Usui et al., 2010; Liu et al., 2011; Jiang and Hsu, 2012; Howarth et al., 2014; 2015; Walton et al., 2012; Combs et al., 2018), suggesting enriched and intermediate poikilitic shergottites do not originate from a common magmatic source.

Previously, it was proposed that poikilitic shergottites may have formed from the same magma suite and originated from a common igneous body on Mars (e.g., Mikouchi and Kurihara, 2008). However, this suggestion was based on the investigation of intermediate shergottites only, as enriched poikilitic shergottites were first identified in 2010 (e.g., Usui et al., 2010; Jiang and Hsu, 2012; Howarth et al., 2014; 2015; Combs et al., 2018). Enriched and intermediate poikilitic shergottites share similar textural attributes (i.e., bimodal poikilitic textures) and mineral assemblages (e.g., McSween et al., 1979; Harvey et al., 1993; Treiman et al., 1994; Goodrich, 2002; Lin et al., 2005; Mikouchi, 2005; Usui et al., 2010; Lin et al., 2013; Howarth et al., 2014; 2015; Combs et al., 2016), supporting the proposal of a common poikilitic igneous crystallization location. Yet, additional petrological and geochemical characteristics suggest that the enriched poikilitic shergottites may be petrogenetically related to enriched olivine-phyric and basaltic shergottites, rather than to intermediate poikilitic shergottites. For example, some members of the enriched poikilitic shergottites display both crystallization and ejection ages that are comparable to some enriched basaltic and olivine-phyric shergottites. Roberts Massif (RBT) 04261/2 and NWA 4468 are the only enriched poikilitic shergottites that have been analyzed for both crystallization ages and cosmic ray exposure (CRE) ages. They yield Sm-Nd crystallization ages

of ~150 ± 29 Ma (Borg et al., 2008) and ~179 ± 27 Ma (Shih et al., 2009), respectively, and CRE ages of ~3 Ma (Nishiizumi and Caffee, 2010; Wieler et al., 2016). Crystallization and CRE ages of RBT 04261/2 and NWA 4468 coincide with crystallization ages (157 Ma – 203 Ma) and CRE ages (~2.5 Ma) of some enriched basaltic and olivine-phyric shergottites (e.g., Shih et al., 1982; Nyquist et al., 2001; Shih et al., 2003; Borg et al., 2008; Lapen et al., 2009; Marks et al., 2010; Usui et al., 2010; Wieler et al., 2016). In addition to crystallization ages, isotopic ratios ($^{176}Hf/^{177}Hf$, $^{143}Nd/^{144}Nd$, and $^{87}Sr/^{86}Sr$) have been determined for RBT 04262 and NWA 4468, yielding similar values as other enriched shergottite sources (e.g., Shih et al., 2003; Borg et al., 2008; Lapen et al., 2009; Marks et al., 2010). This may suggest a possible genetic relationship between these martian meteorites, where enriched poikilitic shergottites were produced via polybaric crystallization in the interior of Mars and enriched basaltic shergottites formed from the same parental magma after eruption onto the martian surface (e.g., Howarth et al., 2014).

Intermediate poikilitic shergottites have yielded consistent crystallization ages of 150 Ma to 212 Ma, as well as similar CRE ages ranging from ~4 Ma to ~4.7 Ma (e.g., Shih et al., 1982; Morikawa et al., 2001; Nyquist et al., 2001; Borg et al., 2002; Eugster et al., 2002; Christen et al., 2005; Misawa et al., 2006; Kong et al., 2007; Misawa et al., 2008; Liu et al., 2011; Shih et al., 2011). Although crystallization ages of intermediate poikilitic shergottites overlap with that of enriched shergottites, their CRE ages represent a more recent ejection event (e.g., Nyquist et al., 2001; Misawa et al., 2006; Borg et al., 2008; Lapen et al., 2009; Marks et al., 2010; Jiang and Hsu, 2012; Cassata and Borg, 2015). More recently, two other enriched poikilitic shergottites, NWA 6342 and NWA 7397, have been analyzed for CRE ages and yielded ages of ~4.5 Ma, which is more consistent with the ejection event found for intermediate poikilitic shergottites (e.g., Nyquist et al., 2001; Wieler et al., 2016). Thus, the formation and spatial associations between enriched

and intermediate shergottites are still up for debate (e.g., McSween, 1994; Treiman et al., 1994; Goodrich, 2002; Mikouchi, 2005; Bridges and Warren, 2006; Usui et al., 2010; Jiang and Hsu, 2012; Howarth et al., 2014; Combs et al., 2016).

Using the most comprehensive collection (11 samples) of poikilitic shergottites to date, including three that have not been previously studied [Northwest Africa (NWA) 11065, NWA 11043, and NWA 10961], I further constrain formation, magmatic evolution, and emplacement of poikilitic shergottites, by use of bulk rock trace element data, *in situ* major element data, oxygen fugacity (fO$_2$) values, subsolidus equilibration temperatures, phosphorus (P) maps of olivine grains, and quantitative textural analyses.

2. Samples and analytical methods

2.1 Samples

Eleven poikilitic shergottite meteorites were chosen for this study, which include Northwest Africa (NWA) 7755, NWA 7397, NWA 4468, NWA 10169, NWA 10618, NWA 10961, NWA 11065, NWA 11043, Allan Hills (ALHA) 77005, Lewis Cliff (LEW) 88516, and Roberts Massif (RBT) 04261/2. I have investigated one thin section for NWA 7755, NWA 11065, NWA 11043, and RBT 04261/2; two polished thin sections for NWA 7397, NWA 10169, NWA 10618, NWA 10961, ALHA 77005, and LEW 88516; and three polished thin sections for NWA 4468. NWA meteorites were purchased through meteorite dealers, while ALHA 77005, LEW 88516, and RBT 04261/2 were obtained on loan through the Meteorite Working Group.

2.2 Electron microprobe analyses

2.2.1 In situ major element analyses

Major element compositions of olivine grains were measured in NWA 4468, NWA 10618, NWA 10961, NWA 11065, NWA 11043, ALHA 77005, LEW 88516. Major element compositions of pyroxene grains were measured in NWA 4468, NWA 10618, NWA 10961, NWA 11065, NWA 11043, and ALHA 77006. Major element compositions of spinel grains were measured in NWA 4468, NWA 10618, NWA 10961, NWA 11065, NWA 11043. Analyses of olivine, pyroxene, and spinel were conducted using the *JEOL JXA-8900* electron probe microanalyzer (EPMA) housed at the University of Nevada Las Vegas (UNLV), using an accelerating voltage of 15 kV, beam current of 20 nA, beam diameter of 2 μm, and standard ZAF corrections. Major element compositions of maskelynite grains were measured in NWA 4468, NWA 10618, NWA 10961, NWA 11065, and NWA 11043, using an accelerating voltage of 15

kV, beam current of 10 nA, beam diameter of 2 μm, and standard ZAF corrections. Peak counting times were 20 s for Na; 30 s for Fe, K, Mg, Si, Mn, Cr, and Ni; 40 s for Ca; 60s for Ti, Al, and P. Calibrations were conducted daily for silicate and oxide phases using the following standards: olivine (Mg, Si), augite (Mg, Fe), ilmenite (Mn, Fe, Ti), plagioclase (Ca, Al, Si), chromite (Cr), Ni-olivine (Ni), apatite (P), albite (Na), microcline (K). Detection limits were ≤0.01 wt. % for K_2O, MgO, Al_2O_3, CaO, and P_2O_5 and ≤0.02 wt. % for SiO_2, Na_2O, FeO, MnO, Cr_2O_3, TiO_2, and NiO.

Elemental X-ray maps of Mg, Ca, Fe, and Si were produced for all twenty thin sections of the eleven poikilitic shergottite samples, using the *JEOL JXA-8900* EPMA housed at UNLV, with beam conditions set to 15 kV accelerating voltage, 20 nA beam current, pixel dwell time of 9 ms, and step size of 2 µm. Phosphorus elemental X-ray maps of chosen olivine grains within NWA 7755, RBT 04262, ALHA 77005, LEW 88516, NWA 10618, and NWA 11065 were obtained using the *JEOL JXA-8200* Superprobe at Rutgers University, with an accelerating voltage of 15 kV, beam current of 300 nA, pixel dwell time of 500 ms, and step size of 2 µm. Three spectrometers [PET, TAP, and large PET (LPET)] were used simultaneously to measure P kα during P-mapping of olivine grains, in order to maximize counts and increase the signal-to-noise ratio. Modal abundances (vol. %) of mineral phases were calculated through use of *ImageJ* software and employing pixel count analyses of Mg, Ca, Fe, and Si elemental X-ray maps. An error of ~5% was estimated for the modal abundances similar to the supervised image classification method conducted by Maloy and Treiman (2007).

2.2.3 Oxygen fugacity calculations

Olivine-pyroxene-spinel (Ol-Pyx-Sp) oxybarometry and olivine-spinel (Ol-Sp) geothermometry were utilized to calculate oxygen fugacities (fO$_2$) and subsolidus equilibration temperatures, respectively, of both poikilitic and non-poikilitic textures within NWA 4468, NWA 7755, NWA 10618, NWA 10961, NWA 11065, NWA 11043, ALHA 77005, LEW 88516, and RBT 04261/2. (Sack and Ghiorso 1989; 1991a; 1991b; 1994a; 1994b; 1994c; Ballhaus et al., 1991; Wood, 1991; http://melts.ofm-research.org/CORBA_CTserver/Olv_Spn_Opx/index.php). Measurements of olivine-pyroxene-spinel assemblages were taken where the three phases were in contact with one another, suggesting equilibrium and representative fO$_2$ estimates for early- and late- stage crystallization assemblages. Major element compositions of olivine, low-Ca pyroxene, and spinel mineral assemblages were analyzed in the previously mentioned meteorites using the *JEOL JXA-8900* EPMA at UNLV, to conduct fO$_2$ and subsolidus equilibration temperature calculations. To calculate subsolidus equilibration temperatures and fO$_2$ estimates for intermediate NWA 10961, we avoided mineral grains that were in close proximity to areas that had been affected by shock.

2.3 Inductively Coupled Plasma - Mass Spectrometry (ICP-MS)

1.23 g of NWA 7755, 0.50 g of NWA 4468, 1.20 g of NWA 10961, 0.30 g of NWA 11065, and 1.41 g of NWA 11043 were crushed separately in an agate pestle and mortar, solely used for martian samples. The crushed powders were analyzed at *Scripps Isotope Geochemistry Laboratory* (SIGL), which was then digested (along with standards BHVO-2, AGV-1, and BCR-2 and total procedural blanks) in 4 mL of concentrated HF and 1 ml of concentrated HNO$_3$ for >72 hours at on a hot plate. Bulk trace element compositions were measured for the poikilitic shergottite

solutions and the standards, by use of a *ThermoScientific iCAP Q* ICP-MS housed at SIGL. BHVO-2 was used to standardize the analyses. Precision of reference material analyses typically exceeded 5% (relative standard deviation – RSD). The procedures performed for this analytical technique followed those in Day et al. (2015).

2.4 Quantitative textural analyses

Quantitative textural analyses, such as crystal size distribution (CSD) analyses and spatial distribution pattern (SDP) analyses, are well-established and useful tools to investigate physical formation processes and crystallization kinetics of igneous rocks (e.g., Cashman and Marsh, 1988; Marsh, 1988; Jerram et al., 1996; Marsh, 1998; Higgins, 2000; Jerram et al., 2003; Higgins, 2006; Higgins, 2011). Quantitative textural analyses were applied to the olivine crystal populations in ten (NWA 7755, NWA 7397, NWA 4468, NWA 10169, NWA 10618, NWA 11065, NWA 11043, ALHA 77005, LEW 88516, RBT 04261/2) of the poikilitic shergottites within this study. I focused on the olivine populations within my samples because olivine is the most abundant phase, and is an early and prolonged crystallizing phase, within poikilitic shergottites, allowing for statistically sound and comprehensive results on their growth histories to be obtained.

2.4.1 Crystal size distribution (CSD) analyses

One thin section of NWA 7755, NWA 7397, NWA 4468, NWA 10169, NWA 10618, NWA 11065, NWA 11043, ALHA 77005, LEW 88516, RBT 04261, and RBT 04262 was used to conduct CSD analyses, on the poikilitic and non-poikilitic olivine crystal populations, within these poikilitic shergottites. Photomicrographs of each thin section were taken in cross-polarized light (XPL), plane-polarized (PPL), and reflected light, using a Nikon Eclipse LV100 POL polarizing microscope. The photomicrographs were then manually and automatically mosaicked using *Adobe*

Photoshop®. Individual olivine grain boundaries, outlines of analyzed areas, and outlines of each thin section were manually traced in *Adobe Illustrator*®. Delineation of olivine grains and grain boundaries was done with the aid of a combination of photomicrograph mosaics, backscatter electron images, elemental X-ray maps, and optical microscopy. Olivine grains that intersected the perimeter of the thin section were omitted, as they do not represent complete crystals. Additionally, olivine grains with a short axis of <0.03 mm were discarded due to their near equivalence of the thin-section thickness, which increases the possibility that they are not accurate measurements and are just projections of crystals (Higgins, 2000). Digitized images of the grain boundaries and total areas of the thin sections measured were processed using *ImageJ*, which determined the total number of grains analyzed, XY grain center coordinates, grain long and short axis measurements, grain roundness, and area of each grain. Olivine grain axes measurements were processed using *CSDslice* software. *CSDslice* software includes a database containing 703 different crystal shape habits based on known sections and provides a way to stereologically convert the 2-D measured grain populations to true 3-D crystal size distributions (Higgins, 2000; Morgan and Jerram, 2006). The best matching crystal shape ratios (long-, intermediate-, short-axis ratio) calculated with *CSDslice* software were subsequently input into *CSDcorrections* software. *CSDcorrections* software was used to generate CSD plots, and traditionally shows a negative relationship between ln(population density) and crystal size (Cashman and Marsh, 1988; Marsh 1988, Marsh, 1998; Morgan and Jerram, 2006). Crystal growth rates and magma residence times are related to the slope of the CSD plots, which is defined as $m = -1/G\tau$, where *m* represents the slope, *G* represents the growth rate, and τ represents the residence time (Marsh, 1988; 1998).

2.4.2 Spatial distribution pattern (SDP) analyses

Spatial distribution pattern analyses were conducted on the same thin sections, and olivine populations, that were examined for CSD analyses. Images of traced olivine grain boundaries were utilized for SDP analyses to obtain the R-value and porosity (% melt at the time of solidification) of the sample analyzed. The R value is defined as: $R = 2(\sqrt{\rho}\Sigma r)/N$, where ρ is the observed population density, r is the distance between the centers of two neighboring crystals, and N is the number of crystals in the population (Jerram et al., 1996; 2003). The R-values for each sample were calculated based on the technique demonstrated in Jerram et al. (1996) using the *Big-R* software available in *CSDcorrections* software. The percentage of melt at the time of solidification of the entire olivine population was estimated from olivine modal mineral abundances that were calculated from pixel count analyses of the digitized olivine grain boundary images using *ImageJ*.

3. Results

3.1 Petrography

Enriched and intermediate poikilitic shergottites of this study all display characteristic bimodal textures, consisting of both poikilitic and interstitial non-poikilitic textures, similar to what has been previously described in the literature (Fig. 1a and 1b) (e.g., McSween et al., 1979; Harvey et al., 1993; Gleason et al., 1997; Gillet et al., 2005; Mikouchi, 2005; Mikouchi and Kurihara, 2008; Usui et al., 2010; Jiang and Hsu, 2012; Walton et al., 2012; Howarth et al., 2014; 2015; Combs et al., 2018). The poikilitic textures are comprised of medium- to coarse- pyroxene oikocrysts that partly or completely enclose multiple olivine and spinel chadacrysts (Fig. 1a and 1b), except in the case of NWA 11065, where some pyroxene oikocrysts are devoid, and nearly devoid, of mineral inclusions. The textural terms "oikocryst" and "chadacryst" refer to a large crystal (oikocryst) that fully contains smaller mineral inclusions (chadacrysts). In all samples, pyroxene oikocrysts are ovoid and range in maximum length from ~3.4 mm (oikocryst of NWA 11043) to ~10.5 mm (oikocrysts of NWA 11065 and NWA 7755; Fig. 6). Olivine chadacrysts range in length up to 1.8 mm and are subhedral to anhedral. Olivine chadacrysts of enriched poikilitic shergottites occasionally enclose small (<100 μm) euhedral spinel, whereas those of intermediate poikilitic shergottites typically do not.

Dissimilar to the poikilitic textures, non-poikilitic textures consist of more diverse mineral assemblages, which are found interstitial to pyroxene oikocrysts (Fig. 1a and 1b). Phases found within non-poikilitic textures include pyroxene, olivine, maskelynite (shocked plagioclase), spinel, ilmenite, phosphates (apatite and merrillite), and sulfides (pyrrhotite). Non-poikilitic olivine grains range in maximum length from 1.3 mm (ALHA 77005) to 3.8 mm (NWA 7397). Non-poikilitic olivine grains are also more abundant, more euhedral, and typically in contact with one another,

when compared to poikilitic olivine grains. Pigeonite and augite pyroxene grains are found within non-poikilitic textures; however, they do not display the same zoning patterns as poikilitic pyroxene grains. Interstitial pyroxene grains are also subhedral to anhedral and vary considerably in size between individual samples (~50 μm to 1000 μm). Maskelynite (shocked plagioclase) of all poikilitic shergottites predominantly occurs within non-poikilitic textures, interstitial to poikilitic pyroxene, which is what I also observe. (e.g., Ikeda, 1997; Usui et al., 2010; Jiang and Hsu, 2012; Howarth et al., 2014; 2015; Combs et al., 2018). Maskelynite grain sizes are variable between samples with a range of ~20 μm to 1500 μm. Phosphate grains exist as laths within non-poikilitic textures, with an average length of ~100 μm. Non-poikilitic spinel grains are euhedral and spatially associated with non-poikilitic olivine located either within, or adjacent to, olivine grains. Non-poikilitic spinel grains are also generally larger than poikilitic spinel grains, ranging in length up to ~300 μm. Ilmenite grains are found in association with spinel and are fine-grained (<100 μm). Sulfide grains are typically fine-grained in poikilitic shergottites, as is the case for sulfides of this study, with the exception of a ~600 μm long pyrrhotite grain found in one thin section of NWA 10961 (Figs. 2 and 3).

Poikilitic shergottites have all been affected by shock upon ejection from Mars, resulting in pervasive fracturing, darkening of olivine grains, transformation of plagioclase to maskelynite, and formation of shock veins and melt pockets (e.g., McSween et al., 1979; Harvey et al., 1993; Treiman et al., 1994; Gleason et al., 1997; Gillet et al., 2005; Mikouchi, 2005; Walton and Herd, 2007; Mikouchi and Kurihara, 2008; Usui et al., 2010; Jiang and Hsu, 2012; Walton et al., 2012; Howarth et al., 2014; 2015; Takenouchi et al., 2017; Combs et al., 2018). As ALHA 77005, LEW 88516, RBT 04261/2, NWA 7397, NWA 7755, and NWA 10169 have all been previously described (e.g., Harvey et al., 1993; Treiman et al., 1994; Walton and Herd, 2007; Usui et al.,

2010; Howarth et al., 2014; 2015; Combs et al., 2018, respectively), I focus only on the results of shock for NWA 4468, NWA 10618, NWA 11043, NWA 11065, and NWA 10961. Pervasive fracturing is apparent in all five poikilitic shergottites. Olivine grains within NWA 10618, NWA 11043, NWA 11065, and NWA 10961 are darkened to the extent that they are nearly opaque. Shock melt pockets and shock melt veins exist in all five samples;, however, the results of shock are most prominent in NWA 10961, where both analyzed thin sections contain transecting ~2 mm to 5 mm wide shock melt zones. I adopt the term "zone" over "vein", as there are offshoots of melt and no clear melt path. The shock melt boundaries are clearly distinguished through a pyroxene oikocryst with a less sharp contact through the interstitial phases. The host rock and shock melt contacts are gradational, with grain sizes becoming coarser toward interior regions. Opposing walls to the shock melt zones are generally irregular. Olivine is the dominant phase in the shock melt, and grains are micron-sized on average. Along the shock melt boundary within the non-poikilitic texture, olivine boundaries have been recrystallized and incorporated into the shock zone.

I report mineral modal abundances for the 11 samples Table 1. There are slight variations between previously reported modal abundances and those reported here, which are likely due to the heterogeneous nature of poikilitic shergottites (Treiman et al., 1994; Usui et al., 2010; Howarth et al., 2014; 2015; Combs et al., 2018). In general, modal abundances for all phases within enriched poikilitic shergottites of this study overlap with those of intermediate, with the most abundant phases being olivine (30 vol.% to 63 vol.%), low-Ca pyroxene (13 vol.% to 44 vol.%), high-Ca pyroxene (8.4 vol.% to 17 vol.%), and maskelynite (3.6 vol.% to 23 vol.%). Minor phosphates (0.4 vol.% to 2.1 vol.%) and spinel (0.1 vol.% to 1.6 vol.%), and trace ilmenite and sulfides are also present (Table 1). Enriched NWA 11043 contains the greatest abundance of olivine of all analyzed samples, with a modal abundance of 63 vol.%, and the least abundance of low-Ca pyroxene (13

vol.%) (Fig. 2a). Enriched RBT 04261 contains the highest amount of maskelynite (23 vol.%) (Fig. 2b), while intermediate NWA 10961 contains the lowest (3.6 vol.%) (Fig. 2c). Intermediate NWA 10961, ALHA 77005, and LEW 88516 of this study contain notable shock melt abundances of 14 vol.%, 6.4 vol.%, and 4.4 vol.%, respectively (Table 1).

3.2 Bulk rock trace element compositions

Bulk rock trace element compositions were measured for NWA 10961, NWA 11065, NWA 7755, NWA 4468, and NWA 11043, and were compared to data previously obtained for ALHA 77005, LEW 88516, RBT 04262, and NWA 10169 (Table 2 and Fig. 4) (Lodders, 1998; Anand et al., 2008; Usui et al., 2010; Tait and Day, 2018; Combs et al., 2018). Northwest Africa 10961 and NWA 11065 have $(La/Yb)_{CI}$ values of 0.41 and 0.43, which are similar to values reported for intermediate poikilitic shergottites (0.30–0.50) (e.g., Lodders, 1998; Gillet et al., 2005; Bridges and Warren, 2006; Lin et al., 2008; Tait and Day, 2018). Thus, newly recovered NWA 10961 and NWA 11065 have intermediate LREE-enrichments. Northwest Africa 4468 has relatively flat LREE-profiles and a $(La/Yb)_{CI}$ value of 1.11, classifying it as an enriched poikilitic shergottite. A bulk rock REE pattern of NWA 7755 has been calculated by Howarth et al. (2015), using measured mineral REE compositions and modal abundances. Calculations of Howarth et al. (2015) showed NWA 7755 to be an enriched poikilitic shergottite [bulk rock $(La/Yb)_{CI} = 1.1$], with close affinity to enriched shergottites. The calculated bulk rock $(La/Yb)_{CI}$ is similar to my measured value [$(La/Yb)_{CI} = 0.98$] (Table 2). Newly recovered NWA 11043 has the greatest $(La/Yb)_{CI}$ value of mysamples, with a value of 1.59, thus classifying it as a new enriched poikilitic shergottite (Table 2 and Fig. 4). The measured $(La/Yb)_{CI}$ values (0.98 – 1.59) of NWA 7755, NWA 4468, and NWA 11043 all coincide with values reported for enriched poikilitic shergottites

[(La/Yb)$_{CI}$ >0.8] (e.g., Usui et al., 2010; Howarth et al., 2014; 2015; Combs et al., 2018). Slight positive Eu anomalies are observed for NWA 11065, NWA 10961, and NWA 11043, with Eu/Eu* ([Eu$_{CI}$/(Sm$_{CI}$ × Gd$_{CI}$)$^{1/2}$]) values of 1.09, 1.04, and 1.26 (Table 2), respectively, similar to that of NWA 10169 (1.14) (Combs et al., 2018). A slight negative Eu/Eu* anomaly of 0.93 is observed for NWA 7755, which is close to the value of 0.91 for RBT 04262 (Anand et al., 2008). In addition, NWA 11043 displays a negative Ce anomaly [Ce/Ce* = Ce$_{CI}$/(La$_{CI}$ × Pr$_{CI}$)$^{1/2}$] of 0.61. I also observe elevated concentrations of Ba in NWA 11043 (682 ppm) and NWA 7755 (154 ppm), as well as elevated concentrations of Sr in NWA 11043 (~52 ppm), NWA 7755 (~40 ppm), NWA 4468 (~44 ppm), NWA 11065 (~31 ppm), and NWA 10961 (~31 ppm) (Table 2).

3.3 Mineral compositions

3.3.1 Olivine

I obtained major element compositions of poikilitic and non-poikilitic olivine grains for intermediate poikilitic shergottites ALHA 77005, LEW 88516, NWA 10961, and NWA 11065, and enriched poikilitic shergottites NWA 4468, NWA 11043, and NWA 10618 (Table 3 and Fig. 5). Individual poikilitic and non-poikilitic olivine grains in all analyzed samples show no compositional zoning of major elements.

3.3.1.1 Olivine of intermediate poikilitic shergottites

Poikilitic olivine chadacrysts of NWA 10961, ALHA 77005, and LEW 88516 have similar compositions of Fo$_{70-77}$, Fo$_{71-77}$, Fo$_{67-75}$ (Fig. 5), respectively. Olivine major element compositions acquired for intermediate ALHA 77005 and LEW 88516 are in close agreement with previous reports (ALHA 77005: Fo$_{69-77}$ and LEW 88516: Fo$_{62-73}$) by McSween et al. (1979a), Harvey et al. (1993), and Treiman et al. (1994), with minor differences, likely due to the heterogeneity of

coarse-grained, cumulate poikilitic shergottites. Poikilitic olivine of intermediate poikilitic shergottite NWA 11065 has a compositional range of Fo_{58-68}. Chadacrysts of NWA 11065 are the most ferroan of all intermediate poikilitic shergottites (Fig. 5) (e.g., McSween et al., 1979a; Treiman et al., 1993; Harvey et al., 1994; Ikeda, 1997; Hsu et al., 2004; Lin et al., 2005, Walton and Herd, 2007; Walton et al., 2012).

Non-poikilitic olivine grains of poikilitic shergottites are more ferroan than olivine chadacrysts, consistent with previous results (e.g., Treiman et al., 1993; Harvey et al., 1994; Hsu et al., 2004; Walton and Herd, 2007; Usui et al., 2010; Howarth et al., 2014; 2015; Combs et al., 2018). Non-poikilitic olivine grains of NWA 10961 (Fo_{68-71}) have a similar compositional range to that of ALHA 77005 (Fo_{70-74}). The non-poikilitic olivine grains of LEW 88516 and NWA 11065 are more Fe-rich, with compositions of Fo_{63-67} and Fo_{54-63} (Fig. 5), respectively.

3.3.1.2 Olivine of enriched poikilitic shergottites

Enriched poikilitic shergottites contain olivine grains that are more Fe-rich than olivine of intermediate poikilitic shergottites (e.g., Usui et al., 2010; Jiang and Hsu, 2012; Howarth et al., 2014; 2015; Combs et al., 2018). I find this to generally be the case for poikilitic olivine chadacrysts of enriched NWA 4468, NWA 10618, and NWA 11043, which have poikilitic Fo contents of 59–69, 62–66, and 65–70, respectively (Fig. 5). These values overlap with poikilitic olivine compositions of other enriched poikilitic shergottites (e.g., Usui et al., 2010; Howarth et al., 2014; 2015; Combs et al., 2018). However, poikilitic olivine chadacrysts of enriched poikilitic shergottites are more Mg-rich than that of aforementioned intermediate poikilitic shergottite NWA 11065 (Fo_{58-68}) (Fig. 5). These compositions contrast with previous studies mentioning that enriched poikilitic shergottites contain more Fe-rich olivine than intermediate varieties (e.g., Usui et al., 2010; Howarth et al., 2014; 2015; Combs et al., 2018).

Similar to intermediate poikilitic shergottites, non-poikilitic olivine grains of enriched poikilitic shergottites have lower forsterite (Fo) contents than their poikilitic olivine chadacrysts (e.g., Mikouchi and Kurihara, 2008; Usui et al., 2010; Jiang and Hsu, 2012; Howarth et al., 2014; 2015; Combs et al., 2018). Forsterite content of non-poikilitic olivine of enriched poikilitic shergottites NWA 10618, NWA 4468, and NWA 11043 ranges from 58–66, with NWA 4468 containing non-poikilitic olivine with the lowest Fo and NWA 11043 with the highest (Fig. 5). In general, enriched poikilitic shergottites have non-poikilitic olivine compositions that overlap with, or are more Fe-rich than, intermediate poikilitic shergottites. Yet, departure from this is observed for intermediate NWA 11065, which has the most Fe-rich non-poikilitic olivine (Fo_{54-63}) of all analyzed samples (Fig. 5).

3.3.2 Pyroxene

Poikilitic shergottites pyroxene oikocrysts are chemically zoned, having low-Ca cores and thick, irregular high-Ca rims (Fig. 6) (e.g., Treiman at al., 1993; Harvey et al., 1994; Mikouchi, 2005; Mikouchi and Kurihara, 2008; Usui et al., 2010; Howarth et al., 2014; 2015; Combs et al., 2018). Pyroxene oikocrysts within intermediate ALHA 77005, NWA 10961, and NWA 11065, and enriched NWA 4468, NWA 11043, and NWA 10618, display abrupt compositional boundaries between low-Ca cores ($Wo_3En_{55}Fs_{21}$–$Wo_{17}En_{77}Fs_{21}$) and high-Ca rims ($Wo_{27}En_{53}Fs_{20}$–$Wo_{38}En_{48}Fs_{14}$). Low-Ca pyroxene oikocryst cores of ALHA 77005 and NWA 10961 have the same average Mg#s (molar 100*Mg/[Mg+Fe]) as their high-Ca pyroxene oikocryst rims, with values of 78 and 77, respectively, which are also the highest average Mg#s for pyroxene within my study. Intermediate NWA 11065, however, has the lowest average Mg#s for oikocrysts (low-Ca: Mg# 70, high-Ca: Mg# 71). These values closely overlap with those of enriched poikilitic shergottites

NWA 4468, NWA 11043, NWA 10618, RBT 04261/2, NWA 7755, and NWA 10169 (Table 4 and Fig. 5) (e.g., Usui et al., 2010; Howarth et al., 2015; Combs et al., 2018).

Non-poikilitic low-Ca and high-Ca pyroxene exist as distinct grains, and do not exhibit core- to rim- zoning like pyroxene oikocrysts. Non-poikilitic low-Ca pyroxene grains of enriched and intermediate poikilitic shergottites are typically more Fe-rich than pyroxene oikocryst cores, having average Mg#s ranging from 63–73 and 66–68, respectively (Table 4). Poikilitic and non-poikilitic high-Ca pyroxene of both geochemical types show more compositional overlap than low-Ca pyroxene in both textures (Fig. 5).

Furthermore, intermediate poikilitic shergottites generally contain non-poikilitic pyroxene grains that are more Mg-rich than enriched poikilitic shergottites (e.g., Treiman at al., 1993; Harvey et al., 1994; Mikouchi, 2005; Mikouchi and Kurihara, 2008; Usui et al., 2010; Howarth et al., 2014; 2015; Combs et al., 2018). I find this to be the case for NWA 10961 and ALHA 77005, which have an identical low-Ca non-poikilitic pyroxene average composition of $En_{66}Fs_{24}Wo_{10}$, and similar high-Ca pyroxene compositions of $En_{52}Fs_{16}Wo_{32}$ and $En_{50}Fs_{15}Wo_{36}$, respectively (Table 4) (e.g., Harvey et al., 1994; Mikouchi, 2005). I find the opposite to be true for intermediate NWA 11065, which has the most Fe-rich non-poikilitic pyroxene of all poikilitic shergottites (low-Ca: $En_{54}Fs_{32}Wo_{13}$; high-Ca: $En_{52}Fs_{16}Wo_{32}$) (Fig. 5).

3.3.3 Maskelynite

I have measured element compositions of maskelynite for five poikilitic shergottites (NWA 10961, NWA 11065, NWA 10168, NWA 4468, and NWA 11043) (Table 5 and Fig. 7). Maskelynite within NWA 10961, NWA 11065, NWA 4468, and NWA 11043 have similar average compositions, ranging from $An_{50–57}Ab_{42–47}Or_{1–3}$, and mostly fall within the range of maskelynite compositions of previously analyzed intermediate poikilitic shergottites (Fig. 7). Northwest Africa

4468 has the widest maskelynite compositional range of $An_{39-57}Ab_{42-57}O_{2-6}$, which is similar to the range of maskelynite ($An_{34-56}Ab_{44-57}Or_{2-6}$) within enriched NWA 10169 (Combs et al., 2018). Although there is some compositional variation between individual maskelynite grains in all five analyzed samples, I observe no chemical zoning from cores to rims of maskelynite grains.

3.3.4 Spinel

Spinel chadacrysts of enriched and intermediate poikilitic shergottites are chromites and are generally more Cr-rich, in comparison to the more Ti-rich spinel grains of the non-poikilitic interstitial textures (Table 6 and Fig. 8), similar to findings of previous studies (e.g., Lin et al., 2005; Usui et al., 2010; Jiang and Hsu, 2012; Walton et al., 2012; Howarth et al., 2014; 2015; Combs et al., 2018). Non-poikilitic spinel grains within enriched poikilitic shergottites are generally more Ti-rich than that of the intermediate poikilitic shergottites (average TiO_2: 9.5 wt.% versus 6.4 wt.%). I observe this trend for non-poikilitic spinel grains of enriched poikilitic shergottites NWA 4468, NWA 11043, and NWA 10618 (with average spinel compositions from $Chr_{51}Spn_{14}Ulv_{36}$ to $Chr_{44}Spn_{13}Ulv_{43}$), when compared to spinel of intermediate poikilitic shergottite NWA 10961 (average composition of $Chr_{53}Spn_{14}Ulv_{33}$). Deviation from this trend is seen when comparing the average non-poikilitic spinel composition ($Chr_{30}Spn_{10}Ulv_{60}$) of intermediate NWA 11065. Northwest Africa 11065 also has the most Ti-rich spinel grains analyzed in any poikilitic shergottite (Fig. 8).

3.4 Oxygen fugacity and subsolidus equilibration temperature

Oxygen fugacity and subsolidus equilibration temperature calculations were conducted to examine the magmatic formation conditions and evolutions of enriched and intermediate poikilitic shergottites. Results of my fO_2 and subsolidus equilibration temperature calculations are summarized in Table 7 and Figure 9. I have calculated fO_2 for both poikilitic and non-poikilitic textures in all poikilitic shergottites of this study, except for NWA 7397 and NWA 10169. For all samples, an increase in fO_2, ranging from 1.2 to 2.9 log units, occurs from the poikilitic texture to the non-poikilitic texture. This relationship has been seen before in enriched poikilitic shergottites NWA 7397, NWA 7755, and NWA 10169 (Howarth et al., 2014; 2015; Combs et al., 2018), as well as in intermediate poikilitic shergottite NWA 4797 (Walton et al., 2012). The early-stage fO_2 for NWA 10961 is the most reduced of all poikilitic shergottites, being four log units below the Quartz-Fayalite-Magnetite (QFM) buffer (Fig. 9 and Table 7). Although early-stage fO_2 of NWA 10961 is more reduced than other intermediate poikilitic shergottites, later-stage fO_2 (QFM -1.35) of NWA 10961 is more oxidized than that of ALHA 77005, LEW 88516, and NWA 4797, which have QFM values of -1.68, -1.59, and -1.7 (Walton et al., 2012), respectively (Table 7). The largest increase in fO_2 is seen for intermediate poikilitic shergottite NWA 11065, from -3.3 log units below the QFM buffer (poikilitic) to QFM-0.5 (non-poikilitic). The non-poikilitic fO_2 of NWA 11065 is also the most oxidized value of all analyzed samples. In addition, poikilitic fO_2 estimates calculated for intermediate poikilitic shergottite of this study (QFM -3.3 to -4.1) all overlap with previously reported fO_2 estimates of depleted olivine-phyric and basaltic shergottites, such as Tissint (QFM ~-4.0), Sayh al Uhaymir (SaU) 005 (QFM ~-3.4), and Queen Alexandra Range (QUE) 94201 (QFM ~-3.5) (e.g., Herd, 2003; Balta et al., 2015; Castle and Herd, 2017).

In addition to an increase in fO$_2$ from the poikilitic to non-poikilitic textures, a decrease in subsolidus equilibration temperatures is seen between the two textural regions for all samples. Subsolidus equilibration temperatures are similar for both textures of enriched and intermediate poikilitic shergottites (Table 7). Poikilitic subsolidus equilibration temperatures range from 1032 °C to 1101 °C for enriched poikilitic shergottites and from 1089 °C to 1185 °C for intermediate poikilitic shergottites. Non-poikilitic subsolidus equilibration temperatures are lower than poikilitic temperatures, with ranges of 800 °C to 932 °C for enriched poikilitic shergottites and from 850 °C to 947 °C for intermediate poikilitic shergottites. These subsolidus equilibration temperatures are consistent with temperatures obtained for other poikilitic shergottites (e.g., Howarth et al., 2014; 2015; Combs et al., 2018).

3.5 Quantitative textural analyses

Olivine crystallization histories and emplacement of enriched and intermediate poikilitic shergottites were investigated using quantitative textural analyses. I have measured olivine populations of all poikilitic shergottites within this study for quantitative textural analyses, with the exception of NWA 10961, as the shock melt veins would obscure true igneous olivine crystallization histories. Crystal size distribution results are presented in Tables 8–10 and Figures 10–12. Shapes of olivine grains are described as rectangular prisms, thus allowing for statistically significant CSD results to be obtained with populations of 75 grains or more (Morgan and Jerram, 2006). I have measured more than 500 olivine grains in each examined thin section, except for in LEW 88516,22, which only contained 246 grains. In addition to conducting CSD for all measured olivine grains within each thin section, textural analyses of poikilitic and non-poikilitic olivine grains were measured, as separate populations. However, due to the limited number of olivine

grains in each textural region, CSD was only applied to poikilitic and non-poikilitic olivine grains of five enriched (NWA 4468, NWA 10169, NWA 7755, RBT 04262, NWA 11043), and two intermediate (ALHA 77005, NWA 11065) rocks, as they were the only samples that contained 75 or more olivine grains within each textural region (Tables 9 and 10; Fig. 12). The best-fit ratios (representing the short- intermediate- long axis ratio of the three-dimensional crystal shape) of olivine populations of enriched poikilitic shergottites vary from 1.00:1.15:1.60 to 1.00:1.30:2.40, while the intermediate poikilitic shergottites have a variation of 1.00:1.15:1.70 to 1.00:1.25:1.70 (Tables 8–10). Nearly all CSD profiles for both enriched and intermediate poikilitic shergottites show similar overall negative concave-up sublinear slopes (Figs. 10 and 12), with the exception being NWA 11043, which displays a negative linear slope (Figs. 10 and 12). All CSD profiles contain a downturn at the smallest grain size bins (≤0.1 mm) (Figs. 10 and 12). For this reason, we have calculated CSD slopes with and without the grains of the smallest olivine grain size bins (≤0.1 mm) (Tables 8–10). Overall CSD length profile slopes (excluding smallest grain size bins) for enriched poikilitic shergottites range vary from -3.42 to -8.06, and intermediate poikilitic shergottite CSD slopes vary from -3.32 to -6.75. Intercepts of the CSD length profiles for enriched poikilitic shergottites vary from 3.16 to 5.97, and intermediate poikilitic shergottite CSD intercepts vary from 3.68 to 5.27. We observe a negative correlation between corrected CSD slopes and intercepts for both enriched and intermediate poikilitic shergottites, with paired RBT 04261 and RBT 04262 having the steepest and NWA 10169 having the shallowest slope for enriched poikilitic shergottites; NWA 11065 has the steepest slope, and LEW 88516 has the shallowest slope, of intermediate poikilitic shergottites (Tables 8–10; Fig. 11a). A positive correlation is observed between CSD slope and average olivine grain size, with RBT 04261/2 exhibiting the smallest average grain size and LEW 88516 the largest (Fig. 11b). I observe no correlations

between olivine CSD slopes and modal abundances or olivine average sizes and modal abundances (Figs. 11c and 11d). Non-poikilitic olivine populations for NWA 10169, RBT 04262, NWA 11043, and ALHA 77005, and NWA 11065 all have shallower corrected slopes than their poikilitic counterparts, while non-poikilitic slopes of NWA 4468 and NWA 7755 are steeper than their poikilitic slopes (Tables 9 and 10; Fig. 12). Overall intercepts for all non-poikilitic olivine populations of all seven samples are greater than those of the poikilitic populations, ranging from 3.63 to 5.52 in comparison to 2.84 to 5.13 (Tables 9 and 10). I observe general overall negative correlations between corrected slopes and intercepts for both the poikilitic and non-poikilitic populations.

As CSD slopes are related to crystal growth rates and magma residence times (see Crystal Size Distribution analyses section) (Marsh 1988; 1998), I calculated estimates of olivine residence times, resulting in 46–109 (enriched poikilitic shergottites) and 66–112 (intermediate poikilitic shergottites) Earth days (Tables 8–10). Due to the unavailability of experiments on olivine growth in poikilitic shergottite magmas, I obtained estimates using a growth rate of ~$3.1x10^{-8}$ mm/s, which was calculated based off of Fe-Mg diffusion profiles from olivine grains of the enriched olivine-phyric shergottite Larkman Nunatak (LAR) 06319 (Basu Sarbadhikari et al., 2009). This growth rate is similar to growth rates calculated for silicate minerals in terrestrial rocks (Marsh, 1998; Jerram et al., 2003), as well as in lunar and martian meteorites (Day and Taylor, 2007; Day et al., 2006a). However, magma residence times should be used with caution, as they can change considerably with slight variations in growth rates (e.g., Ennis and McSween, 2014; Udry and Day, 2017). I observe no clear correlations between reciprocal of residence time and CSD slope/CSD intercept (Fig. 11e).

Spatial distribution pattern analyses show that nine of the examined poikilitic shergottites plot within the clustered touching framework field, with the two exceptions of NWA 11065 and NWA 7755 plotting on the boundary, and within, the clustered non-touching framework field, respectively (Fig. 13). Phenocryst populations within cumulate rocks typically plot within the clustered touching framework field (Jerram et al., 2003). However, olivine grains of NWA 7755 and NWA 11065 are more widely distributed than typical cumulate rocks due to the large lengths of pyroxene oikocrysts within NWA 11065 (10.6 mm) and NWA 7755 (10.8 mm) that surround them (Fig. 5).

3.6 Phosphorus zonation patterns in olivine

To compare olivine growth histories within enriched and intermediate poikilitic shergottites, I measured P maps in several samples. I produced P maps for two olivine grains within enriched poikilitic shergottites NWA 10618 and NWA 7755, as well as two olivine grains within intermediate poikilitic shergottites ALHA 77005, LEW 88516, and NWA 11065, with one olivine grain (or one composite grain) mapped from each textural domain (Fig. 14a – Fig. 14j). I also mapped olivine grains within RBT 04262, but was unable to distinguish P patterns due to fractures causing false P enrichments.

I observe P maps of poikilitic olivine within NWA 10618, NWA 7755, and ALHA 77005 to contain similar dominant features, such as wide (~175 to 250 μm) P-poor centers, few nearly continuous alternating P-rich and P-poor bands that vary in thickness and enrichments, and resorbed olivine boundaries (Fig 14a – Fig. 14c). A P-poor melt inclusion lies at the NWA 10618 phenocryst center and is surrounded by a P-rich rim (Fig. 14a). This olivine also shows a dendritic P-rich band, consisting of a euhedral P-rich band with P-rich "branch" zonations projecting from the corners (Fig. 14a).

The centers of the poikilitic olivine grains within intermediate LEW 88516 and NWA 11065 show P-enrichments (Figs. 14d and 14e). A composite poikilitic olivine grain was mapped within LEW 88516, and both grain centers are P-rich (Fig. 14d). However, the larger grain (~850 μm long) shows a euhedral P-rich center (~250 μm long) that is surrounded by a less P-rich mantle, while the smaller grain (~500 μm) center contains a dendritic P-rich zone (Fig. 14d). Following the P-rich regions in the centers of both grains are alternating continuous and discontinuous P-poor and P-rich bands, with varying thicknesses and enrichments. The P-rich center of poikilitic olivine

grain of NWA 11065 is thinner (~25 μm wide) (Fig. 14e) than that of LEW 88516. The P-rich center is mantled by a P-poor region that is then surrounded by alternating P-rich and P-poor bands.

Phosphorus-zoning patterns of non-poikilitic olivine grains within NWA 10618, NWA 7755, and ALHA 77005 (Fig. 14f – Fig. 14h) are more complex than that of LEW 88516 and NWA 11065 (Figs. 14i and 14j). The dominant features of the non-poikilitic olivine P-maps of NWA 10618, NWA 7755, and ALHA 77005 are P-poor cores (~125 to 500 μm wide) that are surrounded by nearly continuous outer core- to rim- oscillatory subhedral P-zoning patterns (Fig. 14f – Fig. 14h). Intermediate ALHA 77005 non-poikilitic map displays a large (~1 mm long) composite crystal containing two components that both have euhedral to subhedral P-poor cores (Fig. 14h). In addition, at one edge of the larger component, there is a dendritic zonation that is more P-rich than the rest of the crystal. While P-zoning patterns of non-poikilitic olivine grains of enriched NWA 7755 and NWA 10618 are most similar to each other, clear differences exist between the two. Non-poikilitic olivine grain of NWA 10618 contains a P-poor melt inclusion at its center (Fig. 14f). A higher degree of discontinuity of P-bands, within NWA 10618 compared to NWA 7755, can also be seen at the bottom right of the crystal of NWA 10618, where a large P-poor zone is surrounded by curved and wispy oscillatory P-zoning.

The non-poikilitic P-maps of LEW 88516 and NWA 11065 are different from one another (Figs. 14i and 14j). The P-map of non-poikilitic olivine of LEW 88516 contains a P-rich melt inclusion at its center, surrounded by a P-poor mantle, which is then surrounded by alternating P-rich and P-poor bands that show offset faulting. The non-poikilitic olivine P-map of NWA 11065 shows a composite olivine, with four components (Fig. 14j). The larger component crystal (~1 mm long) is nearly P free, with only a few fine-scale P-rich and P-poor bands alternating near the

crystal boundary. The three smaller components show similar P-patterns, displaying euhedral P-rich centers surrounded by a P-poor region and fine-scale oscillatory P-zonings (Fig. 14j).

4. Discussion

4.1 Secondary processes in poikilitic shergottites

The textures, mineralogies, and bulk compositions of poikilitic shergottites have been modified to varying extents due to secondary processes, such as shock metamorphism and terrestrial alteration (e.g., Crozaz and Wadhwa, 2001; Nyquist, 2001; Crozaz et al., 2003; Walton and Spray, 2003; Walton et al., 2012; Howarth et al., 2014; Howarth et al., 2018; Combs et al., 2018). As such, it is important to distinguish the modifications that have occurred to the primary igneous textures and compositions of poikilitic shergottites post-crystallization, in order to avoid inaccurate interpretations regarding igneous magmatic characteristics and emplacement mechanisms.

4.1.1 Shock melting

Poikilitic shergottites have endured large-scale impact events leading to their ejections from Mars and subsequent arrivals on Earth (e.g., Nyquist et al., 2001; Fritz et. al., 2005). Consequently, processes such as shock melting and metamorphism have caused phase transformations, recrystallization of mineral phases, and the formation of shock melt pockets, veins, and zones, within poikilitic shergottite meteorites (e.g., Gillet, 2005; Walton and Herd, 2007; Walton et al., 2012; Howarth et al., 2015). An array of shock melt features has been described in poikilitic shergottites, such as ALHA 77005, LEW 88516, NWA 1950, and NWA 4797 (e.g., Mikouchi, 2005; Walton and Herd, 2007; Walton et al., 2012; Takenouchi et al., 2018), exemplifying the diversity of shock effects on original igneous texture and composition. I use these examples as comparisons for shock features of poikilitic NWA 4468, NWA 10618, NWA 11043, NWA 11065, and NWA 10961.

Multiple shock effects on mineral structure and appearance are seen in poikilitic shergottites, helping constrain shock Pressure-Temperature (P-T) conditions. The most prevalent shock feature found in shergottite meteorites is the phase transformation of plagioclase to the diaplectic glass maskelynite (e.g., Fritz et al., 2005; Fritz et al., 2017). Plagioclase within poikilitic shergottites NWA 4468, NWA 10618, NWA 11043, NWA 11065, and NWA 10961 has all been converted to maskelynite. The refractive index of this mineral has been used to measure peak shock pressures in other shergottites, including poikilitic shergottites ALHA 77005 and LEW 88516, recording values between 30–55 GPa (e.g., McSween and Stöffler, 1980; Keller et al., 1992; Nyquist et al., 2001; Fritz et al., 2005). An additional shock effect on poikilitic shergottite minerals is the darkening/browning of olivine grains, which specific causal process has been highly debated (e.g., Treiman et al., 2007; Van de Moortéle et al., 2007a; 2007b; Bläβ et al., 2010; Takenouchi et al., 2017; 2018), but is attributed to the precipitation of iron nanoparticles within the olivine structure upon shock (e.g., Takenouchi et al., 2017; 2018). Darkened olivine is found within NWA 10618, NWA 11043, NWA 11065, and NWA 10961, similar to other poikilitic shergottites, such as ALHA 77005, LEW 88516, and NWA 1950 (e.g., Ostertag et al., 1984; Gillet et al., 2005; Mikouchi et al., 2005; Takenouchi et al., 2017; 2018). The presence of darkened olivine may signify high pressure shock events with high postshock temperatures (>895–925 K), as suggested by Takenouchi et al. (2018). Contrarily, I do not see darkened olivine grains within NWA 4468, similar to previous reports for RBT 04261/2, suggesting lower shock pressures and temperatures than shergottites with brown olivine grains (e.g., Takenouchi et al., 2018). In addition, I report the largest sulfide grain within a martian meteorite, found bordering a shock melt boundary within NWA 10961 (Fig. 3). Recrystallization of mineral phases occurs during shock events and could be responsible for the formation of the pyrrhotite grain in NWA 10961. As sulfide minerals are

readily melted prior to silicates, recrystallization to form larger sulfide grains is possible due to shock metamorphism (e.g., Ahrens et al., 1969; Jeanloz and Ahrens, 1976).

Relative cooling rates of post-crystallization shock melting can also be constrained using textures of shock melt features (e.g., Mikouchi and Kurihara, 2008; Walton et al., 2012). Northwest Africa 10961 is the only newly described sample of this study that contains a notable modal abundance of shock melt (Table 1). Interaction between the shock melt and interstitial phases of NWA 10961 suggests a slower cooling rate after shock-melting, similar to some shock melt features of ALHA 77005, LEW 88516, and NWA 4797 (e.g., Walton and Herd, 2007; Walton et al., 2012; Takenouchi et al., 2018). Slightly faster cooling of NWA 10961 shock melt may have occurred throughout the pyroxene oikocryst, as seen by the sharper shock melt/host rock contacts within it.

By compiling shock effects of the five relatively newly recovered poikilitic shergottites, I propose a relative potential shock degree sequence. As NWA 4468 exhibits only maskelynite and no darkened olivine or significant shock melt features, I believe it to be the least shocked, comparable to shock degree of RBT 04261/2 (e.g., Usui et al., 2010; Takenouchi et al., 2018). While NWA 10618, NWA 11043, NWA 11065 may have been shocked to greater, and similar degrees, based on presence of maskelynite and darkened olivine, and absence of substantial shock melt. Northwest Africa 10961 was likely shocked to the greatest degree as seen by maskelynization of plagioclase, darkened olivine, and extensive *in situ* melting, similar to ALHA 77005, LEW 88516, and NWA 4797 (e.g., Walton and Herd, 2007; Takenouchi et al., 2018). However, it is important to note that shock pressures and temperatures can be heterogeneous throughout one sample, thus this model is not precise.

4.1.2 Terrestrial contamination

Martian meteorite samples retrieved from cold and hot desert environments, such as those located in Antarctica and Northwest Africa, are susceptible to terrestrial alteration (e.g., Crozaz and Wadhwa, 2001, Crozaz et al., 2003). Terrestrial alteration effects are more prevalent in meteorites that have been recovered from hot desert environments, particularly because hot deserts have a greater abundance of liquid water than cold deserts. Clays, iron oxides, hydroxides, and terrestrial carbonates have been commonly found in filling mineral fractures in hot desert meteorites, causing elevated concentrations of elements, such as Ba and La (Crozaz and Wadhwa, 2001; Crozaz et al., 2003). I observe enrichments of Ba in poikilitic shergottites NWA 11043 and NWA 7755 samples that contain carbonate veins filling fractures (Table 2). In terrestrial alteration studies of hot-desert meteorites, Ba is found hosted in carbonate veins (Crozaz and Wadhwa, 2001). Similar Ba enrichments have been reported for poikilitic shergottites NWA 7397 and NWA 10169 (Howarth et al., 2014; Combs et al., 2018). In addition, enrichments of La and associated negative Ce anomalies, such as what is seen for NWA 11043 (Fig. 4), are also attributed to REE remobilization by hot-desert alteration (e.g., Floss and Crozaz, 1991; Harvey et al., 1993; Wadhwa et al., 1994; Crozaz and Wadhwa, 2001; Crozaz et al., 2003; Walton et al., 2012; Howarth et al., 2014; Combs et al., 2015).

4.2 Nature of poikilitic shergottite geochemical reservoirs

4.2.2 Rare Earth Element enrichment of poikilitic shergottites

Ratios of the REE are largely unaffected by moderate degrees of fractional crystallization, permitting bulk rock $(La/Yb)_{CI}$ ratios, and corresponding REE patterns, to be used as proxies for parental magmas (e.g., Wadhwa et al., 1994; McSween et al., 1996; Symes et al., 2008). Based on

(La/Yb)$_{CI}$ values, I determined that the newly recovered NWA 11043 and NWA 4468 are enriched poikilitic shergottites, while NWA 11065 and NWA 10961 are intermediate (Table 2 and Fig. 4). Previously, NWA 11043 was defined as an intermediate poikilitic shergottite (Meteoritical Bulletin Database). I find that Northwest Africa 11043 has the highest (La/Yb)$_{CI}$ of any analyzed poikilitic shergottite sample (Table 2 and Fig. 4). However, this pattern is likely a byproduct of terrestrial weathering, causing a slight increase in (La/Yb)$_{CI}$ (Floss and Crozaz, 1991; Harvey et al., 1993; Wadhwa et al., 1994; Crozaz and Wadhwa, 2001; Crozaz et al., 2003; Walton et al., 2012; Howarth et al., 2014; Combs et al., 2018). Nonetheless, NWA 11043 is still akin to enriched poikilitic shergottites.

4.2.3 Relationships between subsolidus equilibration temperature, magmatic fO_2, and LREE-enrichment

Howarth et al. (2014) proposed a polybaric formation model for enriched poikilitic shergottite NWA 7397, where two stages of crystallization, at different depths within the martian interior, are recorded in the bimodal textures of poikilitic shergottites. The poikilitic texture is interpreted to have crystallized at a depth equivalent to 10 kbar pressure, under higher subsolidus equilibration temperatures (1200 °C) and more reducing conditions (QFM -2.0), while the non-poikilitic texture crystallized in transit to the martian surface at lower temperatures (868 °C) and more oxidizing conditions (QFM -1.1 to -0.3) (Howarth et al., 2014). Similar early- and late-stage subsolidus temperatures and fO_2 values have been reported for enriched poikilitic shergottites NWA 7755 and NWA 10169 (Howarth et al., 2015; Combs et al., 2018). I recalculated poikilitic (early-stage) and non-poikilitic (late-stage) subsolidus equilibration temperatures and fO_2 estimates on a separate thin section of NWA 7755 than Howarth et al. (2015), finding good agreement with previous estimates (Table 7). Additionally, calculated subsolidus equilibration

temperatures and fO$_2$ for poikilitic and non-poikilitic textures of enriched poikilitic shergottites RBT 04261/2, NWA 11043, NWA 10618, and NWA 4468 (Table 7 and Fig. 9) are in the range of other enriched poikilitic shergottite estimates (QFM -0.3 to QFM -2.5) (e.g., Usui et al., 2010; Jiang and Hsu et al., 2012; Lin et al., 2013; Howarth et al., 2014; 2015; Combs et al., 2018). Subsolidus equilibration temperatures and fO$_2$ found for the analyzed enriched poikilitic shergottites show evolution from hotter, more reduced magmatic conditions to cooler, more oxidized conditions, as crystallization proceeded, consistent with the formation models proposed for NWA 7397, NWA 7755, and NWA 10169 (Table 7 and Fig. 9) (e.g., Howarth et al., 2014; 2015; Combs et al., 2018).

Intermediate poikilitic shergottites have similar bimodal textures as enriched poikilitic shergottites (Figs. 1a and 1b). Expectedly, two-stage crystallization, and evolution of subsolidus equilibration temperatures and fO$_2$, have also been reported to be recorded in the two textures of intermediate poikilitic shergottites, with fO$_2$ values ranging from QFM -1.2 to QFM -3.2 (e.g., NWA 4797; Walton et al., 2012). My subsolidus equilibration temperatures and fO$_2$ values for intermediate NWA 10961, NWA 11065, ALHA 77005, and LEW 88516 agree with two-stage crystallization of intermediate poikilitic shergottites and support the notion that the two textural regions of poikilitic shergottites record evolving magmatic conditions at different crystallization stages (Table 7 and Fig. 9) (e.g., Howarth et al., 2014; 2015; Combs et al., 2018).

Oxygen fugacity values obtained for early-crystallizing mineral assemblages likely represent shergottite magmatic source redox conditions (e.g., Wadhwa et al., 2001; Herd et al., 2002; Herd et al., 2006). Previous studies have suggested that there is a correlation with the degree of LREE-enrichment and magmatic source redox conditions, where the incompatible-element depleted source region is reduced, and the enriched source is more oxidized (e.g., Wadhwa, 2001;

Herd et al., 2002; Herd, 2003; Hui et al., 2011). My fO$_2$ results suggest decoupling of fO$_2$ with (La/Yb)$_{CI}$ for shergottite geochemical reservoirs. For example, early-stage fO$_2$ of enriched poikilitic shergottite NWA 4468 is within uncertainties of early-stage fO$_2$ of intermediate NWA 4797, with values of QFM -2.9 (Table 7 and Fig. 9) (e.g., Walton et al., 2012). Additionally, early-stage fO$_2$ of intermediate poikilitic shergottites overlap with estimates previously found for depleted basaltic and olivine-phyric shergottites, such as QUE 94201, Tissint, and SaU 005 (Fig. 9) (e.g., Balta et al., 2015; Castle and Herd, 2018). A lack of correlation between (La/Yb)$_{CI}$ and fO$_2$ is also shown by other shergottites, such as poikilitic shergottites NWA 4797 and NWA 10169, gabbroic shergottite NWA 7320, and basaltic shergottite NWA 8657 (e.g., Walton et al., 2012; Castle and Herd, 2017; Udry et al., 2017; Howarth et al., 2018; Combs et al., 2018).

Poikilitic shergottites of this study show an increase in fO$_2$ from the poikilitic texture (early-stage crystallization) to the non-poikilitic texture (late-stage crystallization), with increases ranging from 1.2 to 2.0 log units below the QFM buffer for enriched poikilitic shergottites, and 2.0 to 2.9 log units for intermediate poikilitic (Table 7 and Fig. 9) (e.g., Walton et al., 2012; Howarth et al., 2014; 2015; Combs et al., 2018). The increase of fO$_2$ during crystallization and ascent can be explained by different factors. Throughout crystallization, Fe^{3+} becomes enriched in the melt and is incorporated into late-stage phases, such as spinel, causing higher fO$_2$ values to be found for late-stage melts. This process is known as auto-oxidation, and past modeling has shown that auto-oxidation can account for an increase in fO$_2$ of ~1 log unit (Peslier et al., 2010; Castle and Herd, 2017). Increases in fO$_2$ greater than ~1 log unit cannot be ascribed to solely auto-oxidation, necessitating external contributions, such as magmatic degassing, and/or assimilation of oxidized crust (e.g., Balta et al., 2013; Shearer et al., 2013; Castle and Herd, 2017).

It was previously thought that enriched shergottite magmas had unique capabilities of changing redox states throughout crystallization (e.g., Shearer et al., 2013). This was supported by the enriched olivine-phyric shergottites (e.g., NWA 1068/1110/1183 and LAR 06319) that showed substantial changes in fO$_2$ during crystallization, and limited fO$_2$ variations seen for depleted olivine-phyric shergottites (e.g., Yamato [Y] 98 and NWA 5789) (e.g., Herd, 2003; 2006; Shearer et al., 2006; Peslier et al., 2010; Gross et al., 2011; Shearer et al., 2013). However, as more investigations are conducted on other geochemical types of shergottites, crystallization over wide ranges of fO$_2$ is seen amongst intermediate and depleted shergottites as well (e.g., Gross et al., 2013; Castle and Herd, 2017; Howarth and Udry, 2017; this study). Commonality of fO$_2$ changes >1 log unit amongst shergottites has led to the idea that late-stage degassing is common with shergottite parental magmas, supporting fluids being present in the martian interior (e.g., Peslier et al., 2010;;Walton et al., 2012; Howarth et al., 2014; 2015; McCubbin et al., 2016; Castle and Herd, 2017; Howarth and Udry, 2017; Howarth et al., 2018; Combs et al., 2018).

4.3 Olivine crystallization

4.3.1 Kinetic parameters of olivine crystallization

I have used the combination of CSD analyses and phosphorus mapping to better understand kinetic parameters, such as nucleation density, cooling rates, and growth rates of the olivine populations within enriched and intermediate poikilitic shergottites. The nucleation density of a crystal population is related to the y-intercept of a CSD slope, with greater y-intercepts indicating higher nucleation densities (Higgins, 2011). The y-intercepts of the non-poikilitic olivine population CSD plots are all greater than the poikilitic populations, meaning population densities increased from the early stages of crystallization to the later stages (Fig. 12; Tables 9 and 10).

Lower nucleation densities for the poikilitic populations may be due to resorption of olivine chadacrysts, as also seen by their subhedral to anhedral shapes, rather than an increase in nucleation of olivine during crystallization of poikilitic textures. Additionally, all of the CSD plots display downturns at the smallest grain size intervals, representing either annealing or cessation of nucleation with continued olivine growth (Figs. 10 and 12) (e.g., Marsh, 1988; Higgins, 2011).

Investigation of olivine cooling rates was conducted using CSD slopes, relative magma residence times, and olivine grain sizes (Tables 8–10). Enriched poikilitic shergottites RBT 04261/2 show similar olivine population slopes, as well as the steepest slopes, smallest average olivine grain sizes, and shortest relative magma residence times, implying the olivine populations within them cooled the fastest (Tables 8 and 10; Figs. 10, 11a, 11b, and 12b). Northwest Africa NWA 11043, and NWA 7397 have similar slopes, olivine average grain sizes, and magma residence times, meaning they experienced similar cooling histories (Tables 8 and 10; Figs. 10, 11a, 11b, and 12b). Northwest Africa 7755 and NWA 4468 cooled slower than the previously mentioned samples. Olivine populations of NWA 10618 and NWA 10169, cooled the slowest, displaying shallowest slopes, longest magma residence times, and largest olivine average grain sizes (Tables 8 and 10; Figs. 10, 11a, 11b, and 12b). Fastest to slowest cooling of olivine within intermediate poikilitic shergottites is as follows: NWA 11065, ALHA 77005, and LEW 88516 (Tables 8 and 10; Figs. 10, 11a, 11b, and 12b).

Phosphorus-zoning in olivine has proven to be a useful tool in determining crystal-growth-rate variations (e.g., Boesenberg et al., 2004; Milman-Barris et al., 2008; Watson and Müller, 2009; Peslier et al., 2010; Ennis and McSween, 2014; Welsch et al., 2014 Baziotis et al., 2017). Phosphorus (P) acts as an incompatible element in olivine due to its low partition coefficient (K_d <0.1; Anderson and Greenland, 1969; Brunet and Chazot, 2001). However, studies have shown

that during periods of rapid disequilibrium growth of olivine, P acts as a compatible element, with P enrichments at the growing crystal interface (e.g., Spandler et al., 2007; Milman-Barris et al., 2008; Welsch et al., 2014). This is possible when the growth rate of olivine equals or exceeds the diffusion rate of P in the melt (Peslier et al., 2008). Additionally, early diffusion-controlled olivine growth at high degrees of supersaturation has been proposed to produce a dendritic P-enriched skeleton of olivine, which is then infilled by P-poorer material during subsequent slower growth (e.g., Welsch et al., 2013; 2014; 2016; Baziotis et al., 2017). The period of slower growth aids in producing the euhedral olivine crystal shape. Thus, if fluctuations in olivine growth controls and/or rates occur, then P-rich and P-poor zones within olivine will manifest (e.g., Milman-Barris et al., 2008; Welsch et al., 2014). These various P patterns within olivine can be preserved despite long magma residence times at high temperatures due to the extremely slow diffusion of P (e.g., Harrison and Watson, 1984; Spandler et al., 2007; Milman-Barris et al., 2008; Watson et al., 2015).

Phosphorus maps of poikilitic grains within enriched NWA 7755 and intermediate ALHA 77005 contain wide P-poor centers, surrounded by oscillations of P-rich and P-poor (Figs. 14b and 14c), supporting slow, steady equilibrium growth during initial olivine crystallization, followed by alternation of fast and slow growth rates. These growth histories are the most similar to that of poikilitic olivine of NWA 10618 within this study, although, the dendritic P-rich band of NWA 10618 signifies a period of fast, diffusion-controlled growth (Fig. 14a) (e.g., Welsch et al., 2014; Shea et al., 2015). The non-poikilitic grains of NWA 7755, ALHA 77005, and NWA 10618 display more complex P patterns than poikilitic grains (Fig. 14f – Fig. 14h), suggesting crystallization histories dominated by disequilibrium growth, potentially during ascent. I do not see these exact growth trends for olivine grains within LEW 88516 and NWA 11065. The P patterns of poikilitic olivine grains of LEW 88516 (Fig. 14d) are similar to P patterns within olivine phenocrysts of

Hawaiian postshield magmas, produced by dual mechanism growth, involving rapid, initial diffusion-controlled growth of olivine and a transition to interface-controlled growth (Welsch et al., 2014; 2016) (Fig. 14d). Poikilitic olivine grain of NWA 11065 also contains a P-rich center and displays oscillations of P-poor and P-rich bands, indicating oscillating crystal growth rate, albeit still dissimilar to that of LEW 88516. Different processes may be responsible for initial stages of poikilitic olivine growth within NWA 11065 and LEW 88516, or it may be an artifact due to the crystallographic plane that was cut during thin-section production. However, the P patterns of poikilitic olivine grain of NWA 11065 resemble that of intermediate olivine-phyric shergottite NWA 6234, which also shows a similar thin P-rich region (Gross et al., 2013). The P-rich core of NWA 6243 has been interpreted to be the result of undercooling, subsequent nucleation, and a period of rapid growth (Gross et al., 2013). Additionally, non-poikilitic olivine grains of LEW 88516 and NWA 11065 (Figs. 14i and 14j) suggest growth histories that were controlled by slower steady-equilibrium growth than growth histories of non-poikilitic olivine of NWA 7755, ALHA 77005, and NWA 10618 (Figs. 14f – 14h).

Although differences are seen between P-maps of poikilitic and non-poikilitic olivine within each sample, as well as differences between P-maps of each rock, there is a significant commonality amongst them; phosphorus zonation patterns of all measured olivine grains suggest that growth rates during both enriched and intermediate poikilitic and non-poikilitic olivine crystallization are not constant. Thus, magma residence times calculated for olivine populations by use of CSD are over generalized and can only be used for relative internal comparisons.

4.3.2 Physical processes affecting olivine crystallization

The CSD theory assumes that a steady-state, open magmatic system with continuous crystal nucleation and growth will produce a linear relationship between the population density

and crystal size (Cashman and Marsh, 1988; Marsh 1988; Marsh 1998; Higgins, 2011). Any curvature from the anticipated linear CSD pattern implies physical processes have affected the crystallizing population (Cashman and Marsh, 1988; Marsh 1988; Marsh 1998). An upward curvature of a CSD pattern (i.e., slope flattening at the largest grain sizes) is indicative of olivine accumulation, implying samples with a greater degree of slope flattening have experienced more olivine accumulation. All of the overall poikilitic shergottite olivine CSD plots show a slope flattening at the largest grain size interval, except for NWA 11043 (Fig. 10). Thus, NWA 11043 may have had less olivine accumulation compared to the other samples.

Additionally, the observed negative correlation between corrected CSD slope and CSD intercept (Fig. 11a) implies that textural coarsening was an active process during olivine crystallization (Higgins, 2011). However, this interpretation can only apply to samples that were emplaced in common cumulate piles or shallow sills (See section 4.4.3), as similar relationships have been observed in CSD studies of terrestrial igneous gabbro suites that crystallized within the same magmatic body (e.g., Higgins, 2011; Marsh 1998). Thus, any textural coarsening of enriched poikilitic shergottites would have occurred independently from textural coarsening of intermediate poikilitic shergottites, as the two groups are not co-magmatic.

The SDP of olivine populations within enriched and intermediate poikilitic shergottites corresponds to the spatial associations and arrangements of olivine crystals (e.g., Jerram et al., 2003). Nearly all of the analyzed samples fall within the "clustered touching framework" field, albeit closely bordering the "ordered non-touching framework" field (Fig. 13), suggesting olivine populations within these samples were generally produced by agglomeration of individual grains, which were moderately sorted (Jerram et al., 2003). The SDP analyses of NWA 11065 and NWA 7755 suggest the olivine populations did not form from agglomeration (Fig. 13). These two

samples contain the largest pyroxene oikocrysts (~10 mm) (Figs. 6a and 6b), whose growth, and entrapment of olivine grains likely impeded the occurrence of olivine grain clustering.

4.4 Origin, crystallization, and emplacement of enriched and intermediate poikilitic shergottites

4.4.1 Poikilitic shergottite source constraints

Disparate $(La/Yb)_{CI}$ ratios and REE patterns between enriched and intermediate poikilitic shergottites supports derivation from at least two unique magmatic sources (Fig. 4), which is also corroborated by distinct isotopic compositions (e.g., $^{87}Sr/^{86}Sr$ and $\varepsilon^{143}Nd$) between the two geochemical groups (e.g., Symes et al., 2008; Lapen et al., 2009; Usui et al., 2010; Shearer et al., 2013; Howarth et al., 2014; 2016; Combs et al., 2018). However, the locations of these possible magma reservoirs within the martian interior are not fully constrained. For instance, the location of the enriched source is still highly debated, with either location within the mantle and/or crust, whereas the intermediate signature is thought to either be a product of mixing between enriched and depleted reservoirs during melting, or it may represent an additional mantle source, potentially formed during magma ocean crystallization (e.g., Wadhwa at al., 1994; Borg et al., 2002; Barrat et al., 2002; Herd, 2003; Bridges and Warren, 2006; Symes et al., 2008; Basu Sarbadhikari et al., 2009; Usui et al., 2010; Basu Sarbadhikari et al., 2011; Borg et al., 2012; Brandon et al., 2012; Gross et al., 2013; Shearer et al., 2013; Balta et al., 2013; Howarth et al., 2014; Peters et al., 2015; Ferdous et al., 2017; Tait and Day, 2018). My fO_2 data have implications for the enriched component of poikilitic shergottites being derived from a distinct mantle reservoir, rather than derivation by assimilation of oxidized crustal material (e.g., Usui et al., 2010; Jiang Hsu, 2012; Howarth et al., 2014; 2018). The range of early-stage fO_2 values of the analyzed enriched poikilitic

shergottites is QFM -2.4 – -2.9 (Table 7 and Fig. 9) is more reduced than previous estimates obtained for other enriched poikilitic shergottites (e.g., QFM -1.5 – -2.0; Usui et al., 2010; Jiang and Hsu et al., 2012; Howarth et al., 2014; 2015). Thus, the enriched source shows greater variability in oxidation state, and formation conditions more similar to previous constraints made for shergottites that are believed to be mantle derived (e.g., depleted olivine-phyric shergottite Dar al Ghani — DaG — 476: QFM -2.56; Herd et al., 2001). Based on the reduced nature of the intermediate poikilitic shergottites (Table 7 and Fig. 9), which show close affinity in $f\mathrm{O}_2$ to depleted shergottites, the intermediate reservoir likely resides within the mantle as well (e.g., Usui et al., 2010; Jiang Hsu, 2012; Howarth et al., 2018).

Based on bulk rock REE compositions, I suggest that newly recovered NWA 4468 and NWA 11043 were derived from a LREE-enriched mantle source, similar to other enriched basaltic, olivine-phyric, and poikilitic shergottites (Fig. 4) (e.g., Anand et al., 2008; Lapen et al., 2009; Usui et al., 2010; Combs et al., 2018). In addition, my bulk rock REE data also imply that newly recovered NWA 10961 and NWA 11065 sampled mantle reservoirs that were moderately depleted in LREE (i.e., intermediate reservoir), with similar characteristics (e.g., [La/Yb]$_{CI}$ ratios and $f\mathrm{O}_2$ conditions) as source reservoirs of intermediate poikilitic shergottites ALHA 77005 and LEW 88615 (Fig. 4 and Fig. 9). However, in order to robustly link poikilitic shergottite samples to their source reservoir(s), isotopic compositions (e.g., $^{176}\mathrm{Hf}/^{177}\mathrm{Hf}$, $^{143}\mathrm{Nd}/^{144}\mathrm{Nd}$, and $^{87}\mathrm{Sr}/^{86}\mathrm{Sr}$) need to be measured.

4.4.2 Two-stage crystallization of poikilitic shergottites

Enriched and intermediate poikilitic shergottites have similar textures and mineral assemblages, with implications for a two-stage crystallization model for both types, as previously described for other poikilitic shergottites (e.g., Mikouchi, 2005; Mikouchi and Kurihara, 2008;

Howarth et al., 2014; 2015; Combs et al., 2018). Despite my lack of pressure condition constraints for the poikilitic shergottites of this study, I propose that polybaric formation models similar to that of Howarth et al. (2014) are appropriate here, based on textural relationships, mineralogical differences between the two domains, and dynamic subsolidus temperatures and fO_2 values (Tables 3, 4, 6, and 7; Figs. 1, 5, 9, and 9). Pyroxene oikocrysts enclosed chromite and olivine grains, within both enriched and intermediate poikilitic shergottites, and crystallized and accumulated early, as seen by higher Mg#s of poikilitic pyroxene and olivine than their non-poikilitic counterparts (Tables 3 and 4). Poikilitic olivine chadacrysts are typically subhedral to anhedral, with irregular grain boundaries (e.g., Figs. 14a, 14b, and 14c), consistent with instability of olivine in the parental melt, leading to resorption, and a peritectic reaction forming pyroxene (i.e., olivine + melt = pyroxene) (Bard et al., 1986). This reaction has also been suggested to have occurred in other poikilitic shergottites (e.g., RBT 04262; Usui et al., 2010, NWA 7397; Howarth et al., 2014, and NWA 10169; Combs et al., 2018).

More evolved interstitial melts, which would later crystallize to form non-poikilitic textures, subsequently entrained cumulus pyroxene oikocrysts, as well as cumulus olivine and chromite grains that were not enclosed by pyroxene. Evolved interstitial melts co-crystallized intergrowths of non-poikilitic pyroxene and maskelynite during transport to the martian surface. Late-stage phosphate, spinel, ilmenite, and sulfide phases crystallized as part of non-poikilitic textures, following non-poikilitic pyroxene and interstitial maskelynite crystallization. Lower Mg#s of non-poikilitic olivine and pyroxene, as well as higher TiO_2 concentrations of non-poikilitic spinel help justify more evolved melts being required to form non-poikilitic mineral assemblages (Tables 3, 4, and 6 and Figs. 5 and 6).

Although similar crystallization sequences are apparent for both geochemical types, the liquidus phases are different between the two, with spinel as the liquidus phase for enriched poikilitic shergottites and olivine for intermediate. Enriched poikilitic shergottites typically contain poikilitic olivine with spinel inclusions, whereas intermediate poikilitic shergottites do not. These mineral association observations are coupled with differing poikilitic fO$_2$ values between enriched and intermediate types. Magmatic fO$_2$ of poikilitic textures of intermediate poikilitic shergottites suggests reduced magmatic environments, which may have inhibited spinel growth, allowing olivine to crystallize first (e.g., Castle and Herd, 2018). A difference in crystallization sequences for enriched and intermediate poikilitic shergottite assemblages is also seen in the literature, where chromite has been interpreted to crystallize after olivine in intermediate poikilitic shergottites (e.g., Mikouchi, 2005; Mikouchi and Kurihara, 2008; Walton et al., 2012). Thus, the parental magma(s) that formed the intermediate poikilitic shergottites are similar to, but distinguishable from, that of the enriched poikilitic shergottites.

4.4.3 Poikilitic shergottites spatial relationships in the martian crust

Using quantitative textural analyses, in conjunction with bulk rock and mineralogical investigations of members of enriched and intermediate poikilitic shergottites, constraints on their possible petrogenesis are described here. As demonstrated above, enriched and intermediate poikilitic shergottites were derived from distinguishable magmatic plumbing systems. Here I propose distinct enriched poikilitic shergottite emplacement location(s) in the martian crust from that of members of the intermediate type (Fig. 15). To constrain the emplacement of enriched and intermediate poikilitic shergottites, of this study, in the martian crust, I use CSD data of non-poikilitic olivine populations of enriched and intermediate poikilitic shergottites, except in the case where analyzed thin sections only contained less than 10 poikilitic grains (olivine populations of

RBT 04261, NWA 7397, and LEW 88516) (Tables 8 and 10; Figs. 11 and 12b), as non-poikilitic olivine populations are representative of emplacement histories. Most poikilitic olivine populations are too small for statistically significant CSD analyses or have been resorbed.

Enriched poikilitic shergottites: Multiple non-poikilitic CSD parameters for RBT 04261/2 and NWA 4468 are similar, including best-fit ratios, olivine average sizes, and CSD patterns (Tables 8 and 10; Figs. 11a and 12b), lending support to their emplacement in a common cumulate pile or shallow intrusive body (Fig. 15), which concurs with their parallel REE patterns (Fig. 4), near identical poikilitic and non-poikilitic olivine compositions (Usui et al., 2010; this study), and identical Lu/Hf source compositions that suggest an origin from a common magmatic system (Lapen et al., 2009). Additionally, based on similar crystallization ages, similar REE patterns, and near identical $^{176}Lu/^{177}Hf$ source compositions, NWA 10169 has been interpreted to come from the same source as RBT 04261/2 and NWA 4468 (Combs et al., 2018). This may mean NWA 10169 was emplaced with RBT 04261/2 and NWA 4468, though significantly differing best-fit ratios (Tables 8 and 10) are more in favor of a separate emplacement location for NWA 10169 (Fig. 15). If NWA 10169 was emplaced with RBT 04261/2 and NWA 4468, it would have been emplaced at a greater depth based on its olivine average size, CSD slope, and relative magma residence time (Tables 8 and 10; Figs. 11a and 11b). Thus, I would expect NWA 10169 to exhibit a higher degree of compositional equilibration and compaction than RBT 04261/2 and NWA 4468, which is not what I observe (Figs. 5 and 13; this study, Fig. 5; Combs et al., 2018). Although NWA 10169 may not have been emplaced with RBT 04261/2 and NWA 4468, they likely began crystallizing in the same staging chamber (Fig. 15), as seen by their near identical poikilitic olivine compositions and similar early-stage fO$_2$ values (Table 7 and Fig. 9) (Usui et al., 2010; Combs et al., 2018; this study).

Enriched poikilitic shergottites NWA 7755 and NWA 10618 likely began crystallization in the same magmatic system as NWA 10169, NWA 4468, and RBT 04261/2 (Fig. 15), based on mineral, magmatic fO_2, and bulk rock REE compositional similarities (e.g., Figs. 4, 5, 9, and 14a-14d). Quantitative textural analyses of NWA 7755 and NWA 10618 also suggest potential emplacement with RBT 04261/2 and NWA 4468 (Tables 8 and 9; Figs. 10, 11a, 11b, and 12b). Northwest Africa 7755 and NWA 10618 have identical best-fit ratios that are similar to that of NWA 4468 and RBT 04261/2 (Tables 8 and 10), as well as nearly-parallel CSD patterns (Figs. 10 and 12b). NWA 10618 has larger olivine average sizes, greater relative magma residence times, and shallower slopes than RBT 04261/2, NWA 7755, and NWA 4468 (See section 4.3.1) (Tables 8 and 10; Figs. 10, 11a, 11b, and 12b), implying possible deeper emplacement in the same sill (Fig. 15). However, based on SDP data, it is possible that NWA 7755 was emplaced in an additional sill, separate from the other enriched poikilitic shergottites, as it is the only poikilitic shergottite to plot entirely within the "non-touching framework" field (Fig. 13). If NWA 7755 I consider to have emplaced with RBT 04261/2, NWA 4468, and NWA 10618, then NWA 10618 would be the deepest of the four samples, which is also supported by its smallest compositional range of olivine, suggesting highest equilibration degree (Fig. 5; this study, Fig. 6; Howarth et al., 2014; Howarth et al., 2015). Northwest Africa 10618 also shows greatest degree of olivine compaction (Fig. 13), further supporting greatest emplacement depth (Fig. 15). The emplacement depth sequence, with shallowest to deepest emplacement, would be: RBT 04261/2, NWA 7755, NWA 4468, and NWA 10618 (Tables 8 and 10; Figs. 10, 11a, 11b, and 12b).

Enriched NWA 7397 has a CRE age (~4.5 Ma; Wieler et al., 2016) that is similar to that of intermediate poikilitic shergottites, implying an emplacement location on Mars associated with intermediate poikilitic shergottites, rather than with enriched endmembers (Fig. 13). With all of

the previous observations considered, in addition to CSD data (i.e., distinct CSD profile morphology [Figs. 10 and 12b] and differing best-fit-ratio [Tables 8 and 10]) and mineralogical data (i.e., distinguishable total olivine population modal abundance; Table 1) for NWA 11043, I suggest either an additional emplacement location for NWA 11043 or emplacement with NWA 7397. Although NWA 11043 shows some dissimilarities to NWA 7397, the two have concordant CSD slopes, CSD intercepts, olivine average sizes, and relative magma residence times (Tables 8 and 10; Figs. 10, 11, and 12b). Thus, I am proposing that RBT 04261/2, NWA 4468, and NWA 10618 were emplaced in the same cumulate pile/sill/hypabyssal igneous body, which possibly also included NWA 7755, and either two or three other igneous bodies included NWA 10169, NWA 11043, and NWA 7397 (Fig. 15).

Intermediate poikilitic shergottites: Previously, stratigraphic relationships between intermediate poikilitic shergottites in a common igneous block have been proposed (e.g., Warren and Kallemeyn, 1997; Wadhwa et al., 1999; Mikouchi, 2005; Mikouchi and Kiruhara, 2008, Walton et al., 2012), using modal abundances and chemical compositions of cumulus and intercumulus phases, suggesting differences in these constraints resulted from spatial variation in cooling rates. Mikouchi (2005) suggested a shallower emplacement depth for LEW 88516 compared to ALHA 77005, based on a greater degree of compositional variation of olivine within LEW 88516 due to a lower degree of subsolidus re-equilibration. However, using CSD results, I observe that LEW 88516 shows a longer relative magma residence time and larger average olivine grain size than ALHA 77005 (i.e., LEW 88516 would have been emplaced deeper than ALHA 77005) (Tables 8 and 9; Figs. 10, 11a, 11b, and 12b). In addition, Goodrich et al. (2003) and Walton et al. (2012) suggested that LEW 88516 experienced higher degrees of subsolidus re-equilibration than ALHA 88516, based on spinel compositions and fO_2 data, contrary to the lower

degree proposed by Mikouchi (2005). Combining CSD results with distinct mineralogical data and isotopic data of ALHA 77005 and LEW 88516 (e.g., distinct olivine P-maps; Fig. 14e – 14h and distinct ϵ_{Nd} values; ALHA 77005: +11.1 and LEW 88516: +8.2; Borg et al., 2002), facilitates the interpretation that the two rocks did not crystallize in the same shallow sill or cumulate pile (e.g., Borg et al., 2002) (Fig. 15). They likely crystallized concurrently in the same volcanic complex on Mars, with intermediate poikilitic shergottites, such as Grove Mountain (GRV) 99027 and Y-793605, as seen by their similar Sm-Nd crystallization ages (~179 – ~185 Ma) (e.g., Nyquist et al., 2001; Misawa et al., 2006; Shih et al., 2011) and CRE ages (~4.0 – 5.0 Ma) (e.g., Nyquist et al., 2001; Kong et al., 2007) (Fig. 15).

Based on the near-identical REE patterns of NWA 11065 and NWA 10961 (Fig. 4), they likely originated from a common source that was moderately depleted in the LREE, which may also be the source of ALHA 77005 (Fig. 4). However, to produce Fe-rich pyroxene and olivine of NWA 11065 (Fig. 5), a significant amount of fractional crystallization of Mg-rich pyroxene and olivine would be required. Thus, NWA 11065 may have been derived from the same source region as NWA 10961 and ALHA 77005, but from a different, more evolved volcanic system (Fig. 15). Poikilitic olivine compositions of NWA 11065 are also distinct from intermediate poikilitic shergottites NWA 10961, ALHA 77005, and LEW 88516, supporting early crystallization in a distinct magmatic chamber (Fig. 15). Dissimilar P patterns of olivine within NWA 11065, ALHA 77005, and LEW 88615 further support crystallization in separate magmatic systems (Figs 14e, 14f, 14i, and 14j). Furthermore, NWA 11065 displays a distinct CSD profile from intermediate poikilitic shergottites ALHA 77005 and LEW 88516 (Figs. 10 and 12b), demonstrating emplacement separately from both ALHA 77005 and LEW 88516 (Fig. 15). Quantitative textural analyses were not conducted for NWA 10961; thus, I cannot use CSD or SDP information to

constrain its emplacement relative to other intermediate poikilitic shergottites. However, based on bulk rock trace element data (Table 2 and Fig. 4) and mineral compositions alone, there is possibility that NWA 10961 was emplaced with ALHA 77005 (Fig. 15). Therefore, I am proposing that three different igneous bodies were required for the emplacement of intermediate poikilitic shergottites of this study.

Although enriched and intermediate poikilitic shergottites are petrographically similar, many lines of evidence suggest their emplacement in various cumulate piles or shallow sills. Emplacement of enriched and intermediate poikilitic shergottites in different locations on Mars is also supported by the variation in ejection ages seen for them. Differing CRE ages but overlapping crystallization ages could mean that a widespread emplacement mechanism was occurring concurrently on Mars, resulting in the formation of poikilitic shergottites, thus widespread formation of an important lithology of the martian crust.

4.5 Petrogenetic links with other shergottites

Crystallization modeling of shergottites has shown that mineralogy and major element compositions can be greatly affected by fractional crystallization processes (e.g., Wadhwa et al., 1994; McSween et al., 1996; Symes et al., 2008). Contrarily, such modeling has shown that incompatible trace element systematics, thus radiogenic isotope systematics, are less susceptible to modifications during moderate degrees of fractional crystallization, allowing these systems to be used to establish magmatic source constraints (e.g., Wadhwa et al., 1994; McSween et al., 1996; Symes et al., 2008). Petrogenetic links amongst shergottites meteorites have been postulated with these controls considered (e.g., Nyquist et al., 2001; Borg et al., 2002; 2003; Brandon et al., 2004; Symes et al., 2008; Shearer et al., 2008; Lapen et al., 2009; Shafer et al., 2010; Brandon et al.,

2012; Borg et al., 2012; Filiberto et al., 2012; Shearer et al., 2013; Brennecka et al., 2014; Howarth et al., 2014; Balta et al., 2015; Howarth et al., 2015; Howarth and Udry, 2017; Lapen et al., 2017; Udry et al., 2017; Howarth et al., 2018; Combs et al., 2018; Tait and Day, 2018). Many authors have suggested at least two magmatic reservoirs for the formation of each geochemical class (thus at least six shergottite magmatic reservoirs), based on crystallization age groupings, modeled source isotopic compositions, and CRE ages, within each individual shergottite geochemical group (e.g., Borg et al., 2002; 2003; Symes et al., 2008; Lapen et al., 2009; Brennecka et al., 2014; Balta et al., 2015; Combs et al., 2018).

Based on distinct model $^{176}Lu/^{177}Hf$ source compositions, two geochemically enriched sources have been proposed to be responsible for the generation of young (~150 Ma − 225 Ma) enriched shergottites (e.g., Lapen et al., 2009; Combs et al., 2018; Udry et al., 2017). Enriched poikilitic shergottites NWA 10169, NWA 4468, and RBT 04261/2, enriched basaltic shergottites Shergotty and Zagami, and enriched olivine-phyric shergottite LAR 06319, are likely derived from one enriched source (hereafter, referred to as Enriched Source I), while enriched basaltic shergottites Los Angeles and NWA 856, and enriched gabbroic shergottite NWA 7320 are thought to be derived from a second enriched source (i.e., Enriched Source II; Fig. 15) (e.g., Nyquist et al., 2001; Brandon et al., 2004; Borg et al., 2008; Debaille et al., 2008; Lapen et al., 2009; Shafer et al., 2010; Lapen et al., 2010; Udry et al., 2017; Combs et al., 2018). Although I did not determine isotopic compositions for enriched poikilitic shergottites NWA 10618, NWA 11043, NWA 7755, and NWA 7397, their mineral compositions, fO_2 values, and bulk rock REE patterns (except for NWA 10618, which has not yet been measured for bulk rock compositions) are consistent with a petrogenetic affinity with samples derived from Enriched Source I (Fig. 15).

Young (~170 Ma – 212 Ma) intermediate shergottites are thought to originate from two spatially associated (based on ejection ages) mantle sources (Intermediate Source I and Intermediate Source II of Fig. 15) (e.g., Borg et al., 2002; Misawa et al., 2006; Ping et al., 2007; Misawa et al., 2008; Liu et al., 2011; Shih et al., 2011; Wieler et al., 2016). For example, intermediate poikilitic shergottites ALHA 77005, Y000027/000047/000097, and GRV 99027 have similar ε^{143}Nd values of +11.1, +11.7, and +12.2, respectively (Borg et al., 2002; Misawa et al., 2008; Liu et al., 2011), indicative of origination from the same source region (Intermediate Source I; Fig. 15). Intermediate poikilitic shergottites LEW 88516 and Y-793605 have slightly lower ε^{143}Nd values (+8.2 and +9.7, respectively), suggesting a similar, but distinct, source from previously mentioned intermediate poikilitic shergottites (Intermediate Source II; Fig. 15) (e.g., Borg et al., 2002; Misawa et al., 2006)

Additionally, newly recovered intermediate poikilitic shergottites NWA 11065 and NWA 10961, showing parallel bulk rock REE patterns to intermediate poikilitic shergottites (e.g., ALHA 77005 and GRV 99027) (Fig. 4), exhibit geochemical affinities to intermediate basaltic (e.g., NWA 480; Barrat et al., 2002b) and olivine-phyric (e.g., NWA 6234; Filiberto et al., 2012; Gross et al., 2013) shergottites (e.g., Fig. 4). Thus, an origin from a common intermediate source is possible (Intermediate Source I; Fig. 15). Phosphorus maps of olivine within NWA 11065 are distinct from that of ALHA 77005 (Figs. 14e, 14f, 14h, and 14i; this study), but are very similar to P patterns of olivine megacrysts within intermediate olivine-phyric NWA 6234 (Fig. 4; Gross et al., 2013), suggesting possible crystallization of NWA 11065 and NWA 6234 from the same magmatic plumbing system (Fig. 15).

Previous isotopic and mineralogical studies have demonstrated that different petrographic shergottite subtypes can form from fractionation within the same magmatic system (e.g., Filiberto

et al., 2012; Combs et al., 2018). Basaltic and olivine-phyric shergottites studies exemplify this, where basaltic shergottites are interpreted to be produced from parental melts similar to olivine-phyric shergottites, by either loss of olivine due to fractionation or lack of olivine entrainment (e.g., Shearer et al., 2008; Basu Sarbadhikari et al., 2009; 2011; Filiberto et al., 2012). The same concept could potentially be applied to link poikilitic shergottites to olivine-phyric shergottites, where entrainment and ascent of magma producing olivine-phyric shergottites occurs prior to formation and accumulation of poikilitic pyroxene oikocrysts. Thus, textural and mineralogical differences between basaltic, olivine-phyric, and poikilitic shergottites may arise due to magma tapping (from their respective geochemical reservoirs) occurring at different evolutionary stages. However, further fractional crystallization modeling and investigations of enriched and intermediate poikilitic shergottite crystallization ages, CRE ages, and isotopic compositions need to be conducted to better clarify their links with basaltic and olivine-phyric shergottites.

5. Summary

I have conducted the most comprehensive study on the formation and petrogenetic links amongst enriched and intermediate poikilitic shergottites yet. Through textural and geochemical investigations of members of enriched and intermediate poikilitic shergottites, new constraints on their possible petrogenesis and emplacement are revealed:

- Members of enriched and intermediate poikilitic shergottites have similar emplacement mechanisms and crystallization histories, and thus might have been prevalent on Mars during the Late Amazonian.

- Previous shergottite meteorite studies have shown that incompatible trace element systematics (e.g., $[La/Yb]_{CI}$ values) are not largely affected by fractional crystallization (e.g., Wadhwa et al., 1994; McSween et al., 1996). Thus, fractional crystallization processes affecting a common poikilitic shergottite parental magma could not have produced the distinguishable LREE-enrichments between enriched and intermediate poikilitic shergottites, as such crystallization from at least two distinguishable parental magmas, by partial melting of at least two distinct mantle reservoirs, is more likely.

- A late-stage oxidation event is common amongst enriched and intermediate poikilitic shergottites, as well as other shergottite subgroups, resulting from auto-oxidation and possible degassing. As more investigations of magmatic fO$_2$ of early-stage mineral assemblages of shergottites are conducted, stronger evidence for decoupling of relative LREE-enrichment (i.e., $[La/Yb]_{CI}$) and magmatic source fO$_2$ is found.

- Using quantitative textural analyses, I show that enriched and intermediate poikilitic shergottites were not emplaced in a common sill but rather were emplaced in various sills/shallow intrusive igneous bodies, in the martian crust, potentially at different geographic

locations on Mars, as seen by varying CRE ages for poikilitic shergottites (e.g., Nyquist et al., 2001; Eugster et al., 2010; Wieler et al., 2016) (Fig. 15).

- Based on bulk rock REE patterns, phosphorus maps, and previous isotopic studies, petrographic subtypes (basaltic, poikilitic, olivine-phyric, and gabbroic) of shergottites show clear petrogenetic affinities amongst their respective enriched and intermediate geochemical classes, however to confirm these relationships further isotopic analyses and fractional crystallization modeling need to be conducted.

Appendix A: Tables

Table 1. Mineral modal abundances (vol. %) of poikilitic shergottites

Enrichment	Sample	Olivine	Low-Ca pyroxene	High-Ca pyroxene	Maskelynite	Phosphates	Spinel	Ilmenite + sulfides	Glass	Shock melt
Enriched	NWA 4468	36	37	15	10	0.9	1.0	0.2	n.a.	n.a.
	NWA 10618	48	20	17	13	0.7	1.7	0.4	n.a.	n.a.
	NWA 11043	63	13	15	7.5	1.0	0.8	0.1	n.a.	n.a.
	NWA 7755	30	44	17	7.8	0.5	0.1	0.1	n.a.	n.a.
	NWA 7755[a]	48	25	10	14	0.5	trace	trace	n.a.	n.a.
	RBT 04261	44	21	9.1	23	1.7	1.4	0.1	1.6	n.a.
	RBT 04261[b]	42	22	10	20	1.8	1.6	0.5	n.a.	n.a.
	RBT 04262	33	38	17	8.5	1.3	0.7	0.6	n.a.	n.a.
	RBT 04262[b]	39	28	12	16	1.1	1.5	0.5	1.1	n.a.
	NWA 7397	51	22	12	13	1.7	1.2	0.2	n.a.	n.a.
	NWA 7397[c]	50	30	10	8.0	<1	-	-	-	-
	NWA 10169[d]	37	34	12	15	trace	2.0	trace	-	-
Intermediate	NWA 11065	33	30	16	17	2.1	1.5	0.2	n.a.	n.a.
	NWA 10961	49	21	11	3.6	1.5	0.8	0.1	n.a.	14
	ALHA 77005	53	23	8.4	8.3	0.7	0.5	trace	n.a.	6.4
	ALHA 77005[e]	60	13		9.5	0.4		4.0		14
	LEW 88516	52	21	9.1	10	1.3	1.2	0.3	n.a.	4.4
	LEW 88516[e]	46	37		7.0	0.9		1.6		7.7

[a]Howarth et al. (2015).
[b]Usui et al. (2010).
[c]Howarth et al. (2014).
[d]Combs et al. (2017).
[e]Treiman et al. (1994).
n.a. = not analyzed
- = data not available
trace = < 0.1 vol. %

Table 2. Measured trace (ppm) elemental compositions of enriched and intermediate poikilitic shergottites.

	Intermediate				Enriched				
ppm	NWA 11065	NWA 10961	ALHA 77005[a]	LEW 88516[a]	NWA 7755	NWA 11043	NWA 10169[b]	NWA 4468	RBT 04262[c]
Li	2.46	1.79	1.50	-	3.96	10.7	3.86	3.79	-
B	5.68	1.77	-	-	3.91	8.39	0.87	3.60	-
Sc	35.0	22.4	21.0	25.0	31.0	28.0	29.3	27.2	31.0
V	205	154	162	170	204	199	187	191	218
Co	64.5	65.8	72.0	65.0	71.1	74.6	62.5	71.2	63.0
Ni	250	307	290	280	330	326	270	317	291
Cu	29.8	5.74	5.10	-	10.3	842	8.20	10.5	6.60
Zn	60.8	53.5	60.0	60.0	71.1	56.2	76.5	77.7	74.0
Ga	13.5	6.44	7.30	9.20	8.90	7.03	10.4	12.9	8.20
Ge	1.56	1.22	0.58	0.60	1.54	1.50	2.15	2.40	-
Rb	1.54	0.68	0.70	1.10	3.38	2.15	3.77	4.46	4.00
Sr	30.8	31.0	14.0	17.0	39.9	51.6	41.9	44.2	22.2
Y	13.4	7.29	6.20	5.70	11.6	10.7	10.6	14.4	9.30
Zr	37.3	20.8	19.5	13.0	41.2	27.3	34.6	48.7	23.0
Nb	1.23	0.62	0.65	0.51	2.71	0.98	2.62	3.55	-
Mo	-	-	0.20	-	-	-	0.87	0.11	0.40
Sn	-	-	-	-	-	-	0.34	0.48	-
Cs	0.07	0.03	0.05	0.06	0.22	0.15	0.25	0.26	0.29
Ba	46.9	27.0	4.20	4.90	153	682	298	39.4	12.8
La	0.69	0.41	0.34	0.33	1.58	2.15	1.75	2.20	1.15
Ce	1.74	1.03	0.91	1.26	3.86	2.71	3.86	5.08	2.81
Pr	0.27	0.16	0.13	-	0.55	0.54	0.55	0.73	0.41
Nd	1.62	0.93	0.95	0.82	2.76	2.56	2.66	3.59	2.07
Sm	0.95	0.54	0.49	0.44	1.04	0.96	0.99	1.32	0.81
Eu	0.45	0.24	0.22	0.22	0.39	0.49	0.45	0.52	0.31
Gd	1.68	0.93	0.92	-	1.57	1.48	1.48	1.96	1.36
Tb	0.35	0.19	0.17	0.16	0.30	0.29	0.28	0.38	0.26
Dy	2.37	1.33	1.08	1.08	2.04	1.94	1.96	2.61	1.75
Ho	0.49	0.28	0.25	0.23	0.43	0.39	0.40	0.54	0.40
Er	1.30	0.74	0.66	-	1.19	1.05	1.13	1.53	1.07
Tm	0.19	0.11	0.09	0.10	0.17	0.15	0.16	0.21	0.16
Yb	1.13	0.65	0.59	0.57	1.09	0.92	1.01	1.35	0.96
Lu	0.16	0.09	0.08	0.08	0.16	0.13	0.14	0.19	0.15
Hf	1.26	0.74	0.62	0.52	1.23	0.96	1.13	1.57	0.97
Ta	0.09	0.04	0.03	0.04	0.15	0.06	0.14	0.18	-
W	0.17	0.07	0.08	0.14	0.26	0.15	0.26	0.32	380
Pb	0.26	0.06	-	-	0.51	6.29	0.65	0.53	-
Th	0.16	0.08	0.06	0.04	0.33	0.25	0.27	0.40	0.25
U	0.03	0.03	0.02	0.01	0.08	0.10	0.07	0.09	0.06
Eu/Eu*	1.09	1.04	1.00	-	0.93	1.26	1.14	0.98	0.91
$(La/Yb)_{CI}$	0.41	0.43	0.39	0.39	0.98	1.59	1.18	1.11	0.81

[a]Lodders, 1998, [b]Combs et al., 2018, [c]Anand et al., 2008, [d]Tait and Day, 2018.

- = not measured.

Table 3. Olivine compositions of intermediate (NWA 11065, NWA 10961) and enriched (NWA 11043, NWA 4468, and NWA 10618) poikilitic shergottites.

	NWA 11065						NWA 10961						ALHA 77005						LEW 88516					
	Poikilitic				Non-poikilitic		Poikilitic				Non-poikilitic		Poikilitic				Non-poikilitic		Poikilitic				Non-poikilitic	
	High Fo	Low Fo	Avg	SD	Avg	SD	High Fo	Low Fo	Avg	SD	Avg	SD	High Fo	Low Fo	Avg	SD	Avg	SD	High Fo	Low Fo	Avg	SD	Avg	SD
n			23		29				30		56				101		53				37		30	
wt%																								
SiO_2	36.7	35.4	35.7	0.34	35.3	0.40	38.4	37.3	37.8	0.34	37.4	0.28	39.0	37.1	38.0	0.43	37.5	0.21	37.8	36.9	37.5	0.45	36.7	0.31
TiO_2	0.03	b.d.	0.03	0.02	0.03	0.03	0.02	0.06	0.02	0.02	0.03	0.03	b.d.	0.02	b.d.	-	0.02	0.01	b.d.	0.02	0.02	0.02	0.06	0.09
Al_2O_3	0.02	0.02	0.03	0.03	0.02	0.04	b.d.	b.d.	0.13	0.26	0.04	0.08	b.d.	b.d.	b.d.	0.02	b.d.	-	0.07	b.d.	0.04	0.11	0.04	0.09
Cr_2O_3	0.04	0.03	0.04	0.04	0.03	0.04	0.08	b.d.	0.06	0.07	0.05	0.05	0.04	0.05	0.05	0.06	0.06	0.05	0.05	0.02	0.08	0.15	0.04	0.04
FeO	28.9	35.4	32.5	1.81	35.4	1.68	21.2	26.8	23.9	1.68	26.7	0.64	21.0	26.1	23.2	1.30	25.4	0.69	22.8	29.1	24.8	2.12	30.0	0.83
MnO	0.66	0.80	0.69	0.05	0.77	0.05	0.48	0.60	0.53	0.04	0.59	0.04	0.46	0.57	0.50	0.03	0.55	0.02	0.48	0.57	0.54	0.05	0.63	0.04
MgO	34.6	27.0	30.4	1.59	28.2	1.30	39.2	34.8	36.6	1.42	34.4	0.53	40.2	35.8	38.3	1.11	36.5	0.59	38.2	33.4	36.6	1.59	31.6	0.85
CaO	0.15	0.25	0.19	0.04	0.21	0.04	0.13	0.20	0.18	0.04	0.19	0.04	0.13	0.15	0.16	0.03	0.17	0.04	0.07	0.16	0.18	0.08	0.24	0.16
P_2O_5	0.04	0.05	0.05	0.05	0.07	0.09	0.05	0.04	0.04	0.03	0.05	0.07	0.04	0.05	0.05	0.06	0.05	0.05	0.06	b.d.	0.06	0.05	0.08	0.10
NiO	0.06	0.03	0.05	0.02	0.03	0.02	0.08	0.08	0.06	0.03	0.04	0.03	0.07	0.04	0.05	0.02	0.04	0.02	0.06	0.05	0.05	0.02	0.05	0.02
Total	101	99.0	99.7	0.75	100	0.52	99.6	99.9	99.4	0.47	99.4	0.44	101	100	100	0.44	100	0.42	99.6	100	100	0.52	100	0.47
Fo	68.1	57.6	62.5	2.47	58.7	2.23	76.7	69.8	73.2	2.10	69.7	0.79	77.4	71.0	74.6	1.61	71.9	0.84	74.9	67.2	72.5	2.58	65.3	1.12

	NWA 11043						NWA 4468						NWA 10618					
	Poikilitic				Non-poikilitic		Poikilitic				Non-poikilitic		Poikilitic				Non-poikilitic	
	High Fo	Low Fo	Avg	SD	Avg	SD	High Fo	Low Fo	Avg	SD	Avg	SD	High Fo	Low Fo	Avg	SD	Avg	SD
n			16		23				49		84				17		53	
wt%																		
SiO_2	36.3	36.9	36.7	0.35	36.2	0.24	37.2	36.0	36.8	0.46	36.2	0.33	36.4	35.9	35.9	0.25	35.8	0.35
TiO_2	0.02	0.04	0.02	0.01	0.03	0.02	0.02	0.02	0.02	0.02	0.03	0.02	b.d.	0.05	0.03	0.02	0.03	0.02
Al_2O_3	0.19	0.86	0.14	0.22	0.12	0.21	0.05	b.d.	0.03	0.02	0.02	0.02	0.13	n.d.	0.03	0.04	0.05	0.14
Cr_2O_3	0.05	0.06	0.07	0.04	0.06	0.05	0.06	b.d.	0.03	0.08	b.d.	-	0.04	0.07	0.03	0.02	0.04	0.04
FeO	26.8	30.4	28.7	0.87	30.9	0.50	27.0	35.1	30.4	2.25	34.1	0.79	29.8	32.7	31.7	0.80	33.0	0.84
MnO	0.64	0.71	0.65	0.03	0.69	0.03	0.57	0.72	0.64	0.05	0.71	0.03	0.63	0.68	0.67	0.02	0.69	0.02
MgO	34.2	31.0	33.8	1.07	31.9	0.60	34.3	27.9	31.8	1.95	28.8	0.74	32.0	30.2	30.8	0.50	29.8	0.62
CaO	0.24	0.27	0.23	0.04	0.21	0.06	0.17	0.13	0.19	0.05	0.19	0.04	0.19	0.12	0.17	0.04	0.18	0.05
P_2O_5	0.03	0.18	0.07	0.08	0.10	0.12	n.a.	n.a.	n.a.	-	n.a.	-	0.02	b.d.	0.05	0.03	0.09	0.12
NiO	0.07	0.03	0.06	0.02	0.05	0.02	b.d.	n.a.	0.03	0.03	0.03	0.02	0.09	0.05	0.06	0.03	0.05	0.02
Total	98.6	100	101	0.80	100	0.52	99.5	99.9	99.9	0.55	100	0.45	99.3	99.8	99.5	0.55	99.7	0.61
Fo	69.5	64.5	62.5	2.47	64.8	0.61	69.4	58.6	65.1	3.07	60.0	1.14	65.7	62.2	63.4	0.90	61.7	1.01

Avg = average composition; SD = standard deviation.

n = number of analyses.

n.a. = not analyzed.

b.d. = below detection limit.

Table 4. Average pyroxene compositions of intermediate (NWA 11065, NWA 10961) and enriched (NWA 11043, NWA 4468, and NWA 10618) poikilitic shergottites.

	NWA 11065								NWA 10961								ALHA 77005							
	Low-Ca pyroxene				High-Ca pyroxene				Low-Ca pyroxene				High-Ca pyroxene				Low-Ca pyroxene				High-Ca pyroxene			
	P	SD	NP	SD	P	SD	NP	SD	P	SD	NP	SD	P	SD	NP	SD	P	SD	NP	SD	P	SD	NP	SD
n	30		18		15		9		24		32		20		18		40		15		8		16	
wt%																								
SiO_2	53.2	0.72	51.9	0.73	51.9	0.77	51.8	0.43	54.7	0.77	54.3	0.48	53.0	0.41	52.5	0.57	55.0	0.63	53.9	0.63	52.4	0.61	52.1	0.73
TiO_2	0.17	0.06	0.48	0.19	0.36	0.14	0.41	0.11	0.16	0.15	0.31	0.16	0.31	0.08	0.38	0.10	0.11	0.09	0.36	0.23	0.37	0.16	0.44	0.17
Al_2O_3	0.75	0.16	1.07	0.28	1.69	0.56	1.83	0.32	0.87	0.52	0.94	0.24	1.62	0.44	1.99	0.40	0.49	0.19	0.94	0.25	1.68	0.64	1.88	0.54
Cr_2O_3	0.44	0.09	0.33	0.12	0.74	0.11	0.78	0.15	0.47	0.09	0.44	0.12	0.80	0.06	0.84	0.07	0.47	0.08	0.43	0.11	0.87	0.06	0.88	0.09
FeO	17.6	1.34	20.0	1.65	12.3	0.72	12.8	1.38	14.0	0.81	15.2	1.26	9.48	0.51	10.1	0.62	14.1	0.41	15.5	0.90	8.95	0.56	9.21	0.59
MnO	0.64	0.07	0.71	0.10	0.46	0.07	0.50	0.06	0.49	0.05	0.54	0.05	0.41	0.10	0.41	0.05	0.49	0.04	0.57	0.04	0.37	0.03	0.39	0.03
MgO	23.1	1.67	19.0	1.08	16.7	0.84	16.6	0.92	25.6	1.83	23.6	0.70	18.1	0.74	18.1	0.83	27.4	1.49	24.0	1.07	17.7	0.74	17.5	0.66
CaO	4.03	1.39	6.46	1.62	15.1	1.31	15.0	1.93	3.79	1.93	5.10	1.25	15.8	1.17	15.2	1.12	2.58	1.24	4.87	0.88	17.5	0.87	17.4	1.05
Na_2O	0.07	0.03	0.10	0.04	0.16	0.04	0.20	0.03	0.05	0.03	0.07	0.02	0.16	0.03	0.18	0.03	0.04	0.03	0.09	0.04	0.21	0.02	0.21	0.03
Total	100	0.46	100	0.53	99.6	0.43	99.9	0.39	100	0.58	100	0.52	99.7	0.39	99.7	0.30	101	0.52	101	0.42	100	0.64	100	0.43
Total	8.09	2.86	13.3	3.36	31.5	2.89	31.2	4.15	7.56	3.93	10.2	2.53	32.7	2.44	31.6	2.54	5.01	2.49	9.66	1.80	35.6	1.99	35.5	2.12
En	64.4	3.94	54.4	2.94	48.5	2.06	48.0	2.32	70.7	4.33	65.8	1.37	52.1	1.82	52.2	1.90	73.7	3.20	66.4	2.41	50.2	1.64	49.9	1.56
Fs	27.5	2.35	32.2	2.65	20.1	1.07	20.7	2.19	21.7	1.30	23.9	2.04	15.3	0.81	16.3	0.90	21.3	0.86	24.0	1.51	14.2	0.90	14.7	1.00

	NWA 11043								NWA 4468								NWA 10618							
	Low-Ca pyroxene				High-Ca pyroxene				Low-Ca pyroxene				High-Ca pyroxene				Low-Ca pyroxene				High-Ca pyroxene			
	P	SD	NP	SD	P	SD	NP	SD	P	SD	NP	SD	P	SD	NP	SD	P	SD	NP	SD	P	SD	NP	SD
n	23		22		4		20		62		17		25		5		19		36		3		7	
wt%																								
SiO_2	53.9	0.53	53.0	0.37	52.5	0.58	52.1	0.36	54.2	0.66	52.8	0.44	52.6	0.45	52.0	0.81	53.2	0.57	52.5	0.41	52.1	0.56	52.0	0.57
TiO_2	0.13	0.04	0.42	0.14	0.38	0.18	0.41	0.13	0.18	0.18	0.55	0.24	0.32	0.14	0.69	0.14	0.18	0.08	0.33	0.13	0.26	0.05	0.42	0.17
Al_2O_3	0.67	0.19	0.96	0.28	1.51	0.29	1.85	0.29	0.67	0.20	0.93	0.25	1.56	0.31	1.45	0.12	0.79	0.15	0.94	0.28	1.39	0.08	1.75	0.11
Cr_2O_3	0.48	0.09	0.38	0.09	0.76	0.13	0.75	0.13	0.38	0.06	0.32	0.11	0.73	0.07	0.55	0.07	0.43	0.10	0.35	0.12	0.70	-	0.75	0.07
FeO	16.1	0.40	18.3	0.98	11.3	0.69	11.9	1.20	16.4	0.06	18.7	0.90	11.0	0.55	12.8	0.84	16.8	0.73	18.5	1.28	11.4	0.71	11.3	1.25
MnO	0.63	0.03	0.72	0.04	0.50	0.04	0.52	0.05	0.58	0.04	0.68	0.04	0.46	0.03	0.48	0.04	0.59	0.03	0.64	0.04	0.44	0.03	0.45	0.04
MgO	24.9	0.89	22.1	0.68	17.7	1.00	17.7	0.74	23.7	1.45	20.3	0.61	16.6	0.65	16.0	0.43	23.5	0.92	21.3	0.58	17.6	0.27	17.3	0.59
CaO	3.62	1.09	4.82	0.89	15.7	1.58	14.7	1.77	3.49	1.20	5.51	1.20	16.4	1.01	15.5	0.99	4.16	0.97	5.07	1.03	15.4	0.59	15.5	1.66
Na_2O	0.05	0.02	0.09	0.02	0.18	0.04	0.21	0.03	0.07	0.02	0.11	0.03	0.21	0.03	0.25	0.04	0.07	0.02	0.10	0.03	0.21	0.02	0.23	0.04
Total	100	0.57	101	0.45	101	0.46	100	0.51	100	0.49	99.8	0.48	100	0.33	99.4	0.53	100	0.64	99.7	0.44	99.2	0.46	99.5	0.91
Wo	7.14	2.17	9.70	1.85	32.0	3.28	30.2	3.67	7.10	2.51	11.4	2.48	34.1	2.13	32.4	2.20	8.34	2.00	10.3	2.13	31.6	1.29	32.0	3.40
En	68.2	2.13	61.7	1.50	50.1	2.64	50.6	2.00	67.0	3.37	58.4	1.54	48.1	1.77	46.7	1.08	65.4	2.10	60.2	1.39	50.2	0.68	49.8	1.52
Fs	24.7	0.56	28.6	1.49	17.9	1.11	19.1	1.93	25.9	1.24	30.2	1.44	17.8	0.90	20.9	1.24	26.2	1.07	29.5	2.00	18.2	1.10	18.2	2.02

P = poikilitic texture; SD = standard deviation; NP = non-poikilitic texture.

n = number of analyses.

n.a. = not analyzed.

57

Table 5. Maskelynite compositions of intermediate (NWA 11065, NWA 10961) and enriched (NWA 11043, NWA 4468, and NWA 10618) poikilitic shergottites.

	NWA 11065				NWA 10961				NWA 11043				NWA 4468				NWA 10618			
	Low An	High An	Avg	SD	Low An	High An	Avg	SD	Low An	High An	Avg	SD	Low An	High An	Avg	SD	Low An	High An	Avg	SD
n			32				36				28				28				31	
wt%																				
SiO$_2$	53.7	53.9	53.8	0.89	55.8	53.7	54.3	0.50	55.9	54.0	54.0	0.62	58.9	53.8	55.8	1.71	57.3	53.4	54.3	0.74
TiO$_2$	0.04	0.04	0.05	0.02	0.15	0.06	0.08	0.03	0.10	0.05	0.08	0.03	0.15	0.07	0.07	0.03	0.10	0.04	0.06	0.02
Al$_2$O$_3$	29.3	28.8	29.0	0.54	27.2	29.1	28.4	0.42	28.0	29.3	29.1	0.38	25.9	28.8	27.9	1.05	26.9	29.2	28.4	0.45
FeO	0.47	0.72	0.49	0.08	0.32	0.34	0.34	0.07	0.37	0.60	0.52	0.10	0.45	0.48	0.46	0.11	0.41	0.46	0.47	0.06
MgO	0.14	0.16	0.11	0.03	0.09	0.13	0.14	0.03	0.11	0.09	0.13	0.03	0.06	0.09	0.07	0.02	0.06	0.10	0.10	0.02
CaO	12.0	11.9	11.5	0.67	9.54	11.6	10.9	0.41	10.5	11.7	11.6	0.32	7.82	11.6	10.2	1.27	9.00	11.5	10.9	0.54
Na$_2$O	4.75	4.39	4.83	0.33	5.92	5.05	5.20	0.20	5.36	4.27	4.75	0.25	6.41	4.72	5.37	0.61	6.00	4.62	4.97	0.29
K$_2$O	0.12	0.17	0.18	0.08	0.35	0.23	0.26	0.05	0.32	0.22	0.24	0.03	0.77	0.33	0.49	0.15	0.43	0.26	0.32	0.05
P$_2$O$_5$	0.02	0.04	0.04	0.02	0.07	0.03	0.05	0.02	0.05	0.02	0.06	0.06	n.a.	n.a.	n.a.	n.a.	0.05	0.02	0.03	0.02
Total	101	100	100	0.66	99.4	100	99.6	0.32	101	100	100	0.56	100	100	100	0.35	100	99.5	99.7	0.47
An	41.2	59.5	56.3	3.25	46.1	55.2	52.8	1.90	51.0	59.5	56.6	1.82	38.5	56.5	49.7	6.16	44.2	57.0	53.9	2.61

Avg = average composition; SD = standard deviation.

n = number of analyses.

n.a. = not analyzed.

Table 6. Spinel compositions of intermediate (NWA 11065, NWA 10961) and enriched (NWA 11043, NWA 4468, and NWA 10618) poikilitic shergottites.

	NWA 11065						NWA 10961						NWA 11043					
	P spinel		NP spinel				P spinel		NP spinel				P spinel		NP spinel			
	Avg	SD	Chr-rich Avg	SD	Ulv-rich Avg	SD	Avg	SD	Chr-rich Avg	SD	Ulv-rich Avg	SD	Avg	SD	Chr-rich Avg	SD	Ulv-rich Avg	SD
n	8		8		8		5		11		6		14		5		19	
wt%																		
SiO_2	0.16	0.04	0.08	0.06	0.04	0.02	0.22	0.11	0.16	0.02	0.08	0.02	0.16	0.19	0.16	0.06	0.15	0.18
TiO_2	0.93	0.17	13.7	1.00	17.2	1.24	1.00	0.14	1.20	0.36	11.2	1.08	1.47	0.49	2.68	1.47	12.9	3.01
Al_2O_3	4.78	0.71	4.28	0.70	3.56	1.04	6.82	0.70	6.40	0.69	6.11	0.35	6.06	1.36	6.31	0.84	4.92	1.06
Cr_2O_3	58.0	0.94	25.4	3.25	16.5	2.08	58.2	1.36	57.5	1.35	34.4	2.49	55.1	2.72	51.6	3.68	30.2	6.33
Fe_2O_3	3.80	0.91	12.7	1.79	15.9	2.47	0.89	0.46	1.40	0.26	6.25	0.88	4.38	1.29	5.21	1.78	8.55	1.82
FeO	27.1	1.23	40.5	0.84	43.7	1.01	25.4	0.73	27.1	0.85	36.1	1.24	27.0	1.35	29.0	1.65	39.0	2.77
MnO	0.68	0.03	0.71	0.07	0.75	0.04	0.56	0.04	0.66	0.03	0.73	0.05	0.66	0.03	0.68	0.03	0.77	0.04
MgO	4.29	0.63	2.73	0.19	2.48	0.28	5.76	0.25	4.42	0.52	4.10	0.29	4.91	0.75	4.41	0.68	3.46	0.24
CaO	0.02	0.01	0.04	0.04	0.02	0.01	0.03	0.01	0.03	0.02	0.03	0.01	0.07	0.04	0.08	0.10	0.03	0.02
Total	99.8	0.72	100	0.92	100	0.76	98.9	0.21	98.9	0.27	99.0	0.48	99.8	0.57	100	0.85	100	0.74
Chr	86.7	1.64	43.8	4.31	30.2	2.81	82.9	1.80	82.9	1.96	53.1	3.16	82.3	3.91	78.0	3.91	48.5	8.76
Sp	10.6	1.42	11.0	1.61	9.78	3.10	14.4	1.47	13.8	1.48	14.1	0.82	13.5	2.89	14.2	1.87	11.8	2.20
Ulv	2.64	0.48	45.2	4.53	60.0	3.76	2.70	0.39	3.30	0.99	32.9	3.52	4.18	1.44	7.76	4.33	39.7	10.2

	NWA 4468						NWA 10618					
	P spinel		NP spinel				P spinel		NP spinel			
	Avg	SD	Chr-rich Avg	SD	Ulv-rich Avg	SD	Avg	SD	Chr-rich Avg	SD	Ulv-rich Avg	SD
n	12		3		10		19		15		13	
wt%												
SiO_2	0.29	0.24	0.34	0.19	0.10	0.06	0.10	0.07	0.13	0.10	0.05	0.02
TiO_2	1.39	0.56	1.16	0.27	11.4	5.21	3.42	3.34	1.84	1.07	13.1	3.54
Al_2O_3	7.81	1.21	6.32	0.59	5.67	1.35	8.80	2.53	7.61	1.15	5.35	1.51
Cr_2O_3	54.2	2.41	55.0	1.56	31.8	11.1	47.0	9.23	51.5	3.85	26.1	7.13
Fe_2O_3	4.17	0.65	4.78	0.58	9.50	2.50	5.25	1.89	4.68	0.97	11.2	2.48
FeO	27.3	1.37	28.8	0.39	38.3	5.03	29.9	3.65	29.4	1.07	39.5	2.90
MnO	0.70	0.05	0.72	0.04	0.71	0.03	0.65	0.03	0.65	0.03	0.71	0.05
MgO	4.44	0.64	3.10	0.28	2.97	0.41	4.12	0.77	3.47	0.57	2.81	0.26
CaO	0.02	0.02	b.d.	-	b.d.	-	0.06	0.04	0.04	0.03	0.03	0.01
Total	100	0.44	100	0.66	100	0.47	99.2	0.62	99.3	0.43	98.9	0.40
Chr	79.1	3.49	82.6	1.50	50.7	15.6	70.4	12.9	77.6	5.26	43.9	10.1
Sp	17.0	2.59	14.1	1.44	13.6	2.68	19.7	5.33	17.1	2.66	13.4	3.25
Ulv	3.86	1.56	3.30	0.78	35.8	18.0	9.97	10.0	5.29	3.13	42.7	13.1

P = poikilitic, NP = non-poikilitic, Avg = average, SD = standard deviation.

Chr = chromite, Ulv = ulvospinel, Sp = spinel.

n = number of analyses.

b.d. = below detection limit.

Table 7. Oxygen fugacity (fO_2) and subsolidus equilibration temperature estimates for enriched and intermediate poikilitc shergottites.

Enrichment	Sample	Texture	No. of assemblages	Average T (°C)[a]	1 SD T (°C)	Average $\log_{10}fO_2$[a]	1 SD ($\log_{10}fO_2$)	Average $\log_{10}fO_2$ (IW[b])	1 SD (IW)	Average $\log_{10}fO_2$ (QFM[c])	1 SD (QFM)	Previous fO_2 estimates (QFM)[d-h]
Enriched	NWA 4468	Poikilitic	4	1036	98	-12.86	1.03	+0.70	0.53	-2.87	0.46	-
		Non-poikilitic	2	932	80	-14.14	1.03	+2.03	0.49	-1.72	0.39	
	NWA 10618	Poikilitic	4	1081	71	-12.74	1.25	+0.90	0.24	-2.68	0.29	-
		Non-poikilitic	4	854	17	-14.95	0.23	+2.74	0.27	-1.11	0.25	
	NWA 7755	Poikilitic	2	1032	1	-13.23	0.46	+1.13	0.45	-2.50	0.45	-2.0[d]
		Non-poikilitic	2	842	82	-15.16	1.42	+2.89	0.49	-0.99	0.36	-1.7 to -1.3[d]
	RBT 04261	Poikilitic	2	1080	131	-12.67	1.13	+0.94	0.47	-2.64	0.51	-
		Non-poikilitic	3	873	85	-14.48	1.68	+2.88	0.12	-0.95	0.14	
	RBT 04262	Poikilitic	3	1048	131	-13.18	1.82	+1.06	0.61	-2.56	0.51	-1.6[e]
		Non-poikilitic	3	800	46	-15.62	1.05	+3.33	0.12	-0.60	0.10	
	NWA 11043	Poikilitic	6	1101	72	-12.21	0.92	+1.13	0.41	-2.43	0.38	-
		Non-poikilitic	5	888	41	-14.38	0.85	+2.61	0.35	-1.20	0.35	
	NWA 7397[f]	Poikilitic	-	868[f]	-	-	-	-	-	-	-	-2.0 to -1.8[f]
		Non-poikilitic	-	-	-	-	-	-	-	-	-	-1.1 to -0.3[f]
	NWA 10169[g]	Poikilitic	-	994[g]	22[g]	-	-	-	-	-	-	-2.50±0.38[g]
		Non-poikilitic	-	803[g]	66[g]	-	-	-	-	-	-	-1.08±0.15[g]
Intermediate	ALHA 77005	Poikilitic	13	1089	74	-13.61	0.78	-0.09	0.41	-3.67	0.37	-3.7[h]
		Non-poikilitic	1	924	-	-14.18	-	+2.08	-	-1.68	-	
	LEW 88516	Poikilitic	6	1093	88	-13.77	1.01	-0.30	0.57	-3.87	0.51	-2.4[h]
		Non-poikilitic	3	947	5	-13.69	0.02	+2.14	0.06	-1.59	0.06	
	NWA 11065	Poikilitic	2	1119	37	-12.85	0.49	+0.20	0.05	-3.34	0.01	-
		Non-poikilitic	5	850	39	-14.40	0.66	+3.39	0.28	-0.47	0.24	
	NWA 10961	Poikilitic	4	1185	39	-12.79	0.65	-0.64	0.25	-4.12	0.27	-
		Non-poikilitic	3	904	21	-14.22	0.43	+2.43	0.03	-1.35	0.05	

[a]T and $\log_{10}fO^2$ calculated using the CT Server Ol-Px-Sp oxybarometer, which utilizes the Ghiorso and Sack (1991) Ol-Sp geothermometer.
[b]Relative to Iron-Wüstite (IW) buffer defined by Herd (2008) with the use of O'Neil and Pownceby (1993) data.
[c]Relative to Quartz-Fayalite-Magnetite (QFM) buffer defined by Wones and Gilbert (1969).
[d]NWA 7755 QFM data obtained by Howarth et al. (2015)
[e]RBT 04262 QFM data obtained by Usui et al. (2010).
[f]NWA 7397 QFM data obtained by Howarth et al. (2014).
[g]NWA 10169 QFM data obtained by Combs et al. (2018).
[h]ALHA 77005 and LEW 88516 QFM data obtained by Walton et al. (2012).

Table 8. Quantitative textural analyses of olivine grains in poikilitic shergottites

Enrichment	Sample	No. of grains	Total Area (mm^2)	R^2	Best-fit ratio	Shape	Alignment factor	Big R	Orientation	Average size (mm)	1 SD	Max	Min	Slope (mm^{-1})	Intercept
	NWA 4468	1100	201	0.91	1.00:1.20:1.60	Rectangular prism	0.24	1.039	Length	0.28	0.24	1.98	0.04	-4.96 ± 0.11	4.92 ± 0.06
									Width	0.18	0.15	1.19	0.03	-6.66 ± 0.07	5.74 ± 0.07
	NWA 10169	506	136	0.90	1.00: 1.25:1.90	Rectangular prism	0.46	1.087	Length	0.31	0.30	2.38	0.38	-3.55 ± 0.11	3.91 ± 0.08
									Width	0.19	0.18	1.94	0.03	-4.79 ± 0.17	4.69 ± 0.09
	NWA 7397	1664	237	0.91	1.00:1.15:1.60	Rectangular prism	0.12	1.131	Length	0.26	0.24	3.80	0.04	-4.63 ± 0.08	5.03 ± 0.04
									Width	0.17	0.15	2.39	0.03	-6.41 ± 0.13	5.86 ± 0.05
	NWA 10618	848	200	0.88	1.00:1.15:1.60	Rectangular prism	0.22	1.206	Length	0.34	0.31	2.10	0.66	-3.68 ± 0.08	4.10 ± 0.06
									Width	0.22	0.20	1.56	0.03	-4.91 ± 0.13	4.85 ± 0.07
Enriched	NWA 7755	571	182	0.91	1.00:1.15:1.60	Rectangular prism	0.20	1.092	Length	0.30	0.25	2.05	0.06	-4.37 ± 0.13	4.12 ±0.08
									Width	0.19	0.18	1.66	0.04	-5.69 ± 0.19	4.82 ± 0.09
	RBT 04261	767	80	0.89	1.00:1.20:1.70	Rectangular prism	0.26	1.123	Length	0.21	0.18	1.77	0.34	-6.22 ± 0.16	5.97 ± 0.07
									Width	0.14	0.12	0.92	0.03	-6.95 ± 0.21	6.36 ± 0.08
	RBT 04262	861	114	0.92	1.00:1.20:1.60	Rectangular prism	0.23	1.01	Length	0.21	0.20	2.24	0.04	-6.03 ± 0.15	5.62 ± 0.06
									Width	0.14	0.12	1.29	0.03	-7.73 ± 0.21	6.31 ± 0.07
	NWA 11043	1562	189	0.92	1.00:1.25:1.80	Rectangular prism	0.16	1.305	Length	0.28	0.20	1.42	0.04	-4.71 ± 0.10	5.19 ± 0.05
									Width	0.18	0.13	0.86	0.03	-5.58 ± 0.13	5.78 ± 0.06
	ALHA 77005	500	81	0.91	1.00:1.20:1.70	Rectangular prism	0.43	1.338	Length	0.33	0.2	1.26	0.06	-4.13 ± 0.16	4.72 ± 0.10
									Width	0.21	0.18	0.71	0.03	-5.36 ± 0.22	5.49 ± 0.11
Intermediate	LEW 88516	246	72	0.91	1.00:1.25:1.70	Rectangular prism	0.48	1.164	Length	0.40	0.33	2.47	0.07	-3.28 ± 0.15	3.64 ± 0.13
									Width	0.25	0.20	1.31	0.03	-4.06 ± 0.21	4.30 ± 0.14
	NWA 11065	1039	168	0.90	1.00:1.15:1.70	Rectangular prism	0.22	1.10	Length	0.25	0.18	1.52	0.04	-5.17 ± 0.13	5.12 ± 0.07
									Width	0.16	0.12	1.26	0.03	-6.75 ± 0.18	5.85 ± 0.07

*Used estimated growth rate (G) of ~3.1x10^{-8} mm/s (Basu Sarbadhikari et al., 2009).

Table 8 continued. Quantitative textural analyses of olivine grains in poikilitic shergottites

Enrichment	Sample	T (Earth days)* 10^{-8}	Slope (mm^{-1}) ($\geq$0.1 mm)	Total Intercept ($\geq$0.1 mm)	T (Earth days)* 10^{-8} ($\geq$0.1 mm)
Enriched	NWA 4468	75	-4.76 ± 0.10	4.80 ± 0.06	78
		56	-	-	-
	NWA 10169	105	-3.57 ± 0.11	3.93 ± 0.08	105
		78	-	-	-
	NWA 7397	81	-4.68 ± 0.09	5.06 ± 0.04	80
		58	-	-	-
	NWA 10618	101	-3.69 ± 0.08	4.11 ± 0.06	101
		76	-	-	-
	NWA 7755	85	-4.39 ± 0.13	4.13 ± 0.08	85
		66	-	-	-
	RBT 04261	60	-6.22 ± 0.16	5.97 ± 0.07	60
		54	-	-	-
	RBT 04262	62	-6.06 ± 0.15	5.63 ± 0.06	62
		49	-	-	-
	NWA 11043	79	-4.75 ± 0.10	5.23 ± 0.06	79
		67	-	-	-
Intermediate	ALHA 77005	90	-4.30 ± 0.16	4.86 ± 0.10	87
		70	-	-	-
	LEW 88516	114	-3.32 ± 016	3.68 ± 0.13	112
		92	-	-	-
	NWA 11065	72	-5.27 ± 0.13	5.18 ± 0.07	71
		55	-	-	-

*Used estimated growth rate (G) of ~3.1x10^{-8} mm/s (Basu Sarbadhikari et al., 2009).

Table 9. Quantitative textural analyses of poikilitic olivine grains.

Enrichment	Sample	No. of grains	Total Area (mm^2)	R^2	Best-fit ratio	Shape	Alignment factor	Big R	Orientation	Average size (mm)	1 SD	Max	Min	Slope (mm^{-1})
	NWA 4468	243	201	0.88	1.00:1.25:1.90	Rectangular prism	0.22	0.709	Length	0.26	0.23	1.77	0.04	-4.63 ± 0.22
	NWA 10169	141	136	0.88	1.00:1.40:2.20	Rectangular prism	0.43	0.836	Length	0.25	0.23	1.50	0.04	-4.53 ± 0.30
Enriched	NWA 7755	194	182	0.80	1.00:1.30:2.40	Rectangular prism	0.11	0.960	Length	0.30	0.24	1.30	0.05	-3.51 ± 0.17
	RBT 04262	148	114	0.73	1.00:1.15:1.40	Rectangular prism	0.24	0.726	Length	0.20	0.15	0.88	0.03	-8.06 ± 0.49
	NWA 11043	196	189	0.83	1.00:1.20:1.70	Rectangular prism	0.16	0.618	Length	0.35	0.17	0.97	0.04	-5.15 ± 0.36
	ALHA 77005	194	81	0.88	1.00:1.15:1.60	Rectangular prism	0.49	0.926	Length	0.29	0.20	1.26	0.06	-4.60 ± 0.29
Intermediate	NWA 11065	217	168	0.91	1.00:1.40:1.70	Rectangular prism	0.22	1.104	Length	0.24	0.18	1.52	0.07	-5.19 ± 0.13

*Used estimated growth rate (G) of ~3.1x10^{-8} mm/s (Basu Sarbadhikari et al., 2009).

Table 9 continued. Quantitative textural analyses of poikilitic olivine grains.

Enrichment	Sample	Intercept	T (Earth days)* 10^{-8}	Slope (mm^{-1}) ($\geq$0.1 mm)	Total Intercept ($\geq$0.1 mm)	T (Earth days)* 10^{-8} ($\geq$0.1 mm)
	NWA 4468	3.41 ± 0.13	81	-3.93 ± 0.22	2.87 ± 0.13	95
	NWA 10169	3.14 ± 0.16	82	-4.56 ± 0.31	3.16 ± 0.18	82
Enriched	NWA 7755	2.84 ± 0.13	106	-3.51 ± 0.17	2.84 ± 0.13	106
	RBT 04262	4.46 ± 0.17	46	-8.06 ± 0.49	4.46 ± 0.17	46
	NWA 11043	3.27 ± 0.18	73	-5.26 ± 0.38	3.33 ± 0.19	71
	ALHA 77005	3.95 ± 0.16	81	-4.74 ± 0.31	4.05 ± 0.18	79
Intermediate	NWA 11065	5.13 ± 0.07	72	-6.75 ± 0.37	4.08 ± 0.15	55

*Used estimated growth rate (G) of ~3.1x10^{-8} mm/s (Basu Sarbadhikari et al., 2009).

Table 10. Quantitative textural analyses of non-poikilitic olivine grains.

Enrichment	Sample	No. of grains	Total Area (mm^2)	R^2	Best-fit ratio	Shape	Alignment factor	Big R	Orientation	Average size (mm)	1 SD	Max	Min	Slope (mm^{-1})
Enriched	NWA 4468	857	201	0.91	1.00:1.30:1.50	Rectangular prism	0.25	0.867	Length	0.27	0.24	1.98	0.04	-5.58 ± 0.14
	NWA 10169	361	136	0.89	1.00:1.40:2.10	Rectangular prism	0.48	0.920	Length	0.34	0.34	2.38	0.04	-3.41 ± 0.13
	NWA 7755	378	182	0.91	1.00:1.15:1.60	Rectangular prism	0.24	0.767	Length	0.30	0.26	2.05	0.05	-4.23 ± 0.16
	RBT 04262	720	114	0.93	1.00:1.30:1.60	Rectangular prism	0.23	0.906	Length	0.21	0.21	2.24	0.04	-6.31 ± 0.17
	NWA 11043	1366	189	0.92	1.00:1.25:1.80	Rectangular prism	0.16	1.215	Length	0.26	0.20	1.42	0.04	-4.59 ± 0.10
Intermediate	ALHA 77005	321	81	0.86	1.00:1.25:1.70	Rectangular prism	0.37	1.148	Length	0.35	0.23	1.76	0.07	-4.15 ± 0.21
	NWA 11065	806	168	0.88	1.00:1.20:1.60	Rectangular prism	0.23	0.996	Length	0.26	0.18	1.51	0.06	-5.63 ± 0.16

*Used estimated growth rate (G) of ~3.1x10^{-8} mm/s (Basu Sarbadhikari et al., 2009).

Table 10 continued. Quantitative textural analyses of non-poikilitic olivine grains.

Enrichment	Sample	Intercept	T (Earth days)* 10^{-8}	Slope (mm^{-1}) (≥0.1 mm)	Total Intercept (≥0.1 mm)	T (Earth days)* 10^{-8} (≥0.1 mm)
	NWA 4468	4.85 ± 0.06	67	-4.19 ± 0.14	4.09 ± 0.06	89
	NWA 10169	3.50 ± 0.10	109	-3.42 ± 0.13	3.51 ± 0.10	109
Enriched	NWA 7755	3.63 ± 0.10	88	-4.26 ± 0.16	3.65 ± 0.10	88
	RBT 04262	5.52 ± 0.07	59	-6.32 ± 0.17	5.53 ± 0.07	59
	NWA 11043	5.01 ± 0.06	81	-4.64 ± 0.10	5.05 ± 0.06	81
Intermediate	ALHA 77005	4.29 ± 0.13	90	-4.24 ± 0.21	4.35 ± 0.13	88
	NWA 11065	4.99 ± 0.08	66	-5.63 ± 0.16	4.99 ± 0.08	66

*Used estimated growth rate (G) of ~3.1x10^{-8} mm/s (Basu Sarbadhikari et al., 2009).

Appendix B: Figure captions

Figure 1. Mg X-ray maps of a) enriched poikilitic shergottite NWA 4468,2 and b) intermediate poikilitic shergottite ALHA 77005, 207, representing the similar characteristic bimodal textures of enriched and intermediate poikilitic shergottites. Poikilitic textures (P) outlined in red and non-poikilitic textures (NP) in blue.

Figure 2. Composite X-ray map images (Ca = red, Fe = green, Mg = blue) of a) enriched poikilitic shergottite NWA 11043, b) enriched poikilitic shergottite RBT 04261, and c) intermediate poikilitic shergottite NWA 10961.

Figure 3. Backscatter electron (BSE) image of ~600 μm long pyrrhotite grain within NWA 10961,A bordering a shock melt boundary.

Figure 4. CI chondrite-normalized (McDonough and Sun, 1995) rare earth element (REE) profiles for enriched and intermediate poikilitic shergottites. Data for enriched poikilitic shergottite NWA 10169 from Combs et al. (2018); RBT 04262 from Anand et al. (2008); NWA 7397 from Howarth et al. (2014). Data for enriched basaltic shergottite Los Angeles from Jambon et al. (2002). Data for intermediate poikilitic shergottites ALHA 77005 from Smith et al. (1984); LEW 88516 from Lodders (1998); GRV 99027 from Lin et al. (2005). Data for intermediate basaltic shergottite NWA 480 from Barrat et al. (2002).

Figure 5. Pyroxene quadrilateral and olivine major element compositions for enriched (NWA 11043, NWA 10618, and NWA 4468) and intermediate (NWA 11065 and NWA 110961) poikilitic shergottites. Compositional fields for the intermediate poikilitic shergottites are from Mikouchi et al. (2005) and Mikouchi et al. (2008). Compositional fields for the enriched poikilitic shergottites are from Bingkui et al. (2004), Usui et al. (2010), and Howarth et al. (2014). Figure modified after Combs et al. (2018).

Figure 6. Ca X-ray maps of a) intermediate NWA 11065 and b) enriched NWA 7755, showing pyroxene phases within poikilitic (large [~10 mm] zoned pyroxene oikocrysts) and non-poikilitic (irregularly zoned non-poikilitic pyroxene grains) textures. Inset maps showing textural zones in detail. P = poikilitic texture; NP = non-poikilitic texture; lcp = low-Ca pyroxene; hcp = high-Ca pyroxene. White dashed lines delineate textural boundaries.

Figure 7. Maskelynite major element compositions in enriched poikilitic shergottites (NWA 10618, NWA 11043, NWA 4468) and intermediate poikilitic shergottites (NWA 11065 and NWA 110961) plotted on the An-Ab-Or ternary. Compositions predominantly overlap with those of the intermediate poikilitic shergottites, with NWA 4468 also overlapping with enriched poikilitic shergottites. Intermediate poikilitic shergottite fields from ALHA 77005, LEW 88516, Y793605, and NWA 1950 (Harvey et al., 1993; Mikouchi and Miyamoto, 1997; Mikouchi, 2005); enriched poikilitic shergottite fields from RBT 04261/2, GRV 020090, and NWA 7755 (Usui et al., 2010; Jiang and Hsu, 2012; Howarth et al., 2015).

Figure 8. Spinel Ulv-Chr-Spn ternary diagram for enriched poikilitic shergottites (NWA 10618, NWA 11043, NWA 4468) and intermediate poikilitic shergottites (NWA 11065 and NWA 110961) plotted on the. Intermediate poikilitic shergottite fields from NWA 4797 (Walton et al., 2012); enriched poikilitic shergottite fields from RBT 04261/2, GRV 020090, and NWA 7755 (Usui et al., 2010; Jiang and Hsu et al., 2012; Howarth et al., 2015).

Figure 9. Oxygen fugacities (fO_2) relative to the FMQ buffer versus relative REE enrichment (i.e., [La/Yb]$_{CI}$). Early-stage poikilitic fO_2 of intermediate poikilitic shergottites (NWA 10961, NWA 11065, ALHA 77005, and LEW 88516) overlap with previous fO_2 values of depleted shergottites (e.g., Herd, 2003; Balta et al., 2015; Castle and Herd, 2017). Depleted fields from Herd et al. (2001), Herd (2003), Balta et al. (2015), and Castle and Herd (2017). Intermediate

fields from Herd et al. (2002), Goodrich et al. (2003), Lin et al. (2005), Walton et al. (2012). Gross et al. (2013), Howarth and Udry (2017). Enriched fields from Peslier et al. (2010), Usui et al. (2010). Jiang and Hsu et al. (2012), Howarth et al. (2014), Combs et al. (2018). Modified after Combs et al. (2018).

Figure 10. Crystal size distribution profiles for a) olivine grains in enriched and intermediate poikilitic shergottites, b) intermediate poikilitic shergottites LEW 88516, ALHA 77005, and NWA 11065, and c) enriched poikilitic shergottites NWA 10169, NWA 10618, NWA 7755, NWA 7397, NWA 11043, NWA 4468, RBT 04261, and RBT 04262.

Figure 11. Crystal size distribution analyses for enriched and intermediate poikilitic shergottites; Non-poikilitic olivine crystal size distribution data is used for all poikilitic shergottites, except in the case of RBT 04261, NWA 7397, and LEW 8856, where total olivine population data is used, as their olivine populations had less than 10 poikilitic olivine grains. a) Crystal size distribution slope (>0.1 mm) versus intercept; b) Crystal size distribution slope (>0.1 mm) versus olivine average size (mm); c) Crystal size distribution slope (>0.1 mm) versus olivine modal abundance (vol. %); d) Crystal size distribution olivine average size (mm) versus olivine modal abundance (vol. %); e) Crystal size distribution reciprocal of residence time (years) versus CSD slope/CSD intercept ratio. Non-poikilitic olivine crystal size distribution data is used for all poikilitic shergottites, except in the case of RBT 04261, NWA 7397, and LEW 8856, where total olivine population data is used as their olivine populations had less than 10 poikilitic olivine grains.

Figure 12. Crystal size distribution analyses of a) Poikilitic olivine populations and b) Non-poikilitic olivine populations in enriched poikilitic shergottites (NWA 10169, NWA 7755, NWA 11043, NWA 4468, RBT 04262) and intermediate poikilitic shergottites (ALHA 77005 and NWA 11065).

Figure 13. Spatial distribution pattern analyses of olivine in enriched and intermediate poikilitic shergottites with porosity (% melt) versus R-value. RDSL = Random Sphere Distribution Line.

Figure 14. Phosphorus (P) X-ray maps of poikilitic and non-poikilitic olivine grains of enriched and intermediate poikilitic shergottites. Relative pixel intensities between maps are not significant, but brighter pixels within individual maps indicate higher P content. Features of interest are labeled "A", "B", "C", etc. a) Poikilitic olivine grains in enriched NWA 10618 with alternating P-poor and P-rich zonations [A] and a resorbed boundary. This olivine has a P-poor melt inclusion at its center that is surrounded by a P-rich rim [B]. There is also a P-rich dendritic band zonation surrounding an inner P-poor domain [C]. b) Poikilitic olivine grain in enriched NWA 7755. This grain has a wide subhedral P-poor center [A], with nearly continuous concentric bands of low- and high- P olivine (i.e., oscillatory P zoning) [B], and a resorbed grain boundary [C]. c) Composite poikilitic olivine grain in intermediate ALHA 77005 with P-poor centers [A], surrounded by nearly continuous oscillatory zoning [B]. d) Composite poikilitic olivine grain in intermediate LEW 88516 [A_1] and [A_2]. Crystal [A_1] has a euhedral P-rich center [B], surrounded by discontinuous oscillatory P-zoning [C]. Crystal [A_2] has a dendritic P-rich center [D] that is also surrounded by discontinuous oscillator P-zoning [C]. e) Poikilitic olivine grain in intermediate NWA 11065. The center of the grain contains a thin P-rich zonation [A]. The P-rich center is mantled by alternating P-poor and P-rich olivine [B]. f) Non-poikilitic olivine grain in enriched NWA 10618. A P-poor melt inclusion lies at the grain center [A]. Nearly continuous oscillatory P-zoning that nearly parallels crystal boundaries is present from outer core to crystal rim [B]. Discontinuity of oscillatory P-bands is present at the bottom right grain corner, where curved, wispy, alternating P-poor and P-rich bands occur [C]. g) Non-poikilitic olivine grain in enriched

NWA 7755, exhibiting core- to- rim oscillatory P-zoning [A]. h) Composite non-poikilitic olivine grain of intermediate ALHA 77005 [A]. Both component crystals display oscillatory P-zoning [B]. The lower right of the larger component contains a dendritic P-rich zonation [B]. i) Non-poikilitic olivine grain in intermediate LEW 88516 with a P-poor center [A] that is surrounded by oscillatory P-zoning that show offset faulting likely occurring during shock [B]. A shock melt pocket is visible, containing skeletal olivine grains surrounded by a P-rich matrix [C]. j) Composite non-poikilitic olivine grain in intermediate NWA 11065. Larger component crystal has a wide P-poor center [A], surrounded by few oscillatory P-bands [B]. Three smaller component crystals show P-rich centers and nearly continuous oscillatory P-zoning [C].

Figure 15. Schematic petrogenetic model for emplacement of enriched and intermediate poikilitic shergottites, and their relationships to other enriched and intermediate shergottites, which crystallized concurrently during the Late Amazonian (~150 Ma – ~225 Ma) (e.g., Shih et al., 1982; Nyquist et al., 2001; Borg et al., 2002; Shih et al., 2003; Brandon et al., 2004; Bouvier et al., 2005; Misawa et al., 2006; Borg et al., 2008; Debaille et al., 2008; Lapen et al., 2008; Misawa et al., 2008; Lapen et al., 2009; Shih et al., 2009; Marks et al., 2010; Shafer et al., 2010; Liu et al., 2011; Shih et al., 2011; Ferdous et al., 2017; Combs et al., 2018). The physical constraints of mantle sources are unclear. Sources may occur as localized pockets, layers, or broad regional reservoirs. Ejection events of enriched and intermediate shergottites from the martian atmosphere based on CRE ages (e.g., Nyquist et al., 2001; Eugster et al., 2010; Wieler et al., 2016). See main text for details.

Figure 1.

Figure 2.

a) NWA 11043 CaFeMg 2 mm

b) RBT 04261 CaFeMg 2 mm

c) NWA 10961 CaFeMg 2 mm
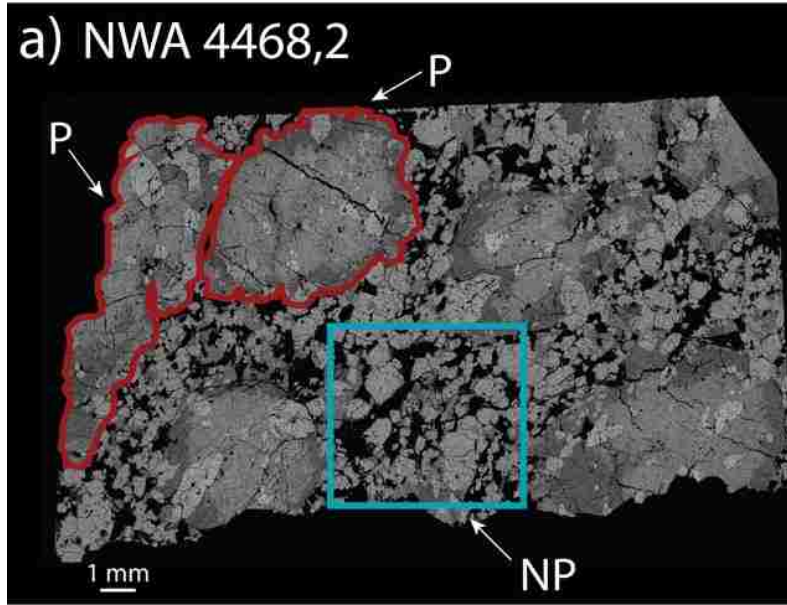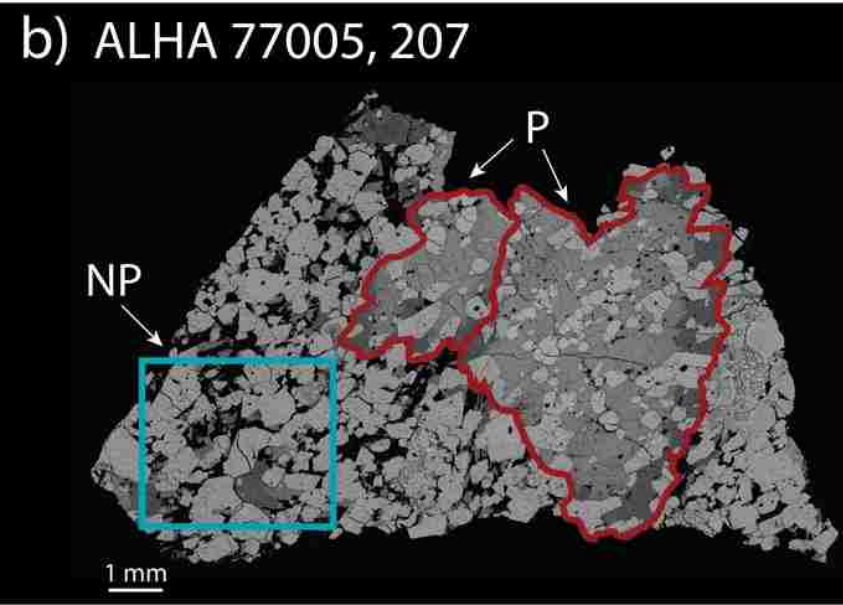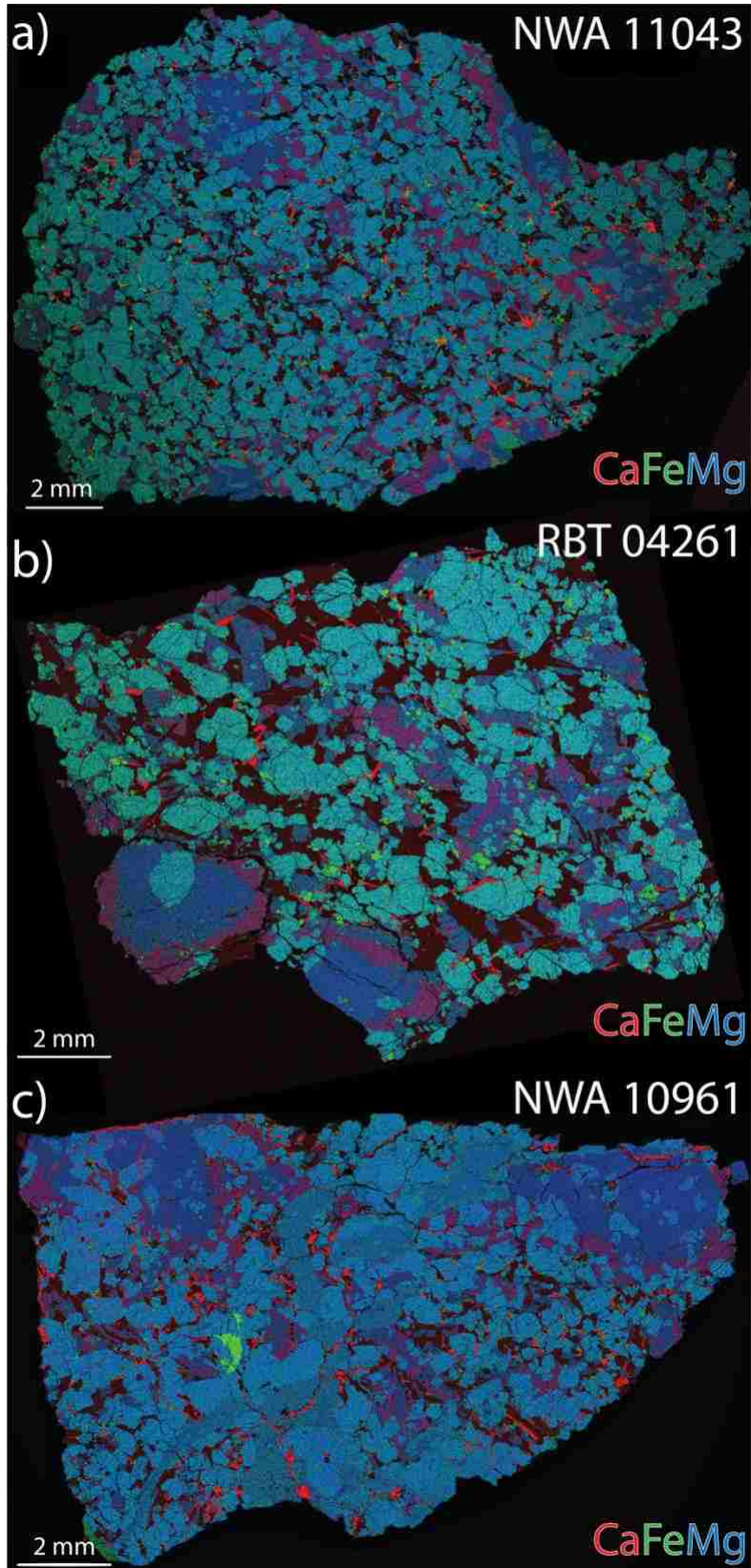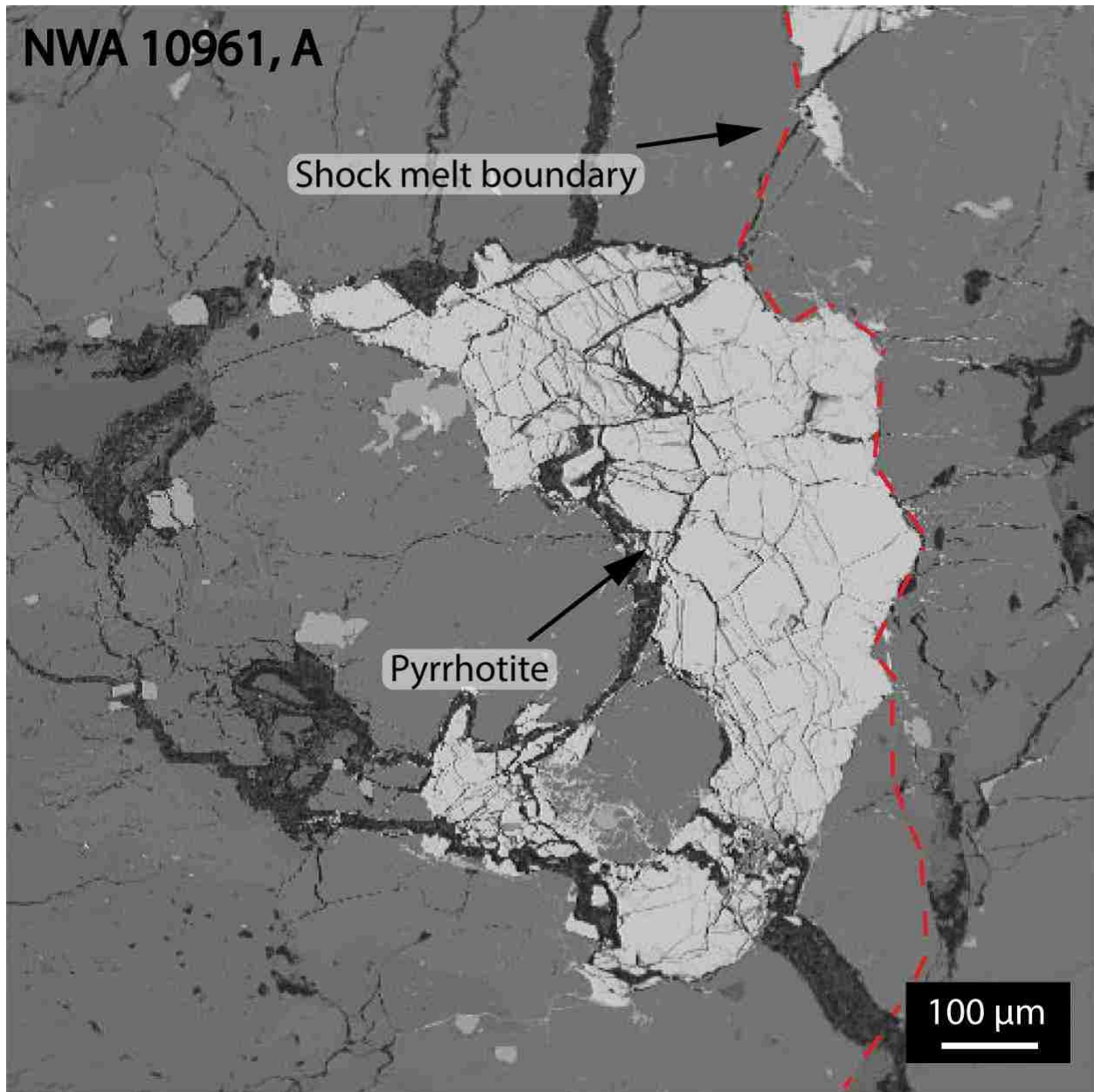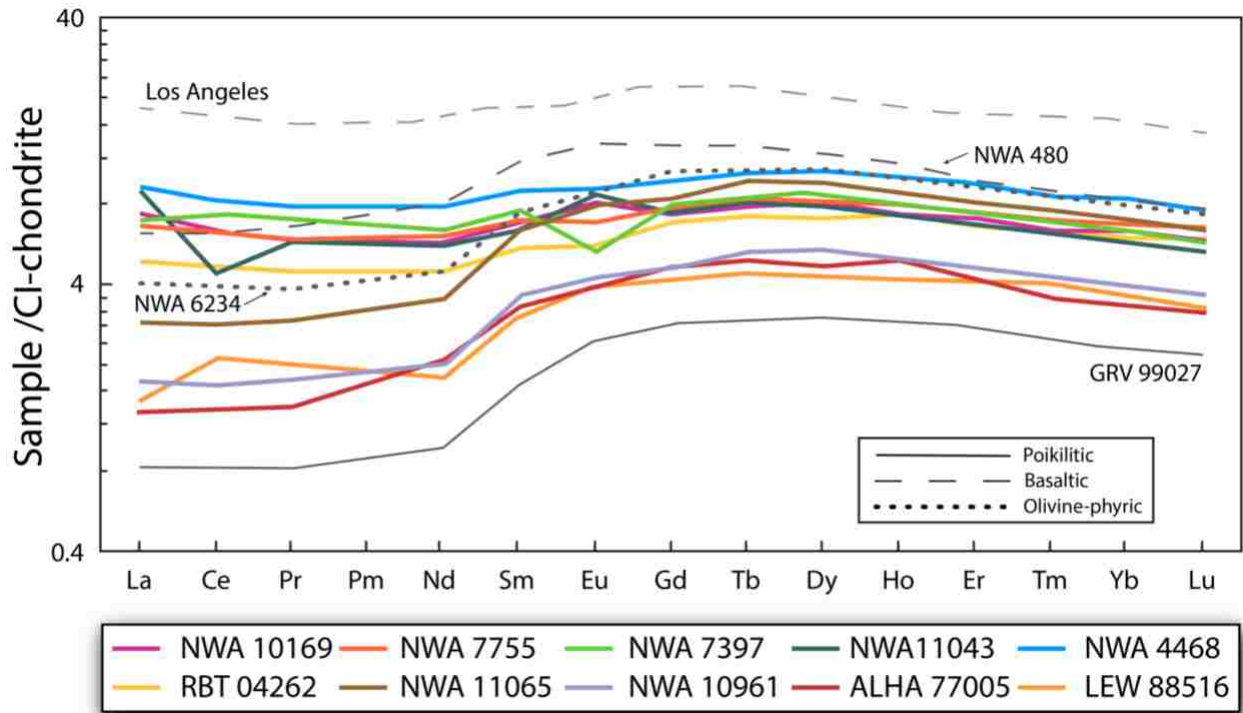
Figure 3.

Figure 4.

Figure 5.
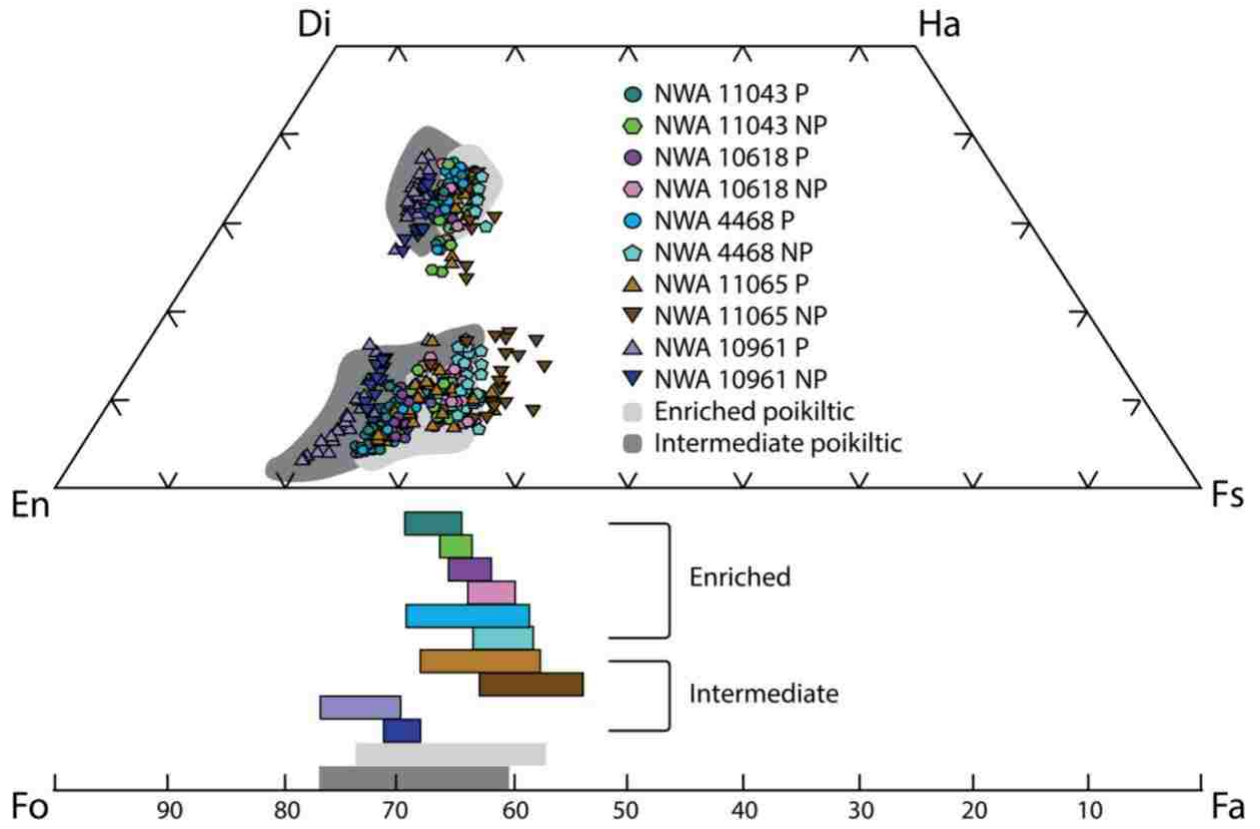
Figure 6.
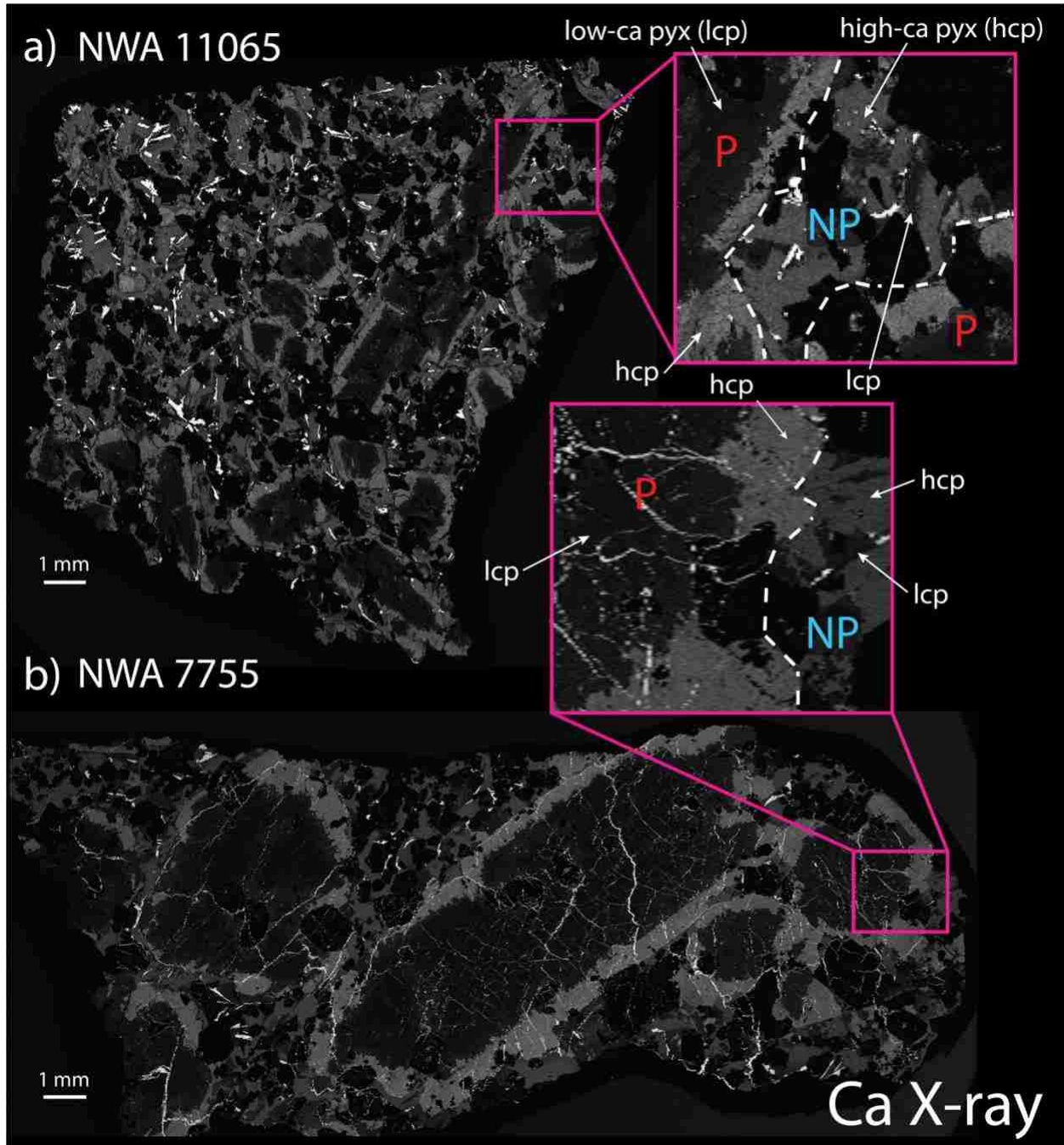
Figure 7.
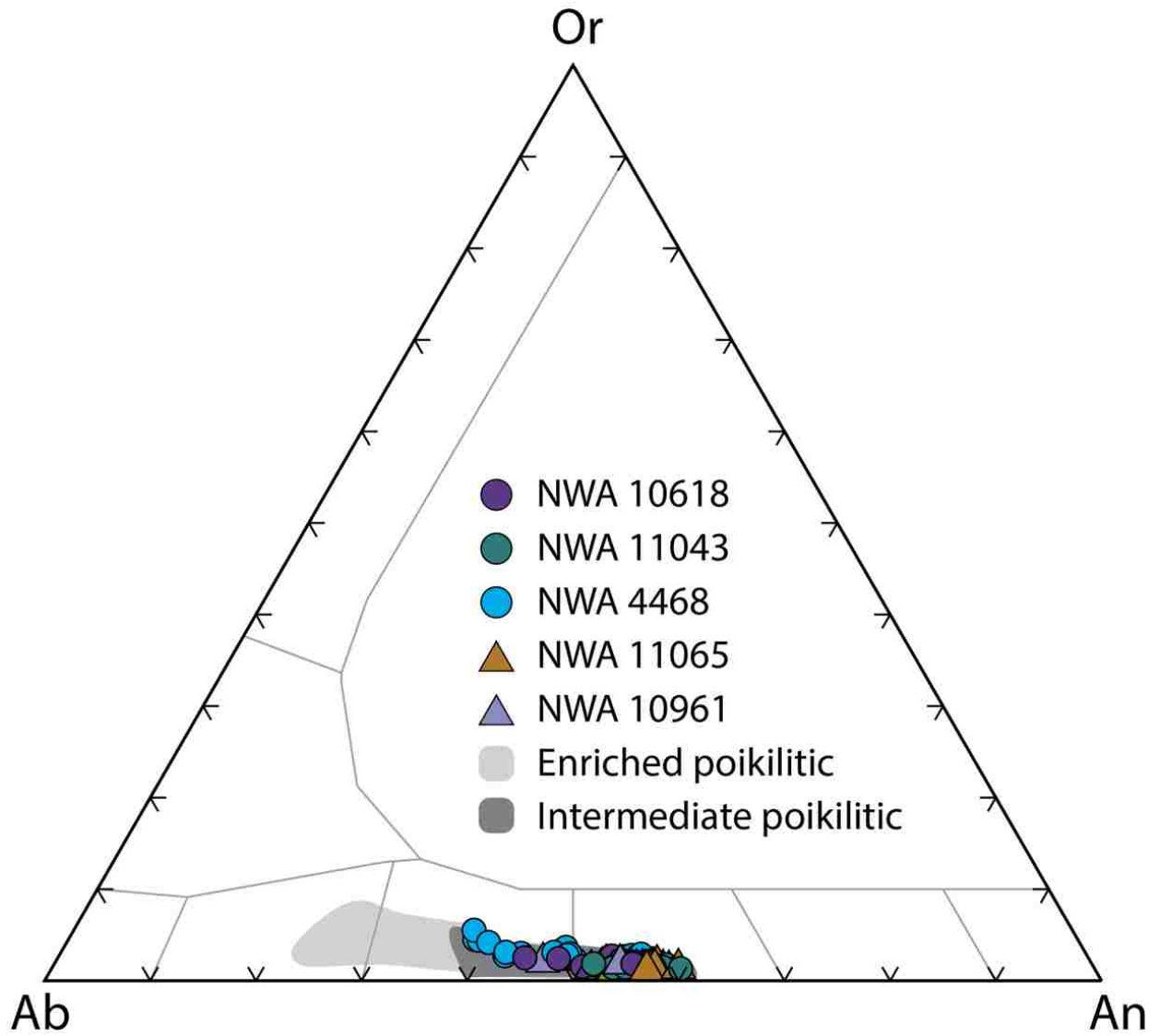
Figure 8.
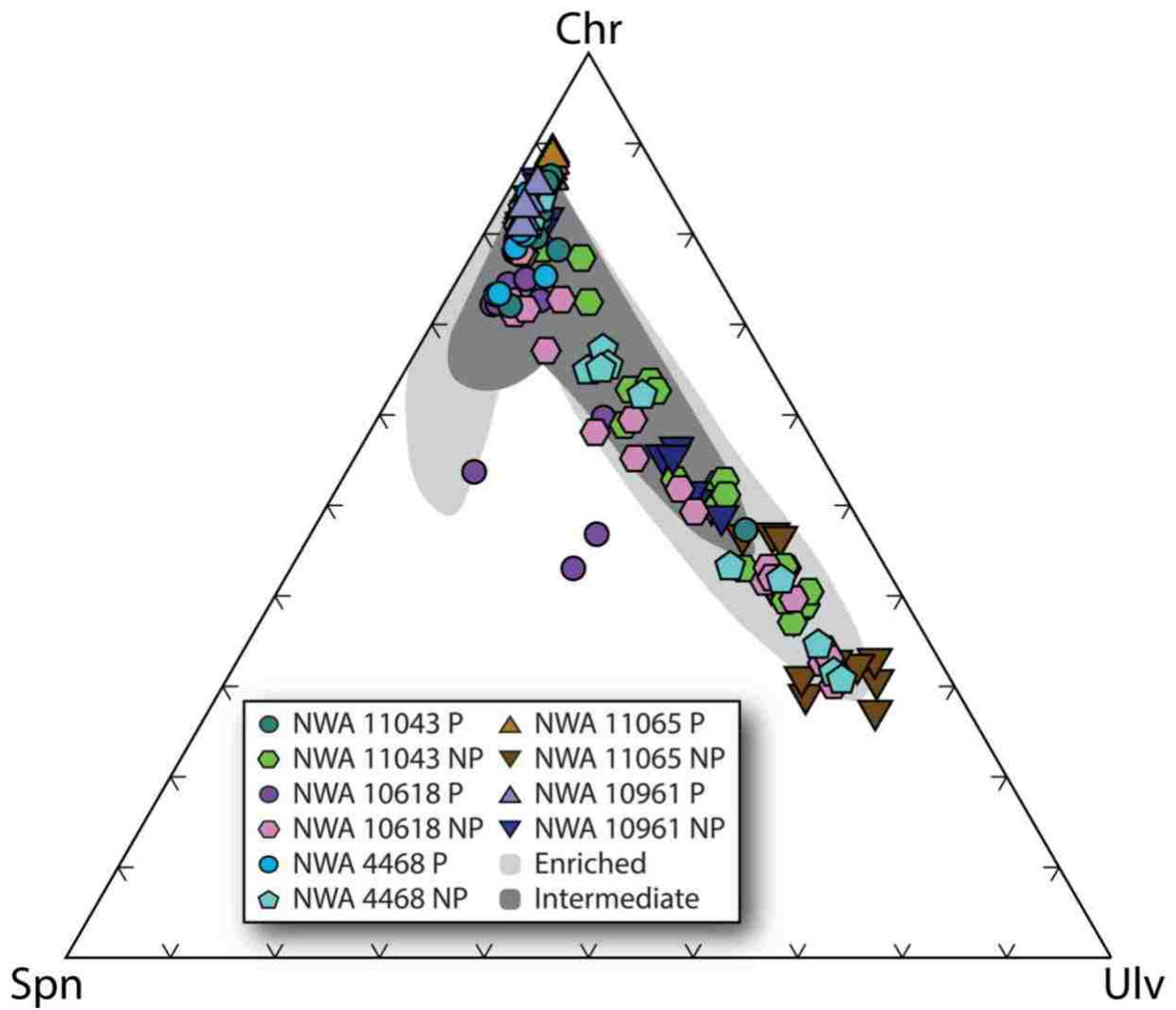
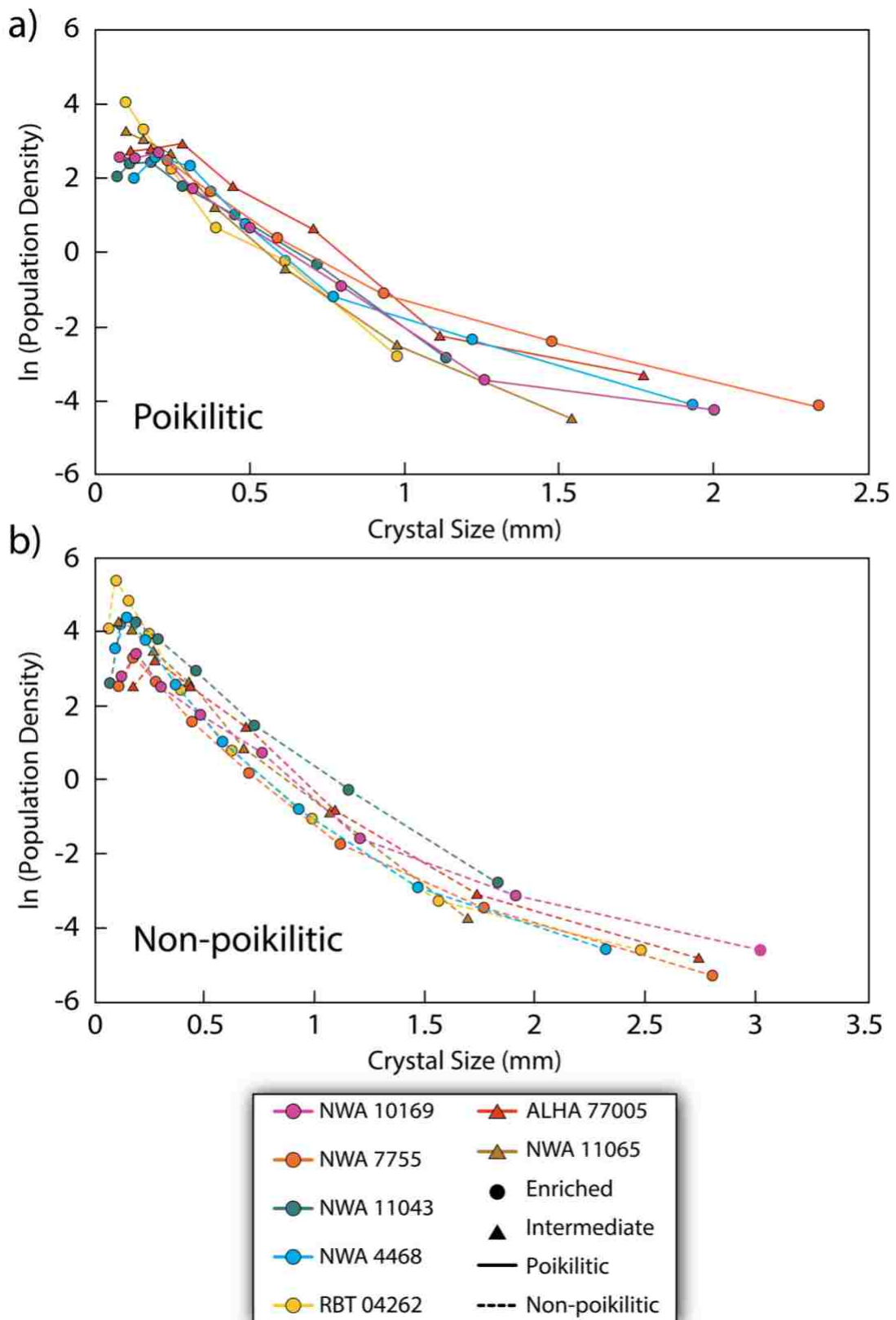**Figure 9.**
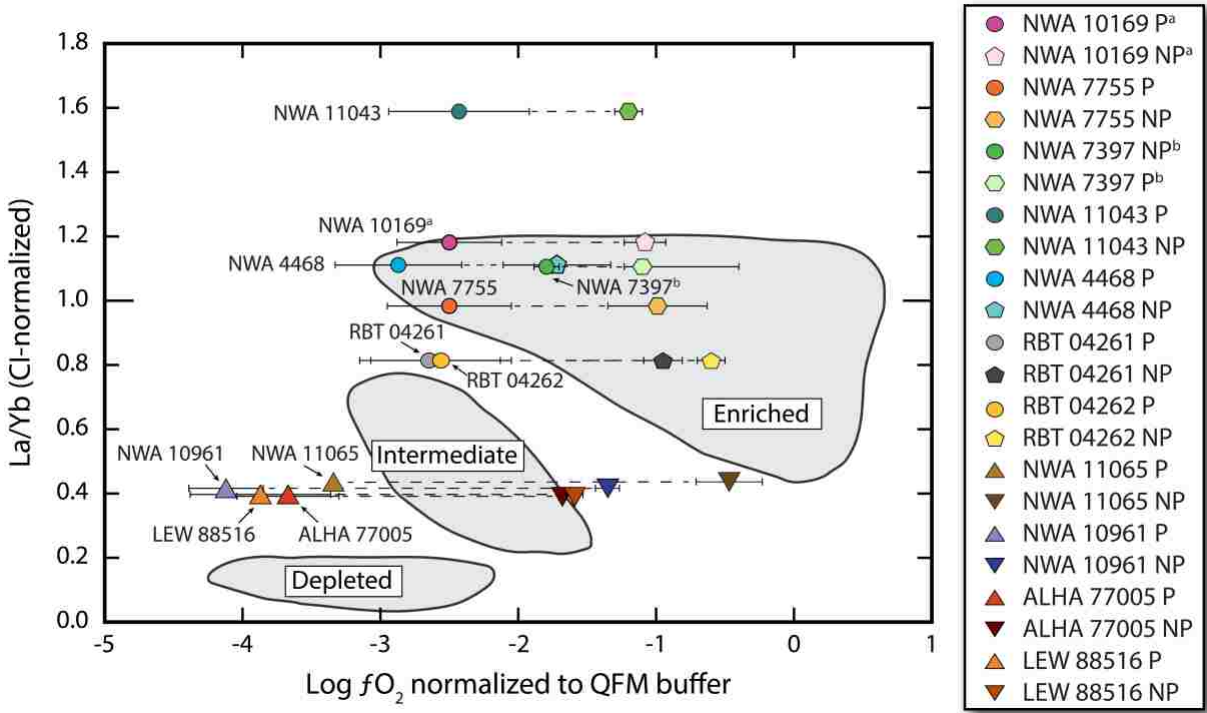
Figure 10.
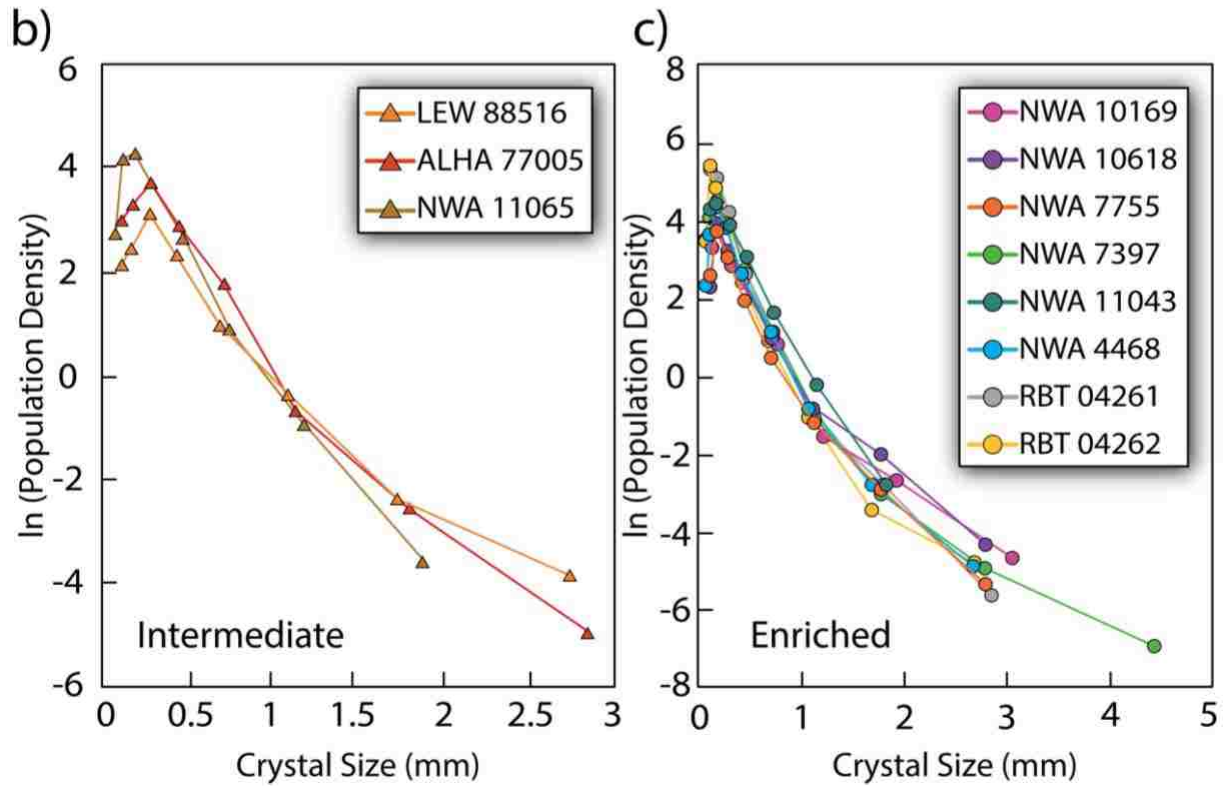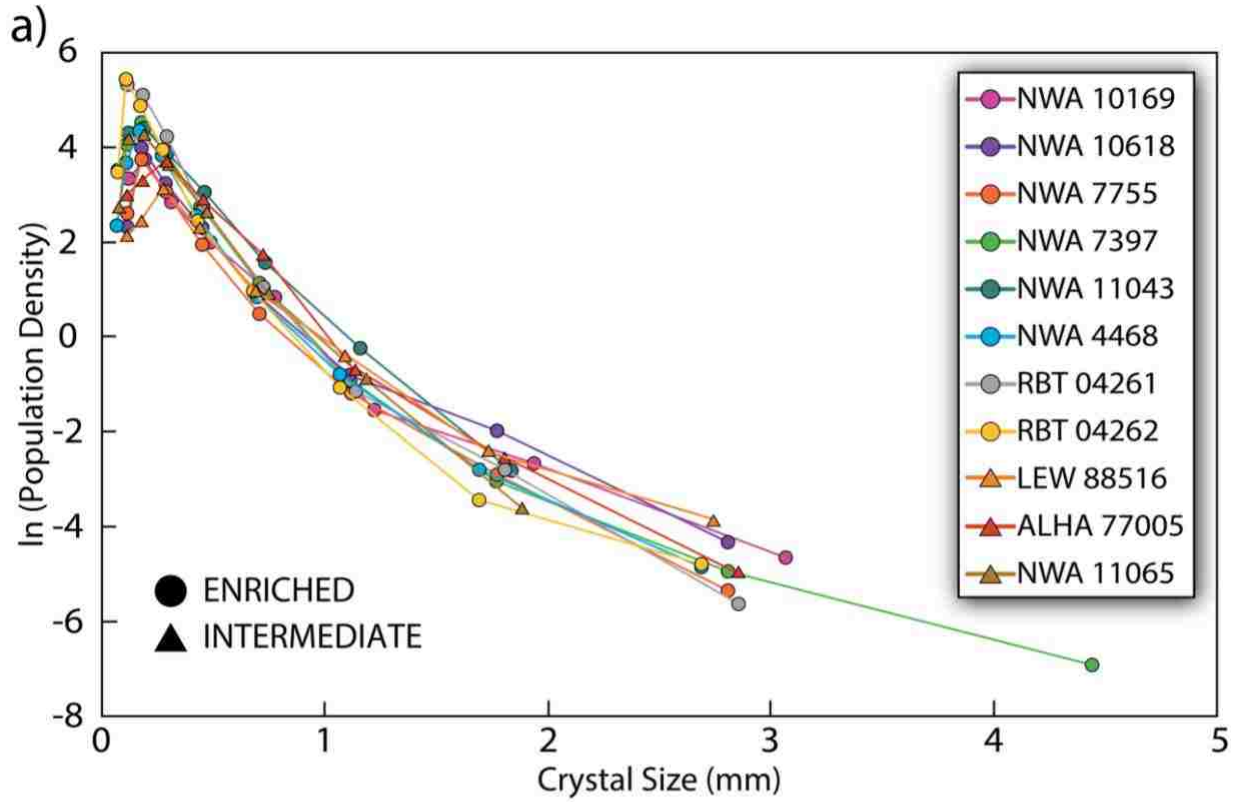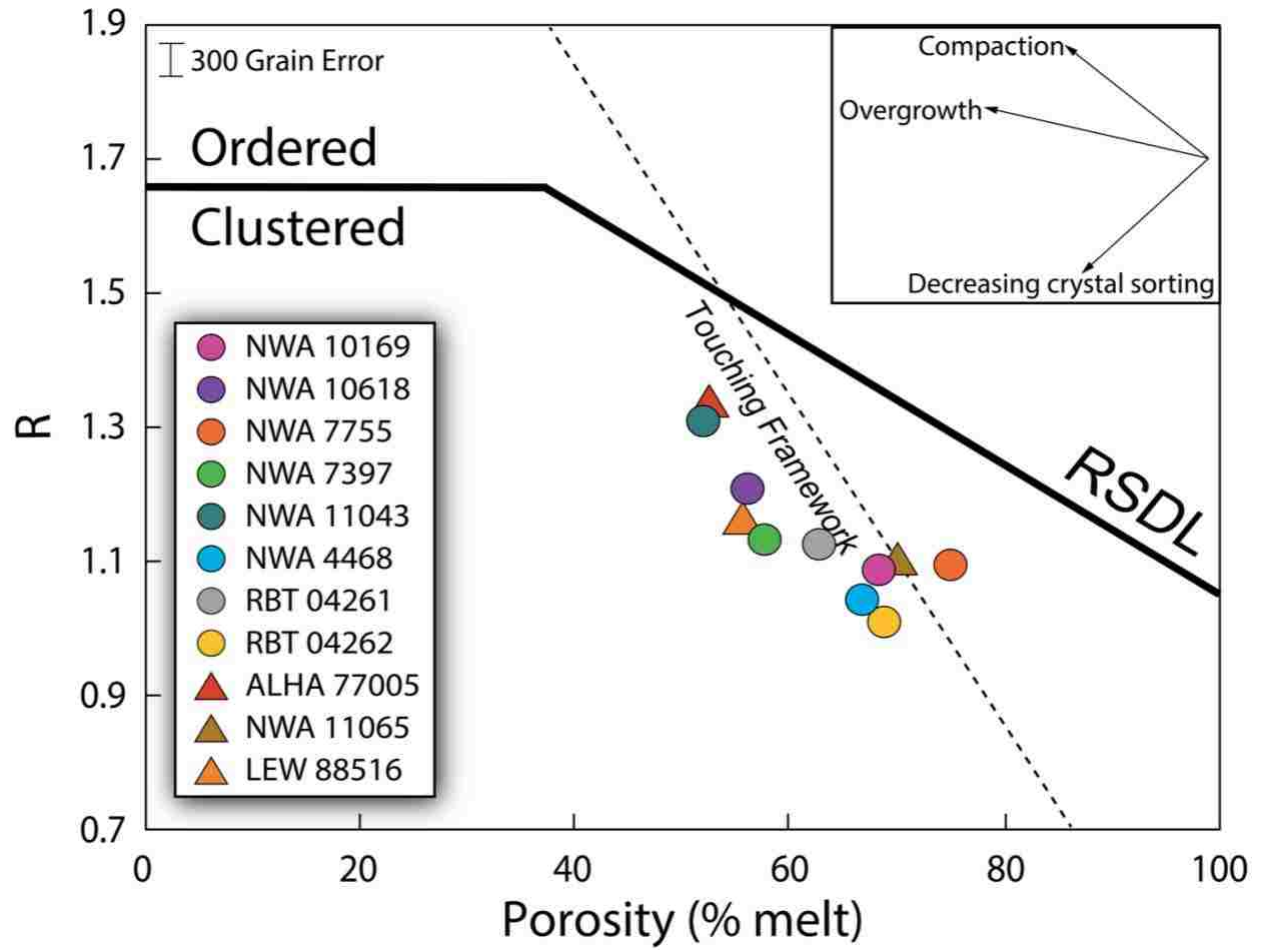
Figure 11.
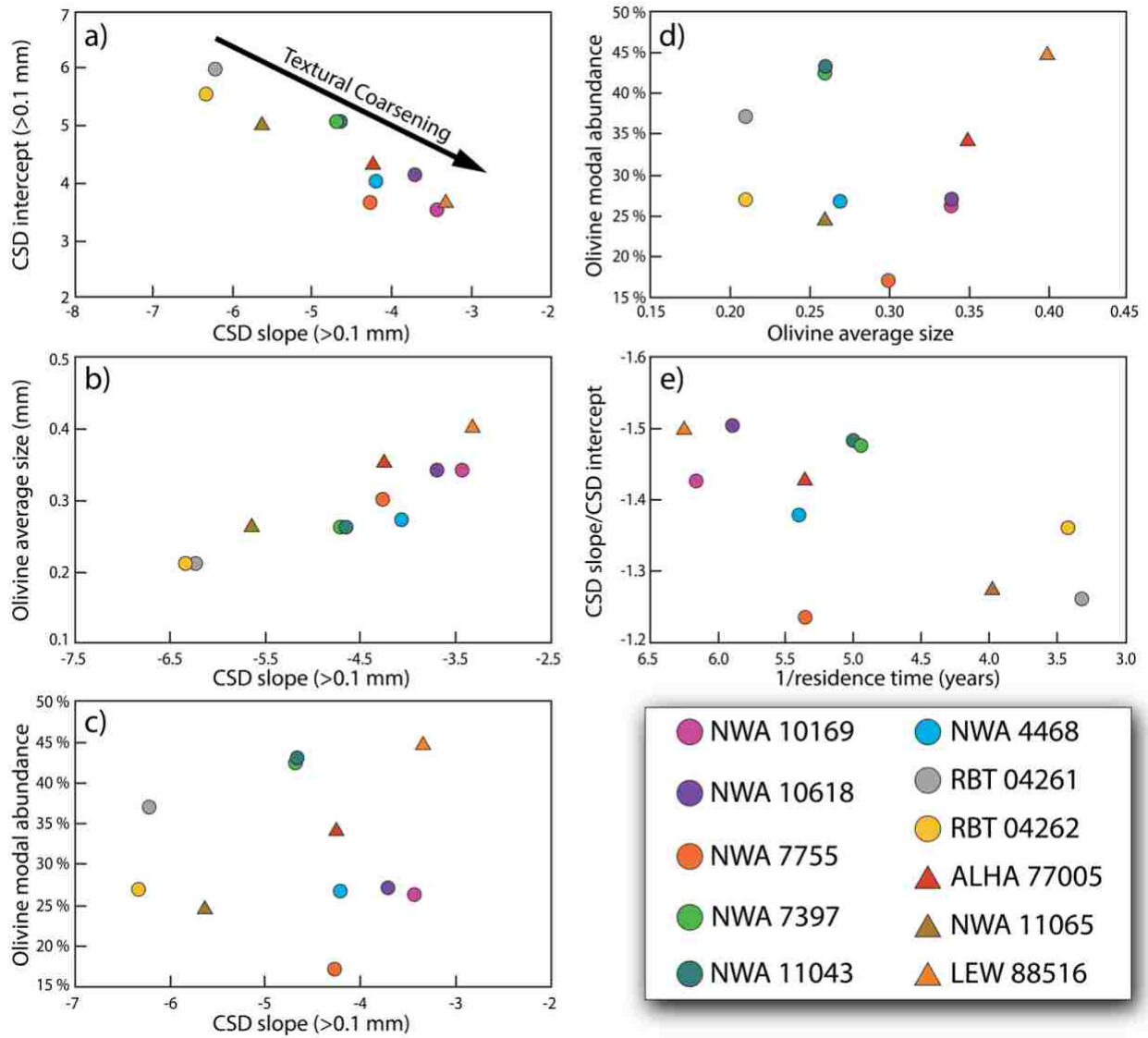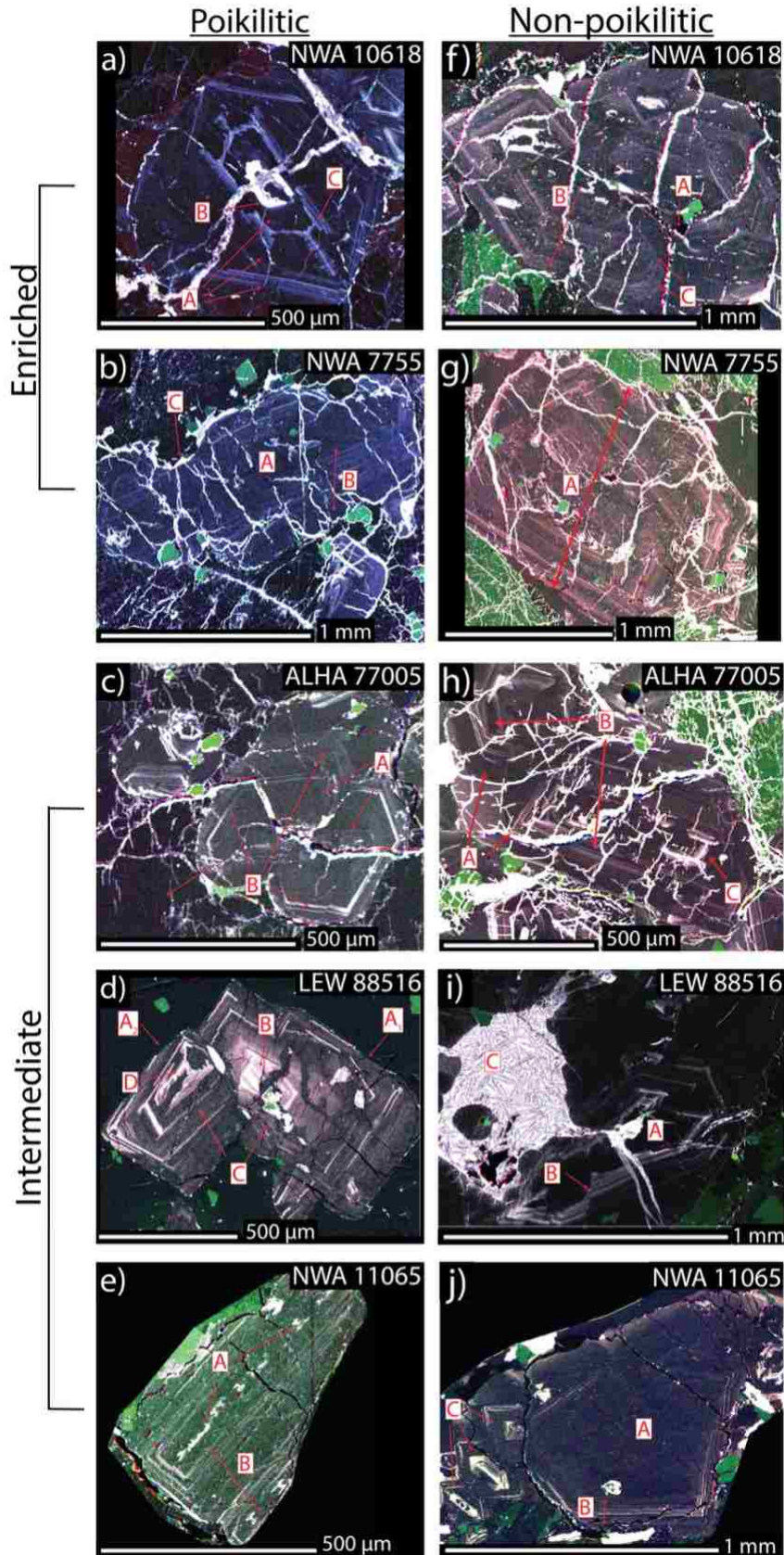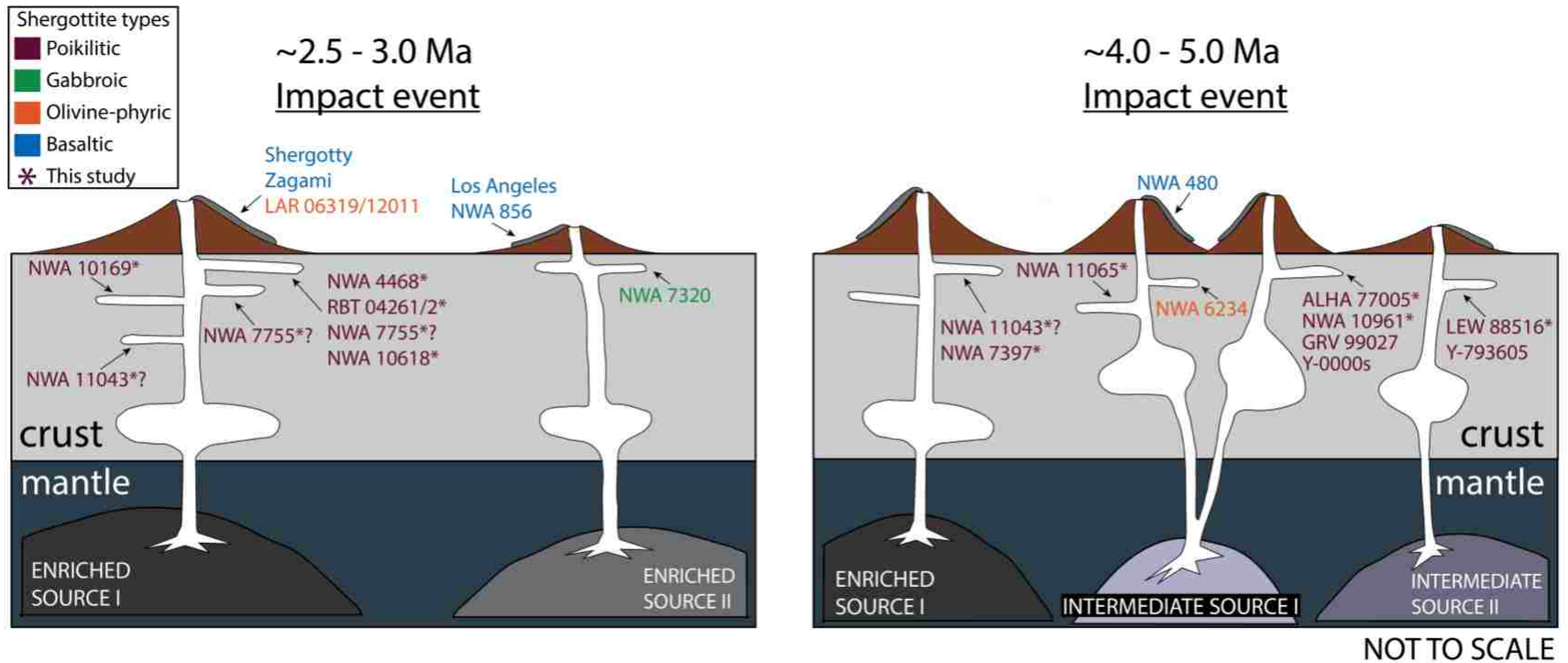
Figure 12.

Figure 13.

Figure 14.

Figure 15.

Shergottite crystallization ages ~150 Ma - ~225 Ma

References

Agee C. B., Wilson N. V., McCubbin F. M., Ziegler K., Polyak V. J., Sharp Z. D., Asmerom Y., Nunn M. H., Shaheen R., Thiemens M. H., Steele A., Fogel M. L., Bowden R., Glamoclija M., Zhang Z., and Elardo S. M. (2013) Unique meteorite from Early Amazonian Mars: Water-rich basaltic breccia Northwest Africa 7034. *Science* **339**, 780–785.

Ahrens T. J., Petersen C. F., and Rosenber J.T. (1969) Shock compression of feldspars. J. *Geophys. Res. Planet.***74**, 2727–2746.

Anand M., James S., Greenwood R. C., Johnson D., Franchi I. A., and Grady M. M. (2008) Mineralogy and geochemistry of shergottite RBT 04262. *Lunar Planet. Sci. XXXIV,* Lunar Planet. Inst., Houston. #2173 (abstr.).

Anderson A. T., Greenland L. P. (1969) Phosphorus fractionationdiagram as a quantitative indicator of crystallization differentiation of basaltic liquids. *Geochim. Cosmochim. Acta* **33**, 493–505.

Ballhaus C., Berry R. F., and Green, D. H. (1991) High pressure experimental calibration of the olivine-orthopyroxene-spinel oxygen geobarometer: implications for the oxidation state of the upper mantle. *Contrib. Mineral. Petrol.* **107**, 27–40.

Balta J. B., Sanborn M., and McSween H. Y. (2013) Magmatic history and parental melt composition of olivine-phyric shergottite LAR 06319: Importance of magmatic degassing and olivine antecrysts in Martian magmatism. *Meteorit. Planet. Sci.* **48**, 1359–1382.

Balta J. B., Sanborn M. E., Udry A., Wadhwa M., and McSween H. Y. (2015) Petrology and trace element geochemistry of Tissint, the newest shergottite fall. *Meteorit. Planet. Sci.* **50**, 63–85.

Balta J. B., Sanborn M. E., Mayne R. G., Wadhwa M., McSween H. Y., and Crossley S. D. (2016) Northwest Africa 5790: A previously unsampled portion of the upper part of the nakhlite pile. *Meteorit. Planet. Sci.* **52**, 36–59.

Barrat J. A., Gillet P., Sautter V., Jambon A., Javoy M., Göpel C., Lesourd M., Keller F., and Petit E. (2002a) Petrology and chemistry of the basaltic shergottite Northwest Africa 480. *Meteorit. Planet. Sci.* **37**, 487–499.

Barrat J. A., Jambon A., Bohn M., Gillet PH., Sautter V., Göpel C., Lesourd M., and Keller F. (2002b) Petrology and chemistry of the Picritic Shergottite North West Africa 1068 (NWA 1068). *Geochim. Cosmochim. Acta* **66**, 3505–3518.

Basu Sarbadhikari A., Day J. M. D., Liu Y., Rumble D. III., and Taylor L. A. (2009) Petrogenesis of olivine-phyric shergottite Larkman Nunatuk 06319: Implications for enriched components in Martian basalts. *Geochim. Cosmochim. Acta* **73**, 2190–2214.

Basu Sarbadhikari A., Goodrich C. A., Liu Y., Day J. M. D., and Taylor, L. A. (2011) Evidence for heterogeneous enriched shergottite mantle sources in Mars from olivine-hosted melt inclusions in Larkman Nunatak 06319. *Geochim. Cosmochim. Acta* **75**, 6803–6820.

Baziotis I., Asimow P. D., Ntaflos T., Boyce J. W., McCubbin F. M., Koroneos A., Perugini D., Flude S., Storey M., Liu Y. S., Klemme S., and Berndt J. (2017) Phosphorus zoning as a recorder of crystal growth kinetics: application to second-generation olivine in mantle xenoliths from the Cima Volcanic Field. *Contrib. Mineral. Petrol.* **172**, s00410-017-1376-7.

Bingkui M., Ziyuan O., Daode W., Yitai J., Guiqin W., and Yangting, L. (2004) A New Martian Meteorite from Antarctica: Grove Mountains (GRV) 020090. *Acta Geologica Sinica* **78**, 1034–1041.

Bläß U. W., Langenhorst F., and McCammon C. (2010) Microstructural investigations on strongly stained olivines of the chassignite NWA 2737 and implications for its shock history. *Earth Planet. Sci. Lett.* **300**, 255–263.

Bloch E., and Ganguly J. (2014) ^{176}Lu-^{176}Hf and ^{147}Sm-^{143}Nd ages of the Martian shergottites: Evaluation of the shock-resetting hypothesis through diffusion kinetic experiments and modeling, and petrological observations. *Earth Planet. Sci. Lett.* **395**, 173–183.

Brandon A. D., Puchtel I. A., Walker R. J., Day J. M. D., Irving A. J., and Taylor L. A. (2012) Evolution of the martian mantled inferred from the ^{187}Re-^{187}Os isotope and highly siderophile element abundance systematics of shergottite meteorites. *Geochim. Cosmochim. Acta* **76**, 206–235.

Boesenberg J. S., Ebel D. S., and Hewins R. H. (2004) An experimental study of phosphoran olivine and its significance in main group pallasites. *Lunar Planet. Sci. XXXV*, Lunar Planet. Inst., Houston. #1366 (abstr.).

Bogard D. D. and Johnson P. (1983) Martian gases in Antarctic Meteorite. *Science* **221**, 651–654.

Bogard D. D., Nyquist L. E., and Johnson P. (1984) Noble gas contents of shergottites and implications for the Martian origin of SNC meteorites. *Geochim. Cosmochim. Acta* **48**, 1723–1739.

Borg L. E. and Draper D. S. (2003) A petrogenetic model for the origin and compositional variation of the Martian basaltic meteorites. *Meteorit. Planet. Sci.* **38**, 1713–1731.

Borg L. E., Nyquist L. E., Taylor L. A., Wiesmann H., and Shih C. -Y. (1997) Constraints on Martian differentiation processes from Rb-Sr and Sm-Nd isotopic analyses of the basaltic shergottite QUE 94201. *Geochim. Cosmochim. Acta* **61**, 4915–4931.

Borg L. E., Norman M., Nyquist L. E., Bogard D., Snyder G., Taylor L. A., and Lindstrom M. (1999) Isotopic studies of ferroan anorthosite 62236: a young lunar crustal rock from a light rare-earth-element-depleted source. *Geochim. Cosmochim. Acta* **63**, 2679–2691.

Borg L. E., Nyquist L. E., Wiesmann H. and Reese Y. (2001) Rubidium-strontium and samarium-neodymium isotopic systematics of the lherzolithic shergottites ALH77005 and LEW88516: constraints on the petrogenesis of Martian meteorites. *Meteorit. Planet. Sci.* **36**, A25.

Borg L. E., Nyquist L. E., Wiesmann H., and Reese Y. (2002) Constraints on the petrogenesis of Martian meteorites from the Rb-Sr and Sm-Nd isotopic systematics of the lherzolitic shergottites ALHA77005 and LEW 88516. *Geochim. Cosmochim. Acta* **66**, 2037–2053.

Borg L. E., Nyquist L. E., Wiesmann H., Shih C. -Y., and Reese Y. (2003) The age of Dar al Gani 476 and the differentiation history of the martian meteorites inferred from their radiogenic isotopic systematics. *Geochim. Cosmochim. Acta* **67**, 3519–3536.

Borg L. E., Edmunson J. E., and Asmerom Y. (2005) Constraints on the U-Pb isotopic systematics of Mars inferred from a combined U-Pb, Rb-Sr, and Sm-Nd isotopic study of the Martian meteorite Zagami. *Geochim. Cosmochim. Acta* **69**, 5819–5830.

Borg L. E., Gaffney A. M., and Depaolo D. J. (2008) Preliminary Age of Martian Meteorite Northwest Africa 4468 and Its Relationship to the Other Incompatible-Element-enriched Shergottites. *Lunar Planet. Sci. XXXIX,* Lunar Planet. Inst., Houston. #1391 (abstr.).

Borg L. E., Symes S., Marks N. Gaffney A. and Shearer C. K (2012) Constraints on the composition and evolution of the Martian mantle from isotopic systematics of basaltic shergottites. *In Workshop on the Mantle of Mars: Insights from Theory, Geophysics, High-Pressure Experiments, and Meteorite* #6014 (abstr.).

Borg L. E., Brennecka G. A., and Symes S. J. (2016) Accretion timescale and impact history of Mars deduced from the isotopic systematics of martian meteorites. *Geochim. Cosmochim. Acta* **175**, 150–167.

Bouvier A., Blichert-Toft J., Vervoort J. D., and Albaréde F. (2005) The age of SNC meteorites and the antiquity of the Martian surface. *Earth Planet. Sci. Lett.* **240**, 221–233.

Bouvier A., Blichert-Toft J., Vervoort J. D., Gillet P., and Albaréde F. (2008a) The case for old basaltic shergottites. *Earth Planet. Sci. Lett.* **266**, 105–124.

Bouvier A., Vervoort J. D., and Patchett P.J. (2008b) The Lu-Hf and Sm-Nd isotopic composition of CHUR: Constraints from unequilibrated chondrites and implications for the bulk compositions of terrestrial planets. *Earth Planet. Sci. Lett.* **273**, 48–57.

Bouvier A., Blichert-Toft J., and Albaréde F. (2009) Martian meteorite chronology and the evolution of the interior of Mars. *Earth Planet. Sci. Lett.* **280**, 285–295.

Brandon A. D., Puchtel I. S., Walker R. J., Day J. M. D., Irving A., and Taylor L. A. (2012) Evolution of the Martian mantle inferred from the ^{187}Re-^{187}Os isotope and highly siderophile element abundance systematics of shergottite meteorites. *Geochim. Cosmochim. Acta* **76**, 206–235.

Brennecka G. A., Borg L. E., and Wadhwa M. (2014) Insights into the Martian mantle: The age and isotopics of the meteorite fall Tissint. *Meteorit. Planet. Sci.* **49**, 412–418.

Bridges J. C., and Warren P. H. (2006) The SNC meteorites: basaltic igneous processes on Mars. *Journal of the Geological Society*, **163**, 229–251.

Brunet F. and Chazot G. (2001) Partitioning of phosphorus between olivine, clinopyroxene and silicate glass in a spinel xenolith from Yemen. *Chem. Geol.* **176**, 51–72.

Cashman K. V. and Marsh B. D. (1988) Crystal size distribution (CSD) in rocks and the kinetics and dynamics of crystallization, II: Makaopuhi lava lake. *Contrib. Mineral. Petrol.* **99**, 292–305.

Castle N. and Herd C. D. K. (2017) Experimental petrology of the Tissint meteorite: Redox estimates, crystallization curves, and evaluation of petrogenetic models. *Meteorit. Planet. Sci.* **52**, 125–146.

Castle N. and Herd C. D. K. (2018) Experimental investigation into the effects of oxidation during petrogenesis of the Tissint meteorite. *Meteorit. Planet. Sci.* **53**, 1341–1363.

Cassata W. S. and Borg L. E. (2015) ^{40}Ar/^{39}Ar systematics of shergottite NWA 4468. *Lunar Planet. Sci. XXXVI,* Lunar Planet. Inst., Houston. #2742 (abstr.).

Christen F., Eugster O., and Busemann H., (2005) Mars ejection times and neutron capture effects of the nakhlites Y000593 and Y000749, the olivine-phyric shergottite Y980459, and the lherzolite NWA1950. *Antarctic Meteorite Research,* **18**, 117–132.

Combs L. M., Udry A., and Day J. M. D. 2016. Petrography and Mineral Chemistry of the New Enriched Lherzolitic Shergottite Northwest Africa 10169. *Lunar Planet. Sci. XXXVII,* Lunar Planet. Inst., Houston. #2804 (abstr.).

Combs L. M., Udry A., Howarth G. H., Lapen T. J., Righter M., Gross J., Day J. M. D., and Rahib R. R. (2018) Petrology of the enriched poikilitic shergottite Northwest Africa 10169: Insight into the martian interior. *Lunar Planet. Sci. XXXIX,* Lunar Planet. Inst., Houston. #2083 (abstr.).

Combs L. M. (2018) Petrology and geochemistry of the enriched poikilitic shergottite Northwest Africa 10169: Insight into the martian interior (Master's thesis) University of Nevada, Las Vegas, Las Vegas, NV, USA.

Crisp J. A. (1984) Rates of Magma Emplacement and Volcanic Output. *J. Volc. Geotherm. Res.,* **20**, 177–211.

Crozaz G. and Wadhwa M. (2001) The terrestrial alteration of Saharan shergottites Dar al Gani 476 and 489: A case study of weathering in a hot desert environment. *Geochim. Cosmochim. Acta* **65**, 971–977.

Crozaz G., Floss C., and Wadhwa M. (2003) Chemical alteration and REE mobilization in meteorites from hot and cold deserts. *Geochim. Cosmochim. Acta* **67**, 4727–4741.

Day J. M. D., Taylor L. A., Floss C., and McSween H. Y. (2006a) Petrology and chemistry of MIL 03346 and its significance in understanding the petrogenesis of nakhlites on Mars. *Meteorit. Planet. Sci.* **41**, 581–606.

Day J. M. D. and Taylor L. A. (2007) On the structure of mare basalt lava flows from textural analysis of the LaPaz Icefield and Northwest Africa 032 lunar meteorites. *Meteorit. Planet. Sci.* **42**, 3–17.

Debaille V., Yin Q. -Z., Brandon A. D., and Jacobsen B. (2008) Martian mantle mineralogy investigated by the ^{176}Lu-^{176}Hf and ^{147}Sm-^{143}Nd systematics of shergottites. *Earth Planet. Sci. Lett.* **269**, 186–199.

Donohue P. H. and Neal C. R. (2015) Quantitative textural analysis of ilmenite in Apollo 17 high-titanium mare basalts. *Geochim. Cosmochim. Acta* **149**, 115–130.

Dreibus G., Spettel B., Haubold R., Jochum K. P., Palme H., Wolf D., and Zipfel J. (2000) Chemistry of a new shergottite: Sayh al Uhaymir 005. *Meteorit. Planet. Sci.* **35**, A49.

Ennis M. J. and McSween H. Y. (2014) Crystallization kinetics of olivine-phyric shergottites. *Meteorit. Planet. Sci.* **49**, 1440–1445.

Eugster O., Busemann H., Lorenzetti S., and Terribilini D. (2002) Ejection ages from krypton-81-krypton-83 dating and pre-atmospheric sizes of Martian meteorites. *Meteorit. Planet. Sci.* **37**, 1345–1360.

Ferdous J., Brandon A. D., Peslier A. H., and Pirotte Z. (2017) Evaluating crustal contributions to enriched shergottites from the petrology, trace elements, and Rb-Sr and Sm-Nd isotope systematics of Northwest Africa 856. *Geochim. Cosmochim. Acta* **211**, 280–306.

Filiberto J., Musselwhite D. S., Gross J., Burgess K., Le L., and Treiman A. H. (2010) Experimental petrology, crystallization history, and parental magma characteristics of olivine-phyric shergottite NWA 1068: Implications for the petrogenesis of "enriched" olivine-phyric shergottites. *Meteorit. Planet. Sci.* **45**, 1258–1270.

Filiberto J., and Dasgupta R. (2011) Fe^{2+}-Mg partitioning between olivine and basaltic melts: Applications to genesis of olivine-phyric shergottites and conditions of melting in the Martian interior. *Earth Planet. Sci. Lett.* **304**, 527–537.

Filiberto J., Chin E., Day J. M. D., Franchi I. A., Greenwood R. C., Gross J., Penniston- Dorland S. C., Schwenzer S. P., and Treiman A. H. (2012) Geochemistry of intermediate olivine-phyric shergottite Northwest Africa 6234, with similarities to basaltic shergottite Northwest Africa 480 and olivine-phyric shergottite Northwest Africa 2990. *Meteorit. Planet. Sci.* **47**, 1256–1273.

Filiberto J., Gross J., Trela J. and Ferré E. C. (2014) Gabbroic Shergottite Northwest Africa 6963: An intrusive sample of Mars. *Am. Mineral.* **99**, 601–606.

Filiberto J. (2017) Geochemistry of Martian basalts with constraints on magma genesis. *Chem. Geol.* **466**, 1–14.

Floss C. and Crozaz G. (1991) Ce anomalies in the LEW 85300eucrite; evidence for REE mobilization during Antarctic weathering. *Earth Planet. Sci. Lett.* **107**, 13–24.

Ford C. E., Russell D. G., Craven J. A., and Fisk M. R. (1983) Olivine-Liquid Equilibria: Temperature, Pressure, and Composition Dependence of the Crystal/Liquid Cation Partition Coefficients for Mg, Fe^{2+}, Ca and Mn. *J. Petrol.* **24**, 256–266.

Fritz J., Artemieva N., and Greshake A. (2005) Ejection of Martian meteorites. *Meteorit. Planet. Sci.* **40**, 1393–1411.

Fritz J., Greshake A., and Fernandes V. A. (2017) Revising the shock classification of meteorites. *Meteorit. Planet. Sci.* **52**, 1216–1232.

Garrido C. J., Kelemen P. B., and Hirth G. (2001) Variation of cooling rate with depth in lower crust formed at an oceanic spreading ridge: Plagioclase crystal size distributions in gabbros from the Oman ophiolite. *Geochem. Geophys. Geosys.* **2**, 1–21.

Gleason J. D., Kring D. A., Hill D. H., and Boynton W. V. (1997) Petrography and bulk chemistry of Martian lherzolite LEW88516. *Geochim. Cosmochim. Acta* **61**, 4007–4014.

Gillet P., Barrat J. A., Beck P., Marty B., Greenwood R. C., Franchi I. A., Bohn M., and Cotton J. (2005) Petrology, geochemistry, and cosmic-ray exposure age of lherzolitic shergottite Northwest Africa 1950. *Meteorit. Planet. Sci.* **40**, 1175–1184.

Ghiorso M. S., and Sack R. O. (1995) Chemical mass transfer in magmatic processes IV. A revised and internally consistent thermodynamic model for the interpolation and extrapolation of liquid-solid equilibria in magmatic systems at elevated temperatures and pressures. *Contrib. Mineral. Petrol.* **119**, 197–212.

Goodrich C. A., (2002) Olivine-phyric martian basalts: A new type of shergottite. *Meteorit. Planet. Sci.* **37**, B31–B34.

Goodrich C. A. (2003) Petrogenesis of olivine-phyric shergottites Sayh al Uhaymir 005 and Elaphant Moraine A79001 lithology A. *Geochim. Cosmochim. Acta* **67**, 3735–3771.

Goodrich C. A., Anne C., Herd C. D. K., and Taylor L. A., (2003) Spinels and oxygen fugacity in olivine-phyric and lherzolitic shergottites. *Meteorit. Planet. Sci.* **38**, 1773–1792.

Gross J., Treiman A. H., Filiberto J., and Herd C. D. K. (2011) Primitive olivine-phyric shergottite NWA 5789: Petrography, mineral chemistry, and cooling history imply a magma similar to Yamato-980459. *Meteorit. Planet. Sci.* **46**, 116–133.

Gross J., Filiberto J., Herd C. D. K., Daswani M. M., Schwenzer S. P., and Treiman A. H. (2013) Petrography, mineral chemistry, and crystallization history of olivine-phyric shergottite NWA 6234: A new melt composition. *Meteorit. Planet. Sci.* **48**, 854–871.

Harrison, T.M., and Watson, E.B. (1984) The behavior of apatite during crustal anatexis: Equilibrium and kinetic considerations. *Geochim. Cosmochim. Acta* **48**, 1467–1477.

Harvey R. P., Wadhwa M., McSween H. Y., and Crozaz G. (1993) Petrography, mineral chemistry, and petrogenesis of Antarctic Shergottite LEW88516. *Geochim. Cosmochim. Acta* **57**, 4769–4783.

He Q., and Xiao L. (2014) Preliminary petrographic and melt-inclusion studies on the Northwest Africa 7397: Another enriched "lherzolitic" shergottite. *Lunar Planet. Sci. XXXXV,* Lunar Planet. Inst., Houston. #1668. (abstr.).

Herd C. D. K., Papike J. J., and Brearley A. J. (2001) Oxygen fugacity of martian basalts from electron microprobe oxygen and TEM-EELS analyses of Fe-Ti oxides. *Am. Mineral.* **86**, 1015–1024.

Herd C. D. K., Borg L. E., Jones J. H., and Papike J. J. (2002) Oxygen fugacity and geochemical variations in the martian basalts: Implications for martian basalt petrogenesis and the oxidation state of the upper mantle of Mars. *Geochim. Cosmochim. Acta* **66**, 2025–2036.

Herd C. D. K. (2003) The oxygen fugacity of olivine-phyric martian basalts and the components within the mantle and crust of Mars. *Meteorit. Planet. Sci.* **38**, 1793–1805.

Herd C. D. K. (2006) Insights into the redox history of the NWA 1068/1110 martian basalt from mineral equilibria and vanadium oxybarometry. *Am. Mineral.* **91**, 1616–1627.

Herd C. D. K., Walton E. L., Agee C. B., Muttik N., Ziegler K., Shearer C. K., Bell A. S., Santos A. R., Burger P. V., Simon J. I., Tappa M. J., McCubbin F. M., Gattacceca J., Lagroix F., Sanborn M. E., Yin Q. -Z., Cassata W. S., Borg L., Lindvall R. E., Kruijer T. S., Brennecka G. A., Kleine T., Nishiizumi K., and Caffee M. W. (2017) The Northwest Africa 8159

martian meteorite: Expanding the martian sample suite to the early Amazonian. *Geochim. Cosmochim. Acta* **218**, 1–26.

Higgins M. D. (2000) Measurement of crystal size distributions. *Am. Mineral.* **85**, 1105–1116.

Higgins M. D. (2006) Quantitative textural measurements in igneous and metamorphic petrology. *Cambridge, UK: Cambridge University Press*, 256.

Higgins M. D. (2011) Textural coarsening in igneous rocks. *Int. Geol. Rev.* **53**, 354–376.

Howarth G. H., Pernet-Fisher J. F., Balta J. B., Barry P. H., Bodnar R. J., and Taylor L. A. (2014) Two-stage polybaric formation of the new enriched pyroxene-oikocrystic, lherzolitic shergottite, NWA 7397. *Meteorit. Planet. Sci.* **49**, 1812–1830.

Howarth G. H., Pernet-Fisher J. F., Bodnar R. J., and Taylor L. A. (2015) Evidence for the exsolution of Cl-rich fluids in martian magmas: Apatite petrogenesis in the enriched lherzolitic shergottite Northwest Africa 7755. *Geochim. Cosmochim. Acta* **166**, 234–248.

Howarth G. H., Liu Y., Chen, Y., Pernet-Fisher J. F., and Taylor L. A. (2016) Postcrystallization metasomatism in shergottites: Evidence from the paired meteorites LAR 06319 and LAR 12011. *Meteorit. Planet. Sci.* **51**, 2061–2072.

Howarth G. H., and Udry A. (2017) Trace elements in olivine and the petrogenesis of the intermediate, olivine-phyric shergottite NWA 10170. *Meteorit. Planet. Sci.* **52**, 391–409.

Howarth G. H., Udry A., and Day J. M. D. (2018) Petrogenesis of basaltic shergottite Northwest Africa 8657: Implications for fO_2 correlations and element redistribution during shock melting shergottites. *Meteorit. Planet. Sci.* **53**, 249–267.

Hsu W., Guan Y., Wang H., Leshin L. A., Wang R., Zhang W., Chen X., Zhang F., and Lin C. (2004) The lherzolitic shergottite Grove Mountains 99027: Rare earth element geochemistry. *Meteorit. Planet. Sci.* **39**, 701–709.

Hui H., Peslier A., Lapen T. J., Shafer J. T., Brandon A. D., and Irving A. J. (2011) Petrogenesis of basaltic shergottite Northwest Africa 5298: Closed-system crystallization of an oxidized mafic melt. *Meteorit. Planet. Sci.* **46**, 1313–1328.

Ikeda Y. (1997) Petrology and mineralogy of the Y-793605 Martian meteorite. *Antarctic Meteorite Research* **10**, 13.

Ikeda Y. (1998) Petrology of magmatic silicate inclusions in the Allan Hills 77005 lherzolitic shergottite. *Meteorit. Planet. Sci.* **33**, 803–812.

Jambon A., Barrat J. A., Sautter V., Gillet Ph., Göpel C., Javoy M., Joron J. L., and Lesourd M. (2002) The basaltic shergottite Northwest Africa 856: Petrology and chemistry. *Meteorit. Planet. Sci.* **37**, 1147–1164.

Jeanloz R. F. and Ahrens T. J. (1976) Shock-induced melting of minerals in basalt. *Eos, Transactions of the American Geophysical Union* **57**, 160.

Jerram D. A., Cheadle M. J., Hunter R. H., and Elliott M. T. (1996) The spatial distribution of grains and crystals in rocks. *Contrib. Mineral. Petrol.* **125**, 60–74.

Jerram D. A., Cheadle M. J., and Philpotts A. R. (2003) Quantifying the building blocks of igneous rocks: Are clustered crystal frameworks the foundation? *J. Petrol.* **44**, 2033–2051.

Jiang Y., and Hsu W. (2012) Petrogenesis of Grove Mountains 020090: An enriched "lherzolitic" shergottite. *Meteorit. Planet. Sci.* **47**, 1419–1435.

Jones J. (2003) Constraints on the structure of the Martian interior determined from the chemical and isotopic systematics of SNC meteorites. *Meteorit. Planet. Sci.* **38**, 1807–1814.

Kelemen P. B., Koga K., and Shimizu N. (1997) Geochemistry of gabbro sills in the crust- mantle transition zone of the Oman ophiolite: implications for the origin of the oceanic lower crust. *Earth Planet. Sci. Lett.* **146**, 475–488.

Keller, L. P., Treiman A. H., and Wentworth S. J. (1992) Shock Effects in the Shergottite LEW88516: Optical and Electron Microscope Observations. *Meteorit. Planet. Sci.* **27**, 242.

Kong P., Fabel D., Brown R., Freeman S. (2007) Cosmic-ray exposure age of Martian meteorite GRV 99027. *Sci. China Ser. D-Earth Sci.* **50**, 1521–1524.

Lapen T. J., Brandon A. D., Beard B. L., Peslier A. H., Lee C-T. A., and Dalton H. A. (2008) Lu-Hf age and isotope systematics of the olivine-phyric shergottite RBT-04262 and implications for the sources of enriched shergottites. *Lunar Planet. Sci. XXXIX,* Lunar Planet. Inst., Houston. #2073. (abstr.).

Lapen T. J., Righter M., Brandon A. D., Beard B. L., Shafer J., and Irving A. J. (2009) Lu-Hf isotope systematics of NWA4468 and NWA2990: Implications for the sources of shergottites. *Lunar Planet. Sci. XXXX,* Lunar Planet. Inst., Houston. #2376. (abstr.).

Lapen T. J., Righter M., Brandon A. D., Debaille V., Beard B. L., Shafer J. T., and Peslier A. H. (2010) A Younger Age for ALH84001 and Its Geochemical Link to Shergottite Sources in Mars. *Science* **328**, 347–351.

Lapen T. J., Righter M., Andreasen R., Irving A. J., Satkoski A. M., Beard B. L., Nishiizumi K., Jull A. J. T., and Caffee M. W. (2017) Two billion years of magmatism recorded from a single Mars meteorite ejection site. *Science Advances* **3**, e1600922.

Lentz R. C. F. and McSween H. Y. (2005) A textural examination of the Yamato 980459 and Los Angeles shergottites using crystal size distribution analysis. *Antarctica Meteorite Research*

18, 66–82.

Lin Y., Guan Y., Wang D., Kimura M., and Leshin L. A. (2005) Petrogenesis of the new lherzolitic shergottite Grove Mountains 99027: Constraints of petrography, mineral chemistry, and rare earth elements. *Meteorit. Planet. Sci.* **40**, 1599–1619.

Lin Y. T., Qi L., Wang G. Q., and Xu L. (2008) Bulk chemical composition of lherzolitic shergottite Grove Mountains 99027-Constraints on the mantle of Mars. *Meteorit. Planet. Sci.* **43**, 1179–1187.

Lin Y., Hu S., Miao B., Xu L., Liu Y., Xie L., Feng L., and Yang. J. (2013) Grove Mountains 020090 enriched lherzolitic shergottite: A two-stage formation model. *Meteorit. Planet. Sci.* **48**, 1572–1589.

Liu T., Li C. and Lin Y. (2011) Rb-Sr and Sm-Nd isotopic systematics of the lherzolitic shergottite GRV 99027. *Meteorit. Planet. Sci.* **46**, 681–689.

Lodders K. (1998) A survey of shergottite, nakhlite and chassigny meteorites whole-rock compositions. *Meteorit. Planet. Sci.* **33**, A183–A190.

Maloy A. K., and Treiman A. H. (2007) Evaluation of image classification routines for determining modal mineralogy of rocks from X-ray maps. *Am. Mineral.* **92**, 1781–1788.

Marks N. E., Borg L. E., Gaffney A. M., and DePaolo D. (2010) The relationship of Northwest Africa 4468 to the other incompatible-element enriched Shergottites inferred from its Rb-Sr and Sm-Nd isotopic systematics (Conference. *Lunar Planet. Sci. XXXXI,* Lunar Planet. Inst., Houston. #2064. (abstr.).

Marsh B. D. (1988) Crystal size distribution (CSD) in rocks and kinetics and dynamics of crystallization. *Contrib. Mineral. Petrol.* **99**, 277–291.

Marsh B. D. (1998) On the interpretation of crystal size distribution in magmatic systems. *J. Petrol.* **39**, 553–599.

McCanta M. C., Beckett J. R., and Stolper E. M. (2016) Correlations and zoning patterns of phosphorus and chromium in olivine from H chondrites and the LL chondrite Semarkona. *Meteorit. Planet. Sci.* **51**, 520–546.

McCoy T. J. and Lofgren G. (1999) Crystallization of the Zagami shergottite: An experimental study. *Earth Planet. Sci. Lett.* **173**, 397–411.

McCubbin F. M., Boyce J. W., Srinivasan P., Santos A. R., Elardo S. M., Filiberto J., Steele A., and Shearer C. K. (2016) Heterogeneous distribution of H_2O in the martian interior: Implications for the abundance of H_2O in depleted and enriched mantle sources. *Meteorit. Planet. Sci.* **51**, 2036–2060.

McSween H. Y. Jr. (1994) What we have learned about Mars from SNC meteorites. *Meteorit. Planet. Sci.* **29**, 757–779.

McSween, Jr., H. Y., Eisenhour D. D., Taylor L. A., Wadhwa M., and Crozaz G. (1996) QUE94201 shergottite: crystallization of a Martian basaltic magma. *Geochim. Cosmochim. Acta* **60**, 4563–4569.

McSween H. Y. (2015) Petrology on Mars. *Am. Mineral.* **100**, 2380–2395.

McSween, H. Y., Jr., and Stöffler, D. (1980) Shock Metamorphic Features in ALHA77005 Meteorite. *Lunar Planet. Sci. XI,* Lunar Planet. Inst., Houston. 717–719.

McSween H. Y., Eisenhour D. D., Taylor L. A., Wadhwa M., and Crozaz G. (1996) QUE 94201 shergottite: Crystallization of a Martian basaltic magma. *Geochim. Cosmochim. Acta* **60**, 4563–4569.

McSween H. Y., Stolper E. M., Taylor L. A., Muntean R. A., O'Kelley G. D., Eldridge J. S., Biswas S., Ngo H. T., and Lipschutz M. E. (1979a) Petrogenetic relationship between Allan Hills 77005 and other achondrites. *Earth Planet. Sci. Lett.* **45**, 275–284.

McSween H. Y., Taylor L. A., and Stolper E. M. (1979b) Allan Hills 77005: A new meteorite type found in Antarctica. *Science* **204**, 1201–1203.

McSween H. Y., and Treiman A. H. (1998) Martian meteorites. *Reviews in Mineralogy* **36**, 1–53.

McSween H. Y., Grove T. L., Wyatt M. B. (2003) Constraints on the composition and petrogenesis of the Martian crust. *J. Geophys. Res. Planet* **108**, 5135–5152.

McSween H. Y., Taylor G. J., and Wyatt M. B. (2009) Elemental Composition of the Martian Crust. *Science* **324**, 736–739.

Mikouchi T., and Miyamoto M. (1996) A new member of lherzolitic Shergottite from Japanes Antarctic Meteorite Collection: Mineralogy and petrology of Yamato-793605. *Antarctic Meteorites XXI,* **21**, 104–106.

Mikouchi T. (2005) Northwest Africa 1950: Mineralogy and comparison with Antarctic lherzolitic shergottites. *Meteorit. Planet. Sci.* **40**, 1621–1634.

Mikouchi T., and Kurihara T. (2008) Mineralogy and petrology of paired lherzolitic shergottites Yamato 000027, Yamato 000047, and Yamato 000097: Another fragment from a Martian "lherzolite" block. *Polar Sci.* **2**, 175–194.

Milman-Barris M. S., Beckett J. R., Baker M. B., Hofmann A. E., Morgan Z., Crowley M. R., Vielzeuf D., and Stolper E. (2008) Zoning of phosphorus in igneous olivine. *Contrib. Mineral. Petrol.* **155**, 739–765.

Misawa K., Yamada K., Nakamura N., Morikawa N, Yamashita K., and Premo W. R. (2006) Sm-Nd isotope systematics of lherzolitic shergottite Yamato-793605. *Antarctic Meteorite Research* **19**, 45–57.

Misawa K., Park J., Shih C.-Y., Reese Y., Bogard D. D., and Nyquist L. E. (2008) Rb-Sr, Sm-Nd, and Ar-Ar isotopic systematics of lherzolitic shergottite Yamato 000097. *Polar Sci.* **2**, 163–174.

Morgan D. J., and Jerram D. A. (2006) On estimating crystal shape for crystal size distribution analysis. *J. Volc. Geotherm. Res.* **154**, 1–7.

Nekvasil H., Dondolini A., Horn J., Filiberto J., Long H., and Lindsley D. H. (2004) The origin and evolution of silica-saturated alkali suites: An experimental study. *J. Petrol.* **45**, 693–721.

Nekvasil H., Filiberto J., McCubbin F. M., and Lindsley D. H. (2007) Alkalic parental magmas for the chassignites? *Meteorit. Planet. Sci.* **42**, 979–992.

Niihara T. (2011) Uranium-lead age of baddeleyite in shergottite Roberts Massif 04261: Implications for magmatic activity on Mars. *J. Geophys. Res. Planet.* **117**, E12.

Nishiizumi K., and Caffee M. W. (2010) A tale of two shergottites: RBT 04261 and RBT 04262. *Lunar Planet. Sci. XXXXI,* Lunar Planet. Inst., Houston. #2276. (abstr.).

Nyquist L. E., Bogard D. D., Shih C. –Y., Greshake A., Stöffler D., and Eugster O. (2001) Ages and Geologic Histories of Martian Meteorites. *Springer Netherlands* **12**, 105–164.

Nyquist L. E., Bogard D. D., Shih C. Y., Park J., Reese Y. D., and Irving A. J. (2009) Concordant Rb–Sr, Sm–Nd, and Ar–Ar ages for Northwest Africa 1460: a 346 Ma old basaltic shergottite related to "lherzolitic" shergottites. *Geochim. Cosmochim. Acta* **73**, 4288–4309.

Ostertag R., Amthauer G., Rager H., and McSween H. Y. Jr. (1984) Fe3+ in shocked olivine crystals of the ALHA 77005 meteorite. *Earth Planet. Sci. Lett.* **67**, 162–166.

Ott U. (1988) Noble gases in SNC meteorites: Shergotty, Nakhla, Chassigny. *Geochim. Cosmochim. Acta* **52**, 1937–1948.

Papike J. J., Karner J. M., Shearer C. K., and Burger P. V. (2009) Silicate mineralogy of martian meteorites. *Geochim. Cosmochim. Acta* **73**, 7443–7485.

Peslier A. H., Woodland A. B., and Wolff J. A. (2008) Fast kimberlite ascent rates estimated from hydrogen diffusion profiles in xenolithic olivines from Southern Africa. *Geochim. Cosmochim. Acta* **72**, 2711–2722.

Peslier A. H., Hnatyshin D., Herd C. D. K., Walton E. L., Brandon A. D., Lapen T. J., and Shafer J. T. (2010) Crystallization, melt inclusion, and redox history of a Martian meteorite: Olivine-phyric shergottite Larkman Nunatuk 06319. *Meteorit. Planet. Sci.* **74**, 4543–4576.

Peters T. J, Simon J. I., Jones J. H., Usui T., Moriwaki R., Economos R. C., Schmitt A. K., and McKeegan K. D. (2015) Tracking the source of the enriched martian meteorites in olivine-hosted melt inclusions of two depleted shergottites, Yamato 980459 and Tissint. *Earth Planet. Sci. Lett.* **418**, 91–102.

Platz T., Michael G., Tanaka K. L., Skinner J. A., and Fortezzo, C. M. (2013) Crater-based dating of geological units on Mars: Methods and application for the new global geological map. *Icarus* **255**, 806–827.

Potter S. A., Brandon A. D., and Peslier A. H. (2015) Melt inclusion analysis of RBT 04262 with relationship to shergottites and Mars surface compositions. *Lunar Planet. Sci. XXXXVI*, Lunar Planet. Inst., Houston. #2945 (abstr.).

Pruis M. J. and Tanaka K. L. (1995) The Martian northern plains did not result from plate tectonics. *Lunar and Planetary Science,* 1147–1148.

Rubin A. E., Warren P. H., Greenwood J. P., Verish R. S., Leshin L. A., Hervic R. L., Clayton R. N., and Mayeda T. K. (2000) Los Angeles: The most differentiated basaltic martian meteorite. *Geology* **28**, 1011–1014.

Sack R. O. and Ghiorso M. S. (1989) Importance of considerations of mixing properties in establishing an internally consistent database: Thermochemistry of minerals in the system Mg2SiO4-Fe2SiO4-SiO2. *Contrib. Mineral. Petrol.* **102**, 41–68.

Sack R. O. and Ghiorso M. S. (1991a) An internally consistent model for the thermodynamic properties of Fe-Mg-titanomagnetite-aluminate spinels: Thermochemistry of minerals in the system Mg2SiO4-Fe2SiO4-SiO2. *Contrib. Mineral. Petrol.* **106**, 474–505.

Sack R. O. and Ghiorso M. S. (1991b) Chromian spinels as petrogenetic indicators: Thermodynamics and petrological applications. *Am. Mineral.* **76**, 827–847.

Sack R. O. and Ghiorso M. S. (1994a) Thermodynamics of multicomponent pyroxenes: I. Formulation of a general model. *Contrib. Mineral. Petrol.* **116**, 277–286.

Sack R. O. and Ghiorso M. S. (1994b) Thermodynamics of multicomponent pyroxenes: II. Phase relations in the quadrilateral. *Contrib. Mineral. Petrol.* **116**, 287–300.

Sack R. O. and Ghiorso M. S. (1994c) Thermodynamics of multicomponent pyroxenes: III. Calibration of $Fe^{2+}(Mg)_{-1}$, $TiAl_2(MgSi_2)_{-1}$, $TiFe_2^{3+}(MgSi_2)_{-1}$, $AlFe^{3+}(MgSi)_{-1}$, $NaAl(CaMg)_{-1}$, $Al_2(MgSi)_{-1}$ and $Ca(Mg)_{-1}$ exchange reactions between pyroxenes and silicate melts. *Contrib. Mineral. Petrol.* **118**, 271–296.

Shafer J. T., Brandon A. D., Lapen T. J., Righter M., Peslier A. H., and Beard B. L. (2010) Trace element systematics and ^{147}Sm-^{143}Nd and ^{176}Lu-^{176}Hf ages of Larkman Nunatak 06319: Closed-system fractional crystallization of an enriched shergottite magma. *Geochim. Cosmochim. Acta* **74**, 7307–7328.

Shearer C. K., McKay G., Papike J. J., and Karner J. M. (2006) Valence state partitioning of vanadium between olivine-liquid: Estimates of the oxygen fugacity of Y980459 and application to other olivine-phyric Martian basalts. *Am. Mineral.* **91**, 1657–1663.

Shearer C. K., Burger P. V., Papdce J. J., Borg L. E., Irving A. J., and Herd C. D. K. (2008) Petrogenetic linkages among Martian basalts: Implications based on trace element chemistry of olivine. *Meteorit. Planet. Sci.* **43**, 1241–1258.

Shearer C. K., Aaron P. M., Burger P. V., Guan Y., Bell A. S., and Papike J. J. (2013) Petrogenetic linkages among fO2, isotopic enrichments-depletions and crystallization history in Martian basalts. Evidence from the distribution of phosphorus in olivine megacrysts. *Geochim. Cosmochim. Acta* **120**, 17–38.

Shea T., Lynn K. J., Garcia M. O. (2015) Cracking the olivine zoning code: distinguishing between crystal growth and diffusion. *Geology* **43**, 935–938

Shih C. Y., Nyquist L. E., Bogard D. D., McKay G. A., Wooden J. L., Bansal B. M., and Wiesmann H. (1982) Chronology and petrogenesis of young achondrites, Shergotty, Zagami, and ALHA77005: Late magmatism on a geologically active planet. *Geochim. Cosmochim. Acta* **46**, 2323–2344.

Shih C. -Y., Nyquist L. E., Wiesmann H. and Barrat J. A. (2003) Age and petrogenesis of picritic shergottite NWA1068: Sm–Nd and Rb–Sr isotopic studies. *Lunar Planet. Sci. XXXIV*, Lunar Planet. Inst., Houston. #1439 (abstr.).

Shih C. -Y., Nyquist L. E., Weismann H., Reese Y., and Misawa K. (2005) Rb-Sr and Sm-Nd dating of olivine-phyric shergottite Yamato 980459: Petrogenesis of depleted shergottites. *Antarctic Meteorite Research,* **18**, 46–65.

Shih C. Y., Nyquist L. E., and Reese Y. (2009). Rb-Sr and Sm-Nd studies of olivine-phyric shergottites RBT 04262 and LAR 06319: Isotopic evidence for relationship to enriched basaltic shergottites *Lunar Planet. Sci. XXXX,* Lunar Planet. Inst., Houston. #1360 (abstr.).

Shih C. -Y., Nyquist L. E., Reese Y., and Misawa K. (2011) Sm-Nd and Rb-Sr studies of lherzolitic shergottite Yamato 984028. *Polar Sci.* **4**, 515–529.

Spandler C., O'Neill H. S., and Kamenetsky V. S. (2007) Survival times of anomalous melt inclusions from element diffusion in olivine and chromite. *Nature* **447**, 303–306.

Smith M. R., Laul J. C., Ma M. S., Huston T., Verkouteren R. M., Lipschutz M. E., and Schmitt R. A. (1984) Petrogenesis of the SNC (shergottites, nakhlites, chassignites) meteorites:

Implications for their origin from a large dynamic planet, possibly Mars. *J. Geophys. Res. Planet.* **89**, B612–B630.

Stolper E., and McSween H. Y. (1979) Petrology and origin of the shergottite meteorites. *Geochim. Cosmochim. Acta* **43**, 1475–1498.

Symes S. J. K., Borg L. E., Shearer C. K., and Irving A. J. (2008) The age of the martian meteorite Northwest Africa 1195 and the differentiation history of the shergottites. *Geochim. Cosmochim. Acta* **72**, 1696–1710.

Takenouchi A., Mikouchi T., and Kogure T. (2017) Mineralogical study of brown olivine in Northwest Africa 1950 shergottite and implications for the formation mechanism of iron nanoparticles. *Meteorit. Planet. Sci.* **52**, 1–14.

Takenouchi A., Mikouchi T., Yamaguchi A. (2018) Shock veins and brown olivine in Martian meteorites: Implications for their shock pressure-temperature histories. *Meteorit. Planet. Sci.* 1–26.

Tait K. T. and Day J. M. D. (2018) Chondritic late accretion to Mars and the nature of shergottite reservoirs. *Earth Planet. Sci. Lett.* **494**, 99–108.

Taylor L. A., Nazarov M. A., Shearer C. K., McSween H. Y., Cahill J., Neal C. R., Ivanova M. A., Barsukova L. D., Lentz R. C., Clayton R. N., and Mayeda T. K. (2002) Martian meteorite Dhofar 019: A new shergottite. *Meteorit. Planet. Sci.* **37**, 1107–1128.

Treiman A. H. (2003) Chemical compositions of martian basalts (shergottites): Some inferences on basalt formation, mantle metasomatism, and differentiation in Mars. *Meteorit. Planet. Sci.* **38**, 1849–1864.

Treiman A. H., McKay G. A., Bogard D. D., Mittlefield D. W., Wang M.-S., Keller L., Lipschutz M. E., Lindstrom M. M., and Garrison D. (1994) Comparison of the LEW 88516 and ALHA 77005 martian meteorites: Similar but distinct. *Meteorit. Planet. Sci.* **29**, 581–592.

Treiman A. H., Dyar M. D., McCanta M., Noble S. K., and Pieters C. M. (2007) Martian Dunite NWA 2737: Petrographic constraints on geological history, shock events, and olivine color. *J. Geophys. Res. Planet.* **112**, E04002.

Treiman A. H., and Filiberto J. (2015) Geochemical diversity of shergottite basalts: mixing and fractionation, and their relation to Mars surface basalts. *Meteorit. Planet. Sci.* **50**, 632-648.

Udry A. and Day J. M. D. (2018) 1.34 billion-year-old magmatism on Mars evaluated from the co-genetic nakhlite and chassignite meteorites. *Geochim. Cosmochim. Acta* **238**, 292–315.

Udry A., Howarth G. H., Lapen T. J., and Righter M. (2017) Petrogenesis of the NWA 7320 enriched martian gabbroic shergottite: Insight into the martian crust. *Geochim. Cosmochim. Acta* **204**, 1–18.

Usui T., McSween H. Y., and Floss C. 2009. Petrogenesis of olivine-phyric shergottite Yamato 980459, revisited. *Geochim. Cosmochim. Acta* **72**, 1711–1730.

Usui T., Sanborn M., Wadhwa M., and McSween H. Y. (2010) Petrology and trace element geochemistry of Robert Massif 04261 and 04262 meteorites, the first examples of geochemically enriched lherzolitic shergottites. *Geochim. Cosmochim. Acta* **74**, 7283–7306.

Van de Moortéle B., Reynard B., Rochette P., Jackson M., Beck P., Gillet P., McMillan P. F., and McCammon C. A. (2007a) Shock-induced metallic iron nano-particles in olivine-rich Marian meteorites. *Earth Planet. Sci. Lett.* **262**, 37–49.

Van de Moortéle B., Reynard B., McMillan P. F., Wilson M., Beck P., Gillet P., and Jahn S. (2007b) Shock-induced transformation of olivine to a new metastable (Mg, Fe)2SiO4 polymorph in Martian meteorites. *Earth Planet. Sci. Lett.* **261**, 469–475.

Wadhwa M. 2001. Redox state of Mars' upper mantle and crust from Eu anomalies in shergottite pyroxenes. *Science* **291**, 1527–1530.

Wadhwa M., McSween H. Y., and Floss C. (1994) Petrogenesis of shergottite meteorites inferred from minor and trace element microdistributions. *Geochim. Cosmochim. Acta* **58**, 4213–4229.

Wadhwa M., McKay G. A., and Crozaz G. (1999) Trace element distributions in Yamato-793605, a chip off the ''Martian lherzolite'' block. *Antarctic Meteorite Research* **12**, 168–182.

Wadhwa M., Lentz R. C. F., McSween H. Y., and Crozaz G. (2001) A petrologic and trace element study of Dar al Gani 476 and Dar al Gani 489: Twin meteorites with affinities to basaltic and lherzolitic shergottites. *Meteorit. Planet. Sci.* **36**, 195–208.

Walton E. L. and Herd C. D. K. (2007a) Dynamic crystallization of shock melts in Allan Hills 77005: Implications for melt pocket formation in Martian meteorites. *Geochim. Cosmochim. Acta* **71**, 5267–5285.

Walton E. L. and Herd C. D. K. (2007b) Localized shock melting in lherzolitic shergottite Northwest Africa 1950: Comparison with Allan Hills 77005. *Meteorit. Planet. Sci.* **42**, 63–80.

Walton E. L. and Shaw C. S. J. (2009) Understanding the textures and origin of shock melt pockets in Martian meteorites from petrographic studies, comparisons with terrestrial mantle xenoliths, and experimental studies. *Meteorit. Planet. Sci.* **44**, 55–76.

Walton E. L., Irving A. J., Bunch T. E., and Herd C. D. K. (2012) Northwest Africa 4797: A strongly shocked ultramafic poikilitic shergottite related to compositionally intermediate Martian meteorites. *Meteorit. Planet. Sci.* **47**, 1449–1474.

Warren P. H. and Kallemeyn G. W. (1997) Yamato-793605, EETA79001, and other presumed Martian meteorites; compositional clues to their origins. *In Antarctic Meteorite Research* **10**, 61–81.

Watson E. B., Cherniak D. J., and Holycross M. E. (2015) Diffusion of phosphorus in olivine and molten basalt. *Am. Mineral.* **100**, 2053–2065.

Watson E. B., Müller T. (2009) Non-equilibrium isotopic and elemental fractionation during diffusion-controlled crystal growth under static and dynamic conditions. *Chem. Geol.* **267**, 111–124.

Welsch B, Faure F, Famin V, Baronnet A, Bachèlery P (2013) Dendritic crystallization: a single process for all the textures of olivine in basalts? *J. Petrol.* **54,** 539–574.

Welsch B, Hammer J, Hellebrand E (2014) Phosphorus zoning reveals dendritic architecture of olivine. *Geology* **42**, 867–870.

Welsch B, Hammer J, Baronnet A, Jacob S, Hellebrand E, Sinton J (2016) Clinopyroxene in postshield Haleakala ankaramite: Texture, compositional zoning and supersaturation in the magma. *Contrib. Miner. Petrol.* **171**, 1–19.

Wieczorek M. A., and Zuber M. T. (2004) Thickness of the Martian crust: Improved constraints from geoid-to-topography ratios. *J. Geophys. Res. Planet.* **109**, E01009.

Wieler R., Huber L., Busemann H., Seiler S., Leya I., Maden C., Masarik J., Meier M. M. M., Nagao K., Trappitch R., and Irving A. J. (2016) Noble gases in 18 Martian meteorites and angrite Northwest Africa 7812 – Exposure ages, trapped gases, and a re-evaluation of the evidence for solar cosmic ray-produced neon in shergottites and other achondrites. *Meteorit. Planet. Sci.* **51**, 407–428.

Wood B. J. (1991) Oxygen barometry of spinel peridotites: *Rev. Min.*, **25**, 417–431.

Xing C. -M., Wang C. Y., and Tan W. (2017) Disequilibrium growth of olivine in mafic magmas revealed by phosphorus zoning patterns of olivine from mafic-ultramafic intrusions. *Earth Planet. Sci. Lett.* **479**, 108–119.

Zipfel J., Scherer P., Spettel B., Dreibus G., and Schultz L. (2000) Petrology and chemistry of the new shergottite Dar al Gani 476. *Meteorit. Planet. Sci.* **35**, 95–106.

RACHEL R. RAHIB

Department of Geoscience
University of Nevada, Las Vegas
Rachel.rahib93@gmail.com

EDUCATION

University of Nevada, Las Vegas – Las Vegas, NV
Bachelor of Science: Geology (12/2015)
3.71 GPA

University of Nevada, Las Vegas – Las Vegas, NV
Master of Science: Geology – Igneous Petrology and Planetary Science (01/2017 – present)
3.96 GPA

EXPERIENCE

- **Jacobs-JETS Remote-Intern** (08/2018 – present)
  NASA Johnson Space Center – Houston, TX based at UNLV – Las Vegas, NV
  Geochemical and petrological study by utilization of an electron microprobe and petrographic microscope to analyze enstatite-rich meteorites, in order to understand their origins, and to compare them to data obtained by MESSENGER for Mercury. Data to be used in abstracts, peer-reviewed publications, and future grant proposals.
  Research Advisors: Dr. Kathleen VanderKaaden, Dr. Arya Udry, and Dr. Francis McCubbin

- **Teaching Assistant – University of Nevada Las Vegas** (06/2018 – 07/2018)
  Geoscience Department UNLV – Las Vegas, NV
  Assisted with, and graded, all lab assignments for two lab sections of GEOL 101, during a five-week summer session course.

- **Research Assistant – University of Nevada Las Vegas** (08/2017 – 08/2018)
  Geoscience Department UNLV – Las Vegas, NV
  Mentored undergraduate on independent senior thesis project focusing on enstatite-rich meteorites and their potential to represent petrologic analogues to Mercury. Prepared samples for analyses. Assisted with collecting, processing, and interpreting data. Co-authored on peer-reviewed journal manuscript.

- **Teaching Assistant – University of Nevada Las Vegas** (01/2017 – 05/2017)
  Geoscience Department UNLV – Las Vegas, NV
  Taught and set up all labs for two laboratory sections of GEOL 101, graded all assignments, led class field trip, and hosted weekend study/practice sessions.

- **Research Assistant – University of Nevada Las Vegas** (11/2013 – 06/2014)
  Environmental Soil Analytical Laboratory (ESAL) UNLV – Las Vegas, NV
  Maintained laboratory and equipment. Sieved and organized soil samples. Compiled and edited databases for analyzed samples. Performed quality assurance procedures for databases.
  Research Advisor: Dr. Brenda Buck.

RESEARCH

- **Master's Thesis – University of Nevada Las Vegas** (01/2017 – present)
  Formation and emplacement processes of martian poikilitic shergottite meteorites
  Research project focusing on understanding petrogenesis of relatively rare and understudied subgroup of martian meteorites (poikilitic shergottites). Presented findings at numerous national scientific conferences. Research Advisor: Dr. Arya Udry.

- **Undergraduate Senior Thesis – University of Nevada Las Vegas** (05/2015 – 12/2015)
  *Crystal size distribution (CSD) analysis of olivine in the lherzolitic shergottite NWA 446*8
  Conducted literature review on martian meteorites. Applied CSD analyses by delineation of olivine grain boundaries to understand mineral crystallization history. Utilized various computer software to obtain and process results. Produced a research report and delivered a presentation to convey findings. Research Advisor: Dr. Arya Udry.

PUBLICATIONS
JOURNAL ARTICLES

- Udry A., Wilbur Z. E., **Rahib R. R.**, McCubbin F. M., Vander Kaaden K. E., McCoy T. J., Ziegler K., Gross J., DeFelice C., Combs L., Turrin D. B. (In revision) Reclassification of four aubrites as enstatite chondrite impact melts: New analogues for Mercury. *Meteoritics and Planetary Sciences,* In Revision.
- Combs L. M., Udry A., Howarth G. H., Righter M., Lapen T. J., Gross J., Ross K. D., **Rahib R. R.**, Day J. M. D. (In review) Petrology of the enriched poikilitic shergottite Northwest Africa 10169: Insight into the martian interior. *Geochimica et Cosmochimica Acta,* In Review.

ABSTRACTS AND EXTENDED ABSTRACTS

- **Rahib R. R.**, Udry A.**,** Howarth G. H., Gross J., Paquet M., Day J. M. D. (2018) Petrogenesis of enriched and intermediate poikilitic shergottites: From magmatic source to emplacement, Geological Society of America Conference (Denver, November 2018).

- Wilbur Z. E., Udry A., McCubbin F. M., Vander Kaaden K. E., **Rahib R. R.**, and McCoy T. J. (2018) Aubrite and enstatite chondrite impact melt meteorites: Analogs to Mercury?, Mercury: Current and Future Science Workshop, Abstract #6034.

- **Rahib R. R**., Udry A.**,** Combs L. C., Howarth G. H. (2018) Formation and emplacement processes of martian poikilitic shergottite meteorites, Lunar and Planetary Science Conference XLIX Houston, Abstract #1303.

- Combs L. M., Udry A.**,** Howarth G. H., Lapen T. J., Righter M., Gross J., Day J. M. D., and **Rahib R. R.** (2018) Petrology of the enriched poikilitic shergottite Northwest Africa 10169: Insight into the martian interior, Lunar and Planetary Science Conference XLIX Houston, Abstract #1727.

- Wilbur Z. E., Udry A., McCubbin F. M., Combs L. M., **Rahib R. R**., McCoy T. J., and McCoy C. (2018) Aubrite and enstatite chondrite impact melt meteorites as potential analogs to mercury, Lunar and Planetary Science Conference XLIX Houston, Abstract #1355.

- **Rahib R. R.**, Udry A., Combs L. M. (2017) Emplacement of martian poikilitic shergottite meteorites using quantitative textural analyses, 2017 NASA Space Grant and Nevada NASA EPSCoR Statewide Meeting.

- Combs L. M., Udry A., **Rahib R. R.** (2017) Petrology of the new enriched poikilitic shergottite Northwest Africa (NWA) 10169: Insight into the martian interior, 2017 NASA Space Grant and Nevada NASA EPSCoR Statewide Meeting.

- **Rahib R. R.**, Udry A**.**, Howarth G. H. (2017) Constraining formation and emplacement processes of poikilitic shergottites using quantitative textural analyses 80thAnnual Meeting of the Meteoritical Society, Abstract #6027.

- Laczniak D., Combs L., **Rahib R.**, and Udry A. (2016) Textural Analysis of Enriched Poikilitic Shergottite, Geological Society of America Conference (Denver, September 2016).

HONORS AND AWARDS

- **UNLV Access Grant** (2018)
  UNLV Graduate College - $2,000
- **Alumni Association Scholarship** (2018)
  UNLV Graduate College - $2,500
- **James F. Adams/GPSA Scholarship** (2018)
  UNLV Graduate College - $1000
- **Desert Space Foundation Scholarship** (2018)
  Department of Geoscience, University of Nevada, Las Vegas - $980
- **GPSA Book Scholarship** (2017)
  Graduate and Professional Student Association - $200
- **Graduate Research Opportunity Fellowship** (2017)
  Nevada NASA Space Grant Consortium - $18,000
- **Edwards and Olswang Scholarship** (2017)
  Department of Geoscience, University of Nevada, Las Vegas - $500
- **Student Travel Award** (2017)
  Lunar and Planetary Institute - $1,000
- **Bernada French Scholarship** (2016 – 2017)
  Department of Geoscience, University of Nevada, Las Vegas - $600
- **Anne Fenton Wyman Scholarship** (2015)
  Department of Geoscience, University of Nevada, Las Vegas - $625
- **Douglas Orr Memorial Scholarship** (2015)
  Department of Geoscience, University of Nevada, Las Vegas - $474
- **UNLV Dean's Honor List** (2013-2015)

SKILLS

Laboratory: Petrographic microscopy (reflected and transmitted light), scanning electron microscopy with energy dispersive spectroscopy (SEM-EDS), electron microscopy (X-ray mapping, EDS and WDS point analyses).
Software: *Microsoft Word*, *PowerPoint*, *Excel*; *Adobe Illustrator*, *Adobe Photoshop*; *ImageJ*; *CSDCorrection; IgPet Rockware.*